MODELING AND FEEDBACK CONTROL OF MEMS DEVICES

by

BRUNO BOROVIC

Presented to the Faculty of the Graduate School of

The University of Texas at Arlington in Partial Fulfillment

of the Requirements

for the Degree of

DOCTOR OF PHILOSOPHY

THE UNIVERSITY OF TEXAS AT ARLINGTON

December 2005

Copyright © by Bruno Borovic 2005

All Rights Reserved

ACKNOWLEDGEMENTS

I would like to express my sincere appreciation and gratitude to my advisor, Dr. Frank L. Lewis for his constant guidance, encouragement and inspiration. Regardless of how hard you work, it is impossible to outrun him. My special thanks go to Dr. Edward S. Kolesar, my co-advisor, for permanent help, advice and years of encouragement. When I needed to share my visions, he was there. Special thanks to Dr. Dereje Agonafer for being an inexhaustible source of ideas and the driving force that actually launched me towards my first research results. Thanks to Dr. Ai Qun Liu for sharing with me his excitement and knowledge about optical MEMS devices, and allowing me to get into the area by working in his lab. Thanks to my former advisor, Dr. Zoran Vukic, and to Dr. Ljubomir Kuljaca for their priceless advice. Thanks to Dr. Ognjen Kuljaca for tolerating me as his roommate. Thanks to all my colleagues and friends with whom I have had pleasure of working during the past several years at ARRI. It was fun. Furthermore, I would like to thank everybody at ARRI, especially Ms. Raynette Taylor and Ms. Sarah Densmore for making my life much easier. Finally, I would like to dedicate this thesis to my parents without whom I would never have been able to make it this far.

October 18, 2005

ABSTRACT

MODELING AND FEEDBACK CONTROL OF MEMS DEVICES

Publication No. ______

Bruno Borovic, PhD.

The University of Texas at Arlington, 2005

Supervising Professor: Frank L. Lewis

As MEMS actuators reach maturity and emerge from the research lab into commercial applications, their increased reliability, speed, and performance accuracy is needed. MEMS are typically driven directly in an open-loop fashion by applying simple actuating signals. The requirements for better dynamical behavior, however, have resulted in the gradual introduction of improved actuation approaches, such as pre-shaped open-loop driving and closed-loop control. Unlike macro mechanical systems where the implementation of the feedback is relatively simple, it is quite problematic in

the MEMS case. The presence of fast system dynamics, and physical area efficiency requirements have introduced additional challenges for feedback control design. The main purpose of this work is to explore possibilities and envision applications where closed-loop strategies can be successfully used.

Naturally, the design of reliable actuating techniques requires simple but accurate dynamic models of the device, either in input/output or in the state variable form. Accurate models lead towards optimal design, better performance, better understanding of the device, short development time, and consequently, lower cost of the device. The modeling of thermal and electrostatic actuators, based on synergy between finite element analysis (FEA) and analytical approaches is, therefore, another subject that this dissertation deals with.

The dissertation focuses mainly on the two most common types of MEMS actuators- thermal and electrostatic. It encloses several chapters addressing development of the modeling methods and advanced actuating techniques, including closed-loop control. The dissertation contains a novel, finite element analysis (FEA)-based modeling method for thermal actuators, position and light intensity control techniques for an optical MEMS device actuated by an electrostatic comb drive, a control system for preventing lateral instability for the comb electrostatic actuator and, finally, a discussion on the sensing structure and force contribution model for the lateral motion control.

TABLE OF CONTENTS

ACKNOWLEDGEMENTS iii

ABSTRACT iv

LIST OF ILLUSTRATIONS x

LIST OF TABLES xv

Chapter

1. INTRODUCTION 1

2. METHOD FOR DETERMINING A DYNAMICAL STATE-SPACE MODEL FOR CONTROL OF THERMAL MEMS DEVICES 6

2.1 Introduction 6

2.2 Structure of Dynamical Model 8

2.2.1 Structure of the Electro-Thermal Model 10

2.2.2 Structure of the Mechanical Model 12

2.2.3 Complete Dynamical Model and Unknown Parameters 13

2.3 FEA Based System Identification 14

2.3.1 Electro-Thermal Model Parameter Estimation 15

2.3.2 Mechanical Model Parameter Estimation 18

2.4 Experiments / Verification 22

2.5 Conclusion 32

3. OPEN-LOOP VS. CLOSED-LOOP CONTROL OF MEMS DEVICES: CHOICES AND ISSUES.. 34

3.1 Introduction.. 34

3.2 System Description.. 36

3.3 Mathematical Model... 39

3.4 Open vs. Closed-Loop Control... 46

3.4.1 Open-Loop Strategies.. 46

3.4.2 Closed-Loop Actuation... 51

3.5 Discussion: Comparison & Issues.. 53

3.5.1 Purpose of the device.. 53

3.5.2 Sensitivity of the parameters.. 54

3.5.3 Problems - Small Scale Feedback... 56

3.6 Conclusions.. 58

4. LIGHT-INTENSITY-FEEDBACK WAVEFORM GENERATOR BASED ON MEMS VARIABLE OPTICAL ATTENUATOR.............. 60

4.1 Introduction.. 60

4.2 Device Description.. 63

4.3 Mathematical Model... 64

4.3.1 Optical Sensing Model.. 64

4.3.2 The Complete Model... 67

4.4 Controller Design... 67

4.4.1 Position Control Loop.. 68

4.4.2 Light Intensity Control Loop... 71

4.5 Experimental Results 73

4.6 Device Properties 77

4.7 Conclusions 79

5. LATERAL INSTABILITY PROBLEM IN ELECTROSTATIC COMB DRIVE ACTUATORS: MODELING & FEEDBACK CONTROL 81

5.1 Introduction 81

5.2 Mathematical Model 84

5.2.1 Structure of the Mechanical Model 85

5.2.2 General Model: Assumptions and Structure 86

5.2.3 Electrostatic Model: Actuator and Lateral Instability 87

5.3 Model Verifications and Refinement 89

5.3.1 Model Summary and Characteristics 95

5.4 Extended Model for Lateral Actuator / Sensor 97

5.5 Control System Design 100

5.5.1 Implementation Issues - Discussion 105

5.6 Conclusions 105

6. LATERAL MOTION CONTROL OF THE ELECTROSTATIC COMB DRIVE: SENSING AND FORCE CONTRIBUTION MODEL 107

6.1 Introduction 107

6.2 System Description 108

6.3 Capacitances 111

6.4 Electrostatic Forces and Contribution Matrix 111

6.5 Capacitance sensitivity 115

6.6 Implementation Difficulties 121

6.6.1 Electric Circuitry / Influence on Measurement 121

6.6.2 Capacitance vs. Aspect Ratio 124

6.7 Conclusions 127

7. CONCLUSIONS 128

Appendix

A. ILLUSTRATIVE EXAMPLE FOR THERMAL ACTUATOR MODELING METHOD 132

REFERENCES 143

BIOGRAPHICAL INFORMATION 151

LIST OF ILLUSTRATIONS

Figure Page

2.1 Structure of the flexible electro-thermally driven mechanical structure and the temperature distribution over the body of the device. 9

2.2 Lumped thermal parameter model. 11

2.3 Block scheme of the model (2.8), (2.9), (2.10). 13

2.4 Flow chart showing the modeling methodology. 21

2.5 The *250μm* long bimorph actuator. 23

2.6 FEA Setup. 25

2.7 Thermal conductions of the air and polysilicon for the actuators in first and second example. 26

2.8 Electrical conductions for actuators in both first and second example. 27

2.9 Generated force (top) and deflection (bottom) as a function of average temperature for both examples. 28

2.10 Static *P-x* characteristic (top), dynamic response of deflection (middle) and simulated dynamic response of the electrical current (bottom) for the *200μm* long actuator [7] from example 1 30

2.11 Static *P-x* characteristic (top); voltage, current and deflection (bottom) dynamic responses of the electrical current (bottom) for the 200 *μm* long actuator from example 2. 31

3.1 SEM image of the MEMS VOA showing electrostatic comb drive, moving shuttle with attached shutter, and optical fiber channels. 37

3.2 Design and geometry of the device from figure 3.1 38

3.3 Experimental setup of the VOA. 39

3.4 Open loop response of the simulated model (3.10), (3.11), compared with the experimental one. 41

3.5 Experimental deflection vs. voltage relationship, representing the input nonlinearity of the system. 43

3.6 Optical Position Measurement [3], [19]. 44

3.7 Position –Optical Intensity Characteristics (3.2) – output nonlinearity of the system. 45

3.8 Pre-shaped open loop responses. All signals have the same voltage level (simulation results). 48

3.9 Cascaded multivibrators and summing op-amp for assembling the pre-shaped input signal.. 49

3.10 Pre-shaped open loop response – different voltage levels and dependence of the speed on maximal available voltage (experimental and simulated results)... 50

3.11 Pre-shaped open loop response with and without the compensation of the higher modes (experimental results). 50

3.12 Controller Structure [17], [19]. 51

3.13 Open and Closed Loop Responses and voltage corresponding to closed loop response. 52

3.14 Sensitivity on change in stiffness, *k* represents the original stiffness of the device. 54

3.15 Sensitivity on change in damping, *d* represents the original damping of the device. 55

3.16 Sensitivity on change in mass; *m* represents the original mass of the device. 55

3.17 Difference between capacitive and optical sensing....................................... 56

4.1 Experimental setup of the VOA. ... 63

4.2 Theoretical (4.4) (dashed), and experimental (dotted full line) relationship between V_{PD} and x. ... 66

4.3 Desired value (x_d) and closed-loop response of the inner position loop (top). Open loop position for single transition (0 to $-5 \mu m$) is given for comparison. Control voltages V_b and V_f are given in the bottom part.. ... 70

4.4 Block scheme of the controller... 73

4.5 Desired and actual light intensity for square-wave like signal... 74

4.6 Desired and actual light intensity for saw-wave like signal. ... 75

4.7 Desired and actual light intensity for saw-wave like like signal of lower frequency. ... 76

4.8 Light intensity waveform generator. ... 78

5.1 Electrostatic comb drive actuator in the state of lateral instability. ... 82

5.2 The original electrostatic comb drive actuator [43] (top), and the hypothetical device for lateral DOF feedback control (bottom)... 83

5.3 The first four modes of the actuator. ... 85

5.4 Comb drive with Δd used to model the unbalanced lateral geometry... 89

5.5 Illustration for calculating the influence of the final aspect ratio angle, α, on the capacitances, C_F and C_B, for the DRIE fabricated comb drive electrodes [27]. ... 90

5.6 The influence of the finite aspect ratio $C(\alpha) / C(0)$ on the capacitances C_F and C_B. For $\alpha=0.78\ deg$, the ratio of the capacitances is 2.07. ... 91

5.7 Experimental deflection vs. voltage relationship associated with the input nonlinearity of the system [43]. ... 92

5.8 Relative increase in the capacitance due to *x-z* movement of the electrodes. The change in capacitance for $z<0$ can be assumed to be symmetrical........ 93

5.9 Progress of the lateral instability – A) *0* volts, B) stable state immediately before pull-in, $V_F=8.95\ V$, and $y=0.65\mu m$ and C) pull-in........ 95

5.10 Verification of the model. The first simulation was done for a stable voltage step-function with an amplitude of *8.8V,* the second one with the unstable one with an amplitude of *8.81V*. 96

5.11 Lateral Actuation and sensing schematics. 99

5.12 Lateral Controller. 101

5.13 The dynamic behavior of the system with and without the controller for the step input (*8.8V*)........ 103

5.14 Dynamic behavior of the controlled system for the various voltage levels. In all cases, the achievable deflections are greater than the maximum value for the uncontrolled case. 104

6.1 Electrostatic comb drive actuator with *x*- and *y*-sensing functionality. 109

6.2 Sensing comb unit with four variable capacitors. 111

6.3 Calculation of the force distribution matrix. 114

6.4 Sensing schematics........ 116

6.5 Capacitances and a capacitance sensitivity as a function of secondary gap y_0' 118

6.6 Change in capacitances ΔC_{my1}, ΔC_{my2} and ΔC_{my} as a function of y, with y_0 being parameter. 120

6.7 Influence of the input of the amplifier on the capacitance measurement........ 122

6.8 Influence of the parasitic capacitances C_{c1}, C_{c2}, C_d, and the bias capacitance C_f on the amplitude of the differential voltage v_{y12}-v_{y34}. 123

6.9 Illustration for the calculation of the influence of the final aspect ratio on the capacitances for the DRIE made structures. 125

6.10 Influence of finite aspect ratio on the capacitance for the DRIE made structures. 126

A.1 FE model contains the air box with the actuator body inside. The temperature boundary conditions are applied to the bottom of the box modeling substrate (T=300K). Model is built under assumption that convection and radiation heat removal is negligible. 133

A.2 Electrical conductance as a function of the average temperature. Data from table 3 were curve fitted. 136

A.3 Total thermal conductance as a function of the average temperature. Data from table 1 were curve fitted and the derivative with respect to the average temperature was taken. 137

A.4 FE model contains only the body of the thermal actuator. Pads are fixed with displacement boundary conditions. Temperature distributions inside the thermal actuator body, recorded during electro-thermal FEA are applied to the actuator. 138

A.5 Thermal conductances. Total thermal conductance, is same as in the figure A.3, is now sum of two thermal conductances – through polysilicon and air. 142

LIST OF TABLES

Table Page

2.1 Geometries of the actuators 23

2.2 Temperature dependent material properties for temperature range *300-800 K* 24

2.3 Parameters of the mechanical model 29

5.1 FEA computed values for the modal frequencies, effective masses, and stiffness parameters 86

A.1 Values read out from the FEA 134

A.2 Values calculated directly from the FEA. 135

A.3 Electrical conductance 136

A.4 Mechanical parameters 139

A.5 Values read out from the FEA 141

A.6 Values calculated from the FEA. 141

CHAPTER 1

INTRODUCTION

As MEMS actuators reach maturity and emerge from the research lab into commercial applications, their increased reliability, speed, and performance accuracy will be needed. Five basic on-chip MEMS actuator technologies have been developed: magnetic, piezoelectric, thermal, optical and electrostatic. Regardless of the applied actuation technique, MEMS are typically driven directly in an open-loop fashion by applying simple actuating signals. Consequently, achieving better dynamical behavior of the MEMS device, in terms on both precision and the speed of the response, is limited only by design improvements of the device itself. MEMS actuators have therefore traditionally been gradually modified and improved in terms of mechanical design and better area-efficiency.

The requirements for better dynamical behavior have resulted in the gradual introduction of improved actuation approaches. Introduction of more complex actuating signals have resulted in so-called “pre-shaped control”. Here, the dynamical model of the device is used to construct a pre-shaped input signal that improves the performance of the device. The pre-shaped driving significantly improves the dynamic behavior of the device.

Even the pre-shaped actuation, however, is sometimes not enough. The lack of accurate models and repeatability of the device parameters, compounded by special requirements on the dynamical behavior, have opened the possibility of closed-loop applications. The first MEMS devices incorporating feedback were closed-loop capacitive sensors, with the objective of enhancing measurement accuracy. These applications of feedback do not, by all means, make the field mature. An increase in complexity, device integration, and sophistication level of MEMS devices demands equally sophisticated integrated control systems. Unlike macro mechanical systems where the implementation of the feedback is relatively simple, it is quite problematic in the MEMS case. The presence of fast system dynamics and area efficiency requirements on the controlled MEMS devices has introduced additional challenges for feedback control design.

The design of reliable driving techniques requires simple dynamical differential equation models of the device, either in input/output or in the state variable form. Accurate models lead towards optimal design, better performance and understanding of the device, shortened development time, and consequently, lower cost of the device.

With the above views in mind, the dissertation focuses mainly on two most common types of MEMS actuators - thermal and electrostatic. It encloses several chapters addressing development of the modeling methods and advanced actuating techniques, including closed-loop control.

Chapter 2 describes a straightforward and fast practical technique for developing state-space dynamical models of thermal actuators that are suitable for

feedback control design with guaranteed performance properties. Resulting lumped dynamical state-space model can be evaluated by conducting numerical integration of ordinary differential equations (ODE). The energy distribution inside the model is balanced by introduction of an average, lumped temperature which, combined with the reduced model and static FEA in a novel way, allows effective parameter estimation. The parameters are intuitive and have physical meaning that can be easily be related to the geometry and material properties of the device. The model is flexible and enables a separate introduction of various effects and external forces. Its simplicity makes it highly amenable for the exploring of the different driving techniques necessary to enhance the performance of thermal MEMS actuators. The resulting model is verified with available dynamic experimental results.

In chapter 3, open-loop and closed-loop design of MEMS control systems, detailing the design issues and choices, are compared and contrasted. Experimental results obtained from implementing pre-shaped open-loop and closed-loop control methods are used to compare the two approaches and point out the advantages and disadvantages of both. It is found that with minimum additional implementation complexity, the closed-loop approach speeds up the system and improves its dynamical response. Criteria for choosing between the two control approaches is established and discussed. As a case study, an optical MEMS device (MOEMS) actuated by the electrostatic comb drive was used. The device can be used both as an optical switch (OS) or variable optical attenuator (VOA).

In chapter 4, as an application example, the device from chapter 3 is used in the VOA mode. The controller developed in chapter 3 is extended to include light intensity control. VOAs are extremely popular devices for light attenuation because of large achievable tuning ranges and wavelength independent output of light. Besides, VOA combines fast response time, long-term repeatability and are less expensive than the other existing products. Additional light-intensity control enables very accurate output, faster responses and generation of power intensity waveforms. Light intensity waveform generator can be used as a tool to simulate variable network losses and many other scenarios of network events such as adding/dropping of users, breakdowns in the network…etc.

In chapter 5, the problem of lateral instability of the comb actuators is addressed. The lateral instability occurs when the electrostatic stiffness transverse to the axial direction of motion exceeds the transverse mechanical stiffness of the suspension. The most common way to avoid it is by increasing the transverse stiffness of the suspension. Unfortunately, all of the suspension-stiffening approaches, eventually, limit the traveling range of the actuator. A novel approach, relying on the use of feedback control to counteract the lateral instability, is therefore proposed. A requirement for doing so is to have lateral motion sensing ability and an appropriate model of the device for the subsequent control system design. In order to do that, a suitable model 2 degree of freedom model for lateral stability analysis was established and experimentally verified. Finally, assuming the lateral deflection available, an appropriate control system was designed and approach was tested through a set of simulations.

In chapter 6, a new 2 degree of freedom sensor structure for the problem from section 5 is presented. The sensor structure is intended to sense lateral and axial motion and is not affected by the out-of-plane motions. This novel design provides a means for more effective control of future comb drive actuator including control of lateral instability.

CHAPTER 2

METHOD FOR DETERMINING A DYNAMICAL STATE-SPACE MODEL FOR CONTROL OF THERMAL MEMS DEVICES

2.1 Introduction

Increased reliability, speed, and performance accuracy of the MEMS actuators become an issue as they take part into commercial applications. This will require the either the design of feedback control system that can provide guaranteed performance and robustness [1], or suitable open-loop driving techniques [2]. Applications of feedback control systems design to optical MEMS switching devices have already been considered [3], [4]. The design of reliable feedback controllers requires simple dynamical differential equation models of the device [52], either in input/output or in the state variable form [5]. Moreover, accurate models lead towards optimal design, better performance, shortened development time, and consequently, lower cost of the device [6], [55].

The mathematical modeling of the ETM MEMS device should be considered as a multi-physics phenomena with thermal effects playing a dominant role. In general, the model consists of the three sub-models – electrical, thermal and mechanical. Much activity has been devoted for several years to MEMS modeling [2], [7]-[9], [83], [56], [67]. In [7] a transient FEA was used to obtain a dynamic response. The method was applied to both a hot arm/cold arm actuator and a chevron actuator. In [2] dynamical

equations were derived using physical modeling principles. A simplified linear third-order autoregressive-moving average difference equation was derived. Experiments were used to identify the parameters of this model. Interesting procedure of reducing the order of the model was described in [8]. Good insight and discussion on dynamical properties and applications of the thermal actuators are given in [9]-[11], [57]-[61], [66], [69]. Summarized, all dynamic modeling methods rely on transient FEA, or require dynamic experimental results to fit the parameters into a lumped model. Typically, transient FEA is slow, especially when it has to be done repeatedly as it is the case with consequent development of driving strategies. On the other hand, dynamic experimental results for position are rather hard to obtain as the measurement techniques of small and fast micro-devices are not well developed and typically require expensive equipment.

In this chapter a straightforward practical technique is provided for developing state-space dynamical models that are suitable for feedback control design with guaranteed performance properties. We propose a lumped dynamical state-space model for MEMS thermal actuators that can be evaluated by conducting numerical integration of ordinary differential equations (ODE). First, the structure of the model is derived in standard fashion using laws of physics resulting in a third order model with temperature, velocity and position being the states. Next, the energy distribution inside the model is balanced by introduction of an average, lumped temperature which, combined with the reduced model and static FEA in a novel way, allows effective parameter estimation. The parameters are intuitive and have physical meaning that can

be easily be related to the geometry and material properties of the device. Qualitative influence of the material properties and geometry can be directly tested on the simplified model. Finally, the resulting model is verified with available dynamic experimental results. The resulting model is flexible and enables a separate introduction of various effects and external forces. If necessary, the similar procedure can be used for extension of the degree (order) of the model. The resulting model is in a state-space form that is highly amenable for the design of feedback control systems to enhance the performance of thermal MEMS actuators.

2.2 Structure of Dynamical Model

A general electro-thermally driven flexible mechanical structure is given in figure 2.1. It contains a heated actuating part and a load mass. In order to determine the structure of the lumped model the applicability of the model is limited by a set of assumptions. The method developed herein is useful in modeling of practical thermal actuators within a large class of Lagrangian systems satisfying the following assumptions:

1. The dynamics of the electrical part of the model is negligible e.g. capacitance and inductance do not exist;
2. Thermal capacitance of the surrounding air is negligible when compared to the thermal capacitance of the structural material;
3. Heat flow inside the body of the system from figure 2.1. does not change direction during the transients, e.g. $\text{sgn}(q_{ex}) \geq 0$. If so, the thermal body can be described as the first order system with a concentrated temperature $\overline{T}$;

4. Concentrated temperature $\overline{T}$ is assumed to preserve the amount of thermal energy stored in the system;
5. The mechanical part of the model is limited to the main degree of freedom (DOF) only, and it should be the dominant mode participating the motion in main DOF, *x;*
6. The bandwidth of the other, non-participating modes of the system should be much higher than the bandwidth of the thermal part of the device – e.g. modes should not be excited;
7. Mechanical movements do not affect thermal dynamics.

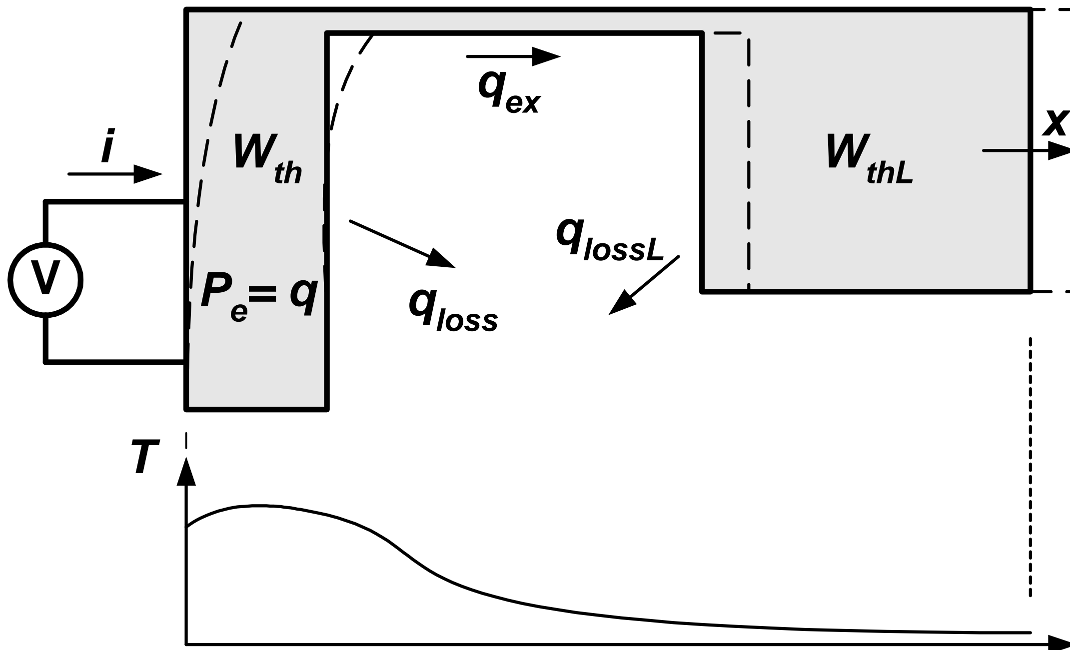

Figure 2.1 Structure of the flexible electro-thermally driven mechanical structure and the temperature distribution over the body of the device.

Based on these assumptions, we propose a method of analysis based on an average temperature $\overline{T}$ that is made precise in the sequel. Given this set of assumptions, the structure of the model can be established. It consists of the first order thermal model and the second order mechanical model.

2.2.1 Structure of the Electro-Thermal Model

When voltage is applied to the contact pads of the ETM device, electrical current flows through the body of the device, causing Joule heating. The ratio between the electrical current and corresponding applied voltage is described by electrical conductance only. Since the electrical resistivity of the device's structural material is temperature dependent, the conductance is also temperature dependent. Having the concentrated temperature $\overline{T}$ of the thermal body, the equation describing the electrical part of the model is given as

$$G_e\left(\overline{T}\right)v = i \tag{2.1}$$

where $G_e\left(\overline{T}\right)$ is the electrical conductance, i is electrical current, and v is the voltage applied to the contact pads. The connection between the electrical and thermal domains can be established through the generation of Joule heat, caused by the electrical current

$$P_e = q = G_e\left(\overline{T}\right)v^2 = \frac{i^2}{G_e\left(\overline{T}\right)} \tag{2.2}$$

where P_e is the electrical power and q is the amount of Joule heating.

Energy is delivered to the element through Joule heating (2.2), and generally removed from it through three heat removal mechanisms – convection, conduction and

radiation [12]. At a specific temperature, a portion of the energy is stored inside the thermal capacitance of the thermal body. Therefore, the thermal model consists of the heat source defined by (2.2), the thermal capacitance, C_{th}, and three thermal conductances that can be associated with the radiation, G_{rad}, convection, G_{conv}, and conduction, G_{cond}, heat removal mechanisms, respectively. In general, it can be assumed that all conductances are dependent on temperature.

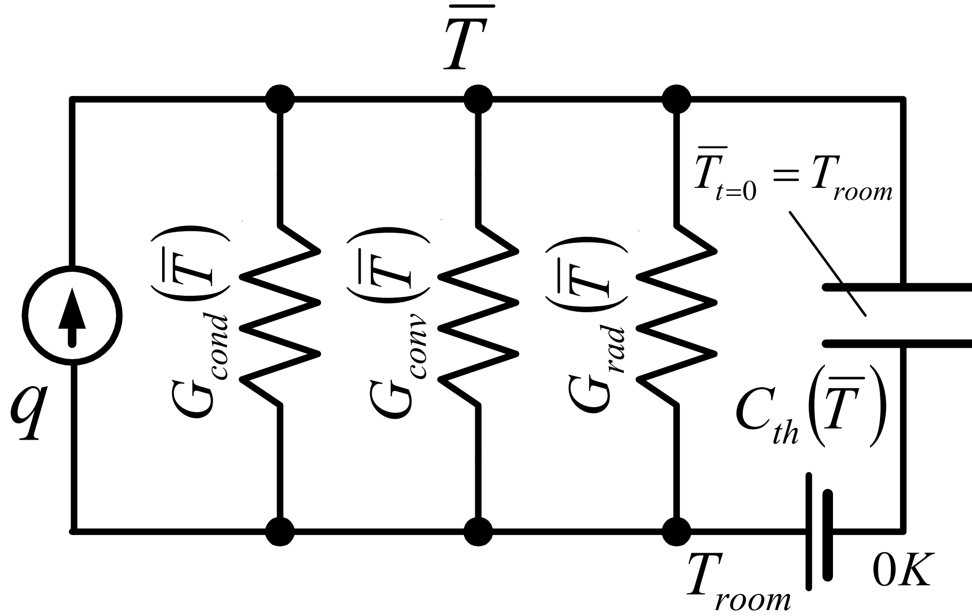

Figure 2.2 Lumped thermal parameter model.

The thermal model is given in Fig 2. and is governed by the following differential equation

$$C_{th}(\overline{T})\dot{\overline{T}} + G_{cond}(\overline{T})\Delta\overline{T} + G_{conv}(\overline{T})\Delta\overline{T} + G_{rad}(\overline{T})\Delta\overline{T} = q \quad (2.3)$$

where $\Delta\overline{T} = \overline{T} - T_{room}$. Initially, the system rests on the room temperature $\overline{T}_{t=0} = T_{room}$.

2.2.2 Structure of the Mechanical Model

In order to find the structure of the mechanical model a deflection of one point on the device is chosen as the primary degree of freedom (DOF), as shown in figure 2.1. In general, considering only the main degree of freedom and neglecting higher order modes, the differential equation describing the motion can be written as

$$\overline{m}(\overline{T})\ddot{x} + d\dot{x} + k(\overline{T})x = \alpha_f(\overline{T}) \tag{2.4}$$

where $\overline{m}$ is the effective moving mass of the device describing both load and actuator mass, k is the stiffness of the device and $\alpha_f(\overline{T})$ is the mechanical force generated by temperature.

Assuming static conditions, e. g. $\ddot{x} = \dot{x} = 0$, equation (2.4) reduces to

$$k(\overline{T})x = \alpha_f(\overline{T}). \tag{2.5}$$

Multiplying and dividing the left hand side of (2.5) by $k(\overline{T})$ yields

$$k(\overline{T})x = k(\overline{T})\frac{\alpha_f(\overline{T})}{k(\overline{T})} = k(\overline{T})\alpha(\overline{T}) \tag{2.6}$$

where $x = \alpha(\overline{T})$ represents the static relationship between temperature and deflection along the main DOF. If (2.6) is introduced into (2.4) the structure of the mechanical part of the model is given as

$$\overline{m}(\overline{T})\ddot{x} + d\dot{x} + k(\overline{T})x = k(\overline{T})\alpha(\overline{T}) \tag{2.7}$$

2.2.3 Complete Dynamical Model and Unknown Parameters

The complete model, shown in figure 3, is given by combining (2.2), (2.3) and (2.7) as

$$q = G_e(\overline{T})v^2 \tag{2.8}$$

$$C_{th}(\overline{T})\dot{\overline{T}} + G_{cond}(\overline{T})\Delta\overline{T} + G_{conv}(\overline{T})\Delta\overline{T} + G_{rad}(\overline{T})\Delta\overline{T} = q \tag{2.9}$$

$$\overline{m}(\overline{T})\ddot{x} + d\dot{x} + k(\overline{T})x = k\alpha(\overline{T}) \tag{2.10}$$

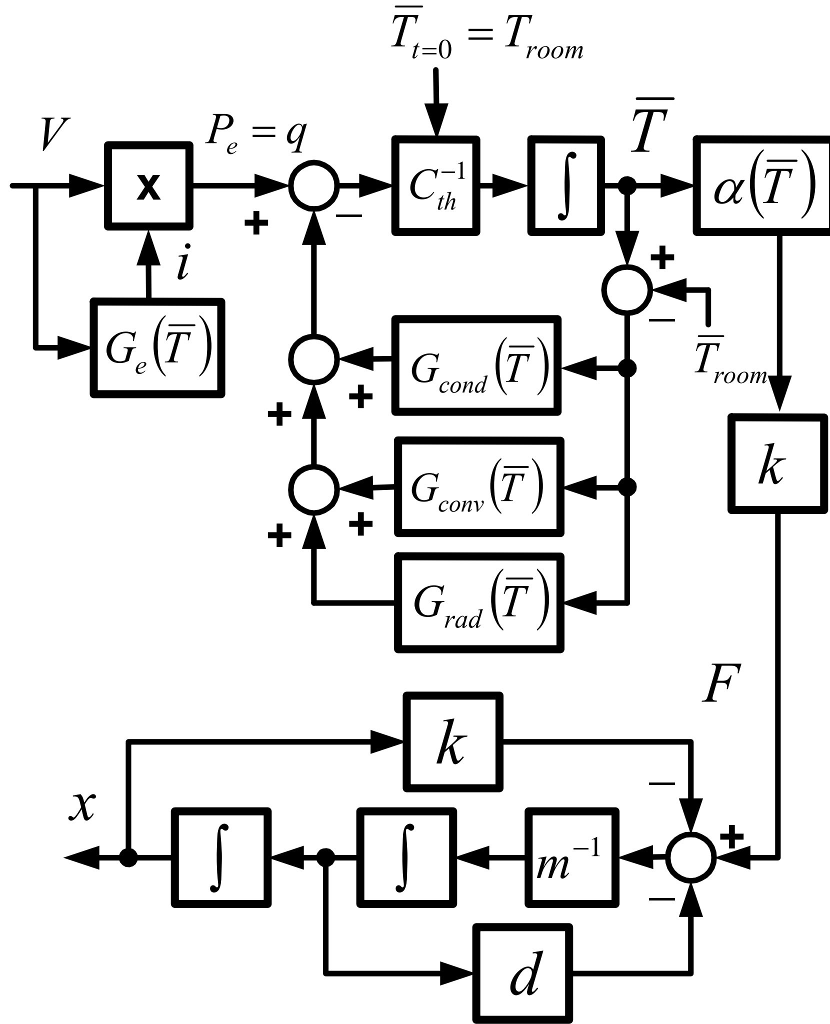

Figure 2.3 Block scheme of the model (2.8), (2.9), (2.10).

with electrical and thermal conductances, thermal capacitance, effective moving mass and stiffness being parameters of the system. Model (2.8)-(2.10) can be put directly into the state-space form [5] with the three states: deflection, x, velocity, $\dot{x}$, and average temperature, $\overline{T}$. Note that the dependence of the parameters on the average temperature makes this model nonlinear.

This modeling procedure, based upon the laws of physics and the set of assumptions applicable on thermal actuators, has yielded the structural form of the dynamical model, and it has also revealed which parameters are important for specifying the dynamics. At this point, the structure of the model is known, but the values of the parameters are still unknown.

2.3 FEA Based System Identification

The unknown system parameters cannot easily be determined using system identification techniques [12] based on experiments with the actual device, since the system is nonlinear, and all the states of the actual actuator are not available as measurements during experimentation. Therefore, we propose using finite element (FE) simulations in a novel fashion to determine the values of the parameters. This is possible to do because all the states in the FE model can be observed as measurements, and they can be computed during the FEA calculations. Three types of FEA should be conducted – a coupled electro-thermal, structural and a modal. To use FEA for parameter identification, it is first necessary to set up an accurate FE model of the MEMS actuator, containing boundary conditions, geometry and accurate and temperature dependent material properties. Material properties of interest are electrical

resistivity, thermal expansion coefficient, specific heat, Young's modulus, Poisson's ratio, and thermal conductivities both for the structural material and the surrounding medium. The FEA outputs include element temperatures, volumes, Joule heat and deflection. Modal FEA is done only to check the assumptions 5 and 6 on negligibility of the higher order modes.

Now that an accurate FEA model and the structure of the dynamical model have been established, it is necessary to define the method to identify the unknown parameters in the dynamical model of (2.8)-(2.10). This requires establishing a connection between the lumped parameters in the model, and the parameters that can be computed using FEA. In the following section, the extracting method is provided.

2.3.1 Electro-Thermal Model Parameter Estimation

Estimation of the electro-thermal parameters consists of applying M different voltage loads to the ETM device and calculating the discrete temperatures, T_i, and generated Joule heat amounts, q_i, of all N finite elements for every j-th load step. The average temperature is determined from the set of temperatures of the finite elements through the manipulation of the thermal capacitance of the device. The average temperature is fictitious quantity that preserves the amount of the energy stored in the system and gives a more intuitive representation of the system.

Assuming room temperature T_{room} all over the body of the device, the thermal capacitance is given as

$$C_{th}\left(T_{room}\right) = \rho V c_m\left(T_{room}\right) \tag{2.11}$$

where ρ is the density of the polysilicon, V is total volume of the actuator and c_m is the temperature dependent specific heat of the structural material. Accordingly, the amount of thermal energy stored inside the body at the room temperature is given as

$$W_{th}(T_{room}) = C_{th}(T_{room})T_{room} = \rho V c_m(T_{room})T_{room} \tag{2.12}$$

At some elevated temperature the temperature distribution is not uniform anymore and energy W_{th} should be calculated by integrating energy all over the body. If the actuator is chopped into the N-finite elements, the total energy for the j-th loading step can be expressed as a sum of the thermal energies stored in each of the N-elements, and it is given as

$$W_{thj} = \rho \sum_{i=1}^{N} c_m(T_j)V_i T_{ij} = \rho \sum_{i=1}^{N} c_{mi}(T_j)V_i T_{ij} \tag{2.13}$$

If one assumes an average temperature, $\overline{T}_j$, that is uniform all over the body of the device, the stored thermal energy is given as

$$W_{thj} = C_{th}(\overline{T}_j)\overline{T}_j = \rho V c_m(\overline{T}_j)\overline{T}_j \tag{2.14}$$

If we equalize (2.13) and (2.14) the amount thermal energy is exactly the same in both cases. This yields

$$\rho V c_m(\overline{T}_j)\overline{T}_j = \rho \sum_{i=1}^{N} c_{mi}(T_j)V_i T_{ij} \tag{2.15}$$

Or, rewritten

$$c_m(\overline{T}_j)\overline{T}_j = V^{-1} \sum_{i=1}^{N} c_{mi}(T_j)V_i T_{ij} = const. \tag{2.16}$$

Equation (2.16) has unique solution ($c_m(\overline{T}_j)$, $\overline{T}_j$) on the interval $T_{\min} \le T_{ij} \le T_{\max}$ for $\forall i$ and $\forall j$, if $c_m(\overline{T}_j)\overline{T}_j$ is monotonic on the same interval. From (2.11), the thermal capacitance at the temperature $\overline{T}_j$ is given as

$$C_{th}(\overline{T}_j) = \rho V c_m(T) = \rho V c_m(\overline{T}_j) \tag{2.17}$$

where $c_m(T)$ is the specific heat as a function of temperature in a polynomial form. If specific heat is assumed independent on temperature, (2.16) reduces to

$$\overline{T}_j = V^{-1}\sum_{i=1}^{N} V_i T_{ij} \tag{2.18}$$

For steady-state conditions $\dot{\overline{T}}_j = 0$, at a specific average temperature $\overline{T}_j$, (2.9) can be rewritten in terms of heat flow as

$$q(\overline{T}_j) = q_{conv}(\overline{T}_j) + q_{cond}(\overline{T}_j) + q_{rad}(\overline{T}_j) \tag{2.19}$$

The total Joule Heat (2.2), (2.8) at the average temperature is simply the sum of the Joule heats generated in the *N*-elements of the finite model geometry, and it is given as

$$q(\overline{T}_j) = \sum_{i=1}^{N} q_{ij} \tag{2.20}$$

Heat removal caused by convection $q_{conv}(\overline{T}_j)$ can be calculated from the FEA results as a sum of convections from the *K* surface areas, A_i, of the surface elements that are at a specific temperature T_i, as

$$q_{conv}(\overline{T}_j) = h\sum_{i=1}^{K} T_{ij} A_i \tag{2.21}$$

Similarly, heat removal caused by radiation can be calculated as

$$q_{rad}\left(\overline{T}_j\right)=\sigma\varepsilon F\sum_{i=1}^{K}A_i\left(T_{ij}^4-T_{room}^4\right) \tag{2.22}$$

After the values of Joule heat (2.20) and the heat flows (2.21)-(2.22) are calculated, the heat transfer caused by conduction can easily be obtained as

$$q_{cond}\left(\overline{T}_j\right)=q\left(\overline{T}_j\right)-q_{conv}\left(\overline{T}_j\right)-q_{rad}\left(\overline{T}_j\right) \tag{2.23}$$

The electrical conductance is determined from the ratio of the Joule heat and the corresponding squared voltage at a specific average temperature as

$$G_e\left(\overline{T}_j\right)=q\left(\overline{T}_j\right)v_j^{-2} \tag{2.24}$$

This FEA step is repeated *M*-times to get all *M*-mean temperatures, $\overline{T}_j$, specific heats $c_m\left(\overline{T}_j\right)$, heat flows, $q\left(\overline{T}_j\right)$, $q_{cond}\left(\overline{T}_j\right)$, $q_{conv}\left(\overline{T}_j\right)$ and $q_{rad}\left(\overline{T}_j\right)$, for each voltage load. The calculated sets of *M* points of electrical conductance (2.24) and heat flows (2.20)-(2.23) can be fitted to the polynomials $G_e\left(\overline{T}\right)$, $q\left(\overline{T}\right)$, $q_{cond}\left(\overline{T}\right)$, $q_{conv}\left(\overline{T}\right)$, and $q_{rad}\left(\overline{T}\right)$, respectively. The corresponding thermal conductances are calculated as

$$G_{cond}\left(\overline{T}\right)=\frac{dq_{cond}\left(\overline{T}\right)}{d\overline{T}};\quad G_{conv}\left(\overline{T}\right)=\frac{dq_{conv}\left(\overline{T}\right)}{d\overline{T}};\quad G_{rad}\left(\overline{T}\right)=\frac{dq_{rad}\left(\overline{T}\right)}{d\overline{T}} \tag{2.25}$$

2.3.2 Mechanical Model Parameter Estimation

To estimate the lumped parameters of the model (2.10), the *M* temperature distributions calculated during the electro-thermal analysis are applied as a body loads

to the mechanical FE model. The parameters to be identified in (2.10) are the function that relates the deflection to the applied temperature, effective moving mass and stiffness constant. Identification of the damping coefficient is omitted in this discussion.

Assuming static conditions $\ddot{x} = \dot{x} = 0$, (2.9) is reduced to

$$x = \alpha\left(\overline{T}\right) \tag{2.26}$$

For the j-th thermal load $\overline{T}_j$, the obtained deflection is calculated using FEA. It is given as

$$x\left(\overline{T}_j\right) = \alpha\left(\overline{T}_j\right) \tag{2.27}$$

The set of calculated points can be fitted into polynomial.

If temperatures of the elements that are applied as a load to the mechanical finite element model provide static, constant force $\alpha_f\left(\overline{T}_j\right)$, and a corresponding deflection, $x\left(\overline{T}_j\right)$. By varying a small load force applied to the ETM device, the deflection is calculated and the stiffness is determined as a ratio between the change in the load force and deflection. Under static conditions the additional force affects (2.9) as follows

$$k\left(\overline{T}_j\right)x_j\left(\overline{T}_j\right) + k\left(\overline{T}_j\right)\Delta x\left(\overline{T}_j\right) = \alpha_f\left(\overline{T}_j\right) + F_L \tag{2.28}$$

$\Delta x\left(\overline{T}_j\right) = x\left(\overline{T}_j\right) - x_L\left(\overline{T}_j\right)$ is the change in the deflection, and F_L is the external load force small enough to ensure $\Delta x\left(\overline{T}_j\right) << x\left(\overline{T}_j\right)$. Equation (2.5) states that $\alpha_f\left(\overline{T}_j\right)$ is balanced by $k\left(\overline{T}_j\right)x\left(\overline{T}_j\right)$. These terms can be eliminated from (2.28) and remaining part determines stiffness as

$$k(\overline{T}_j)=\frac{F_L}{\Delta x(\overline{T}_j)} \tag{2.29}$$

The effective moving mass can be estimated by observing the contribution of the kinetic energy to the motion of the actuator. The main DOF deflection as a function of time can be written as

$$x(t)=x_0 p(t) \tag{2.30}$$

where x_0 is the amplitude of the movement and *p(t)* describes a time depended motion. Assuming similar *p(t)* all over the device the corresponding kinetic energy of (2.30) is given as [80]

$$T_{DOF}(t)=0.5\overline{m}[x\dot{p}(t)]^2\,, \tag{2.31}$$

where $\overline{m}$ represents the effective moving mass of the device. Similarly, the movement of particular finite element inside the device model is given as

$$x_i(t)=x_{i0}p(t), \tag{2.32}$$

with corresponding kinetic energy

$$T_i(t)=0.5m_i[x_{i0}\dot{p}(t)]^2\,. \tag{2.33}$$

Total kinetic energy is given as the sum of contributions of the kinetic energies of the elements all over the device

$$T(t)=0.5\sum_{i=1}^{N}m_i[x_{i0}\dot{p}(t)]^2 \tag{2.34}$$

Equating of the kinetic energies from (2.31) and (2.34) yields

$$0.5\overline{m}x_0^2\dot{p}^2(t)=0.5\sum_{i=1}^{N}m_i x_{i0}^2\dot{p}^2(t) \tag{2.35}$$

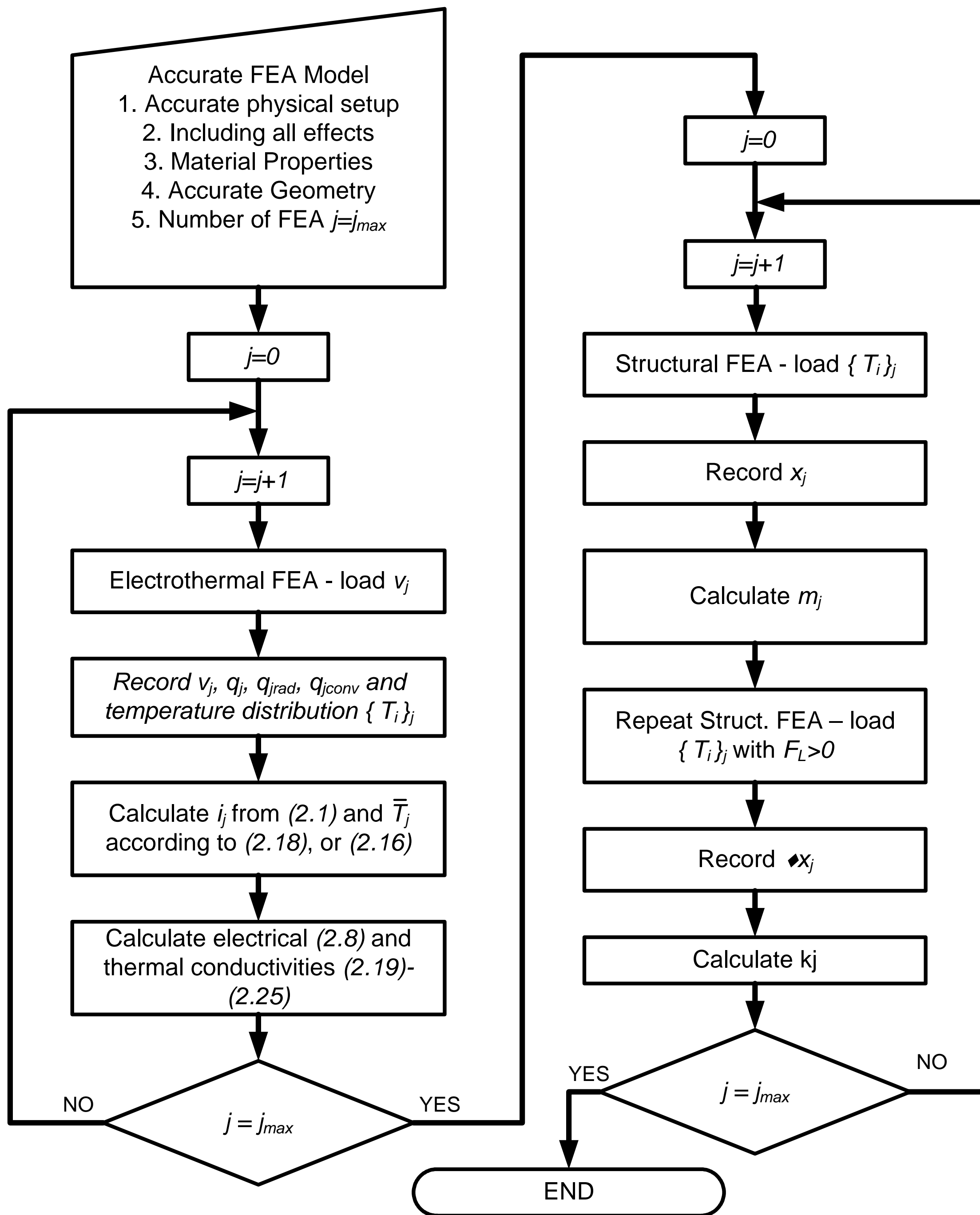

Figure 2.4 Flow chart showing the modeling methodology.

Finally, *p(t)* is assumed to be similar for all elements and therefore can be cancelled out of (2.35) reducing it to

$$\overline{m} = \frac{1}{x_0^2} \sum_{i=1}^{N} x_{i0}^2 m_i \tag{2.36}$$

If effective moving mass is calculated for all *M* loads corresponding to the temperatures $\overline{T}_j$, $j = 1,...,M$, (2.36) is a set of calculated points

$$\overline{m}\left(\overline{T}_j\right) = \frac{1}{x_j^2} \sum_{i=1}^{N} x_i^2\left(\overline{T}_j\right) m_i \tag{2.37}$$

Usually, the influence of temperature on the effective moving mass can be neglected, e.g. $\overline{m}\left(\overline{T}\right) \approx \overline{m}$.

The flow chart for the method of extracting the parameters of the flexible electro-thermal structure is given in figure 2.4.

2.4 Experiments / Verification

The identification procedure and experimental verification of the resulting model are done for two bimorph thermal actuators. The first example, with the experimental results, is taken from [7] in order to verify the method. The actual mismatching of the resulting model and actual actuator, taken as a second example, illustrates a possibility to get a better insight to the dynamical behavior of the device and draw some conclusions. First, the geometry and material properties of the both actuators are given. Next, a suitable FE models are established. The identification method is applied to the models and parameters are extracted. Finally, the resulting models are compared to the experimental results.

The actuators were fabricated using MUMPs process stacking two polysilicon [68] layers on the top of each other. Typical bimorph thermal actuator is shown in figure 2.5. The geometrical parameters of the both actuators are given in table 2.1.

Table 2.1 Geometries of the actuators.

Dimension	Example 1 [μm]	Example 2 [μm]
Length	*200 μm*	*250 μm*
Thickness	*3.5 μm*	*3.5 μm*
Width – hot arm	*3 μm*	*3 μm*
Width – cold arm	*12 μm*	*18 μm*
Width – flexture	*3 μm*	*3 μm*
Length – flexture	*40 μm*	*50 μm*
Gap between arms	*3 μm*	*3 μm*

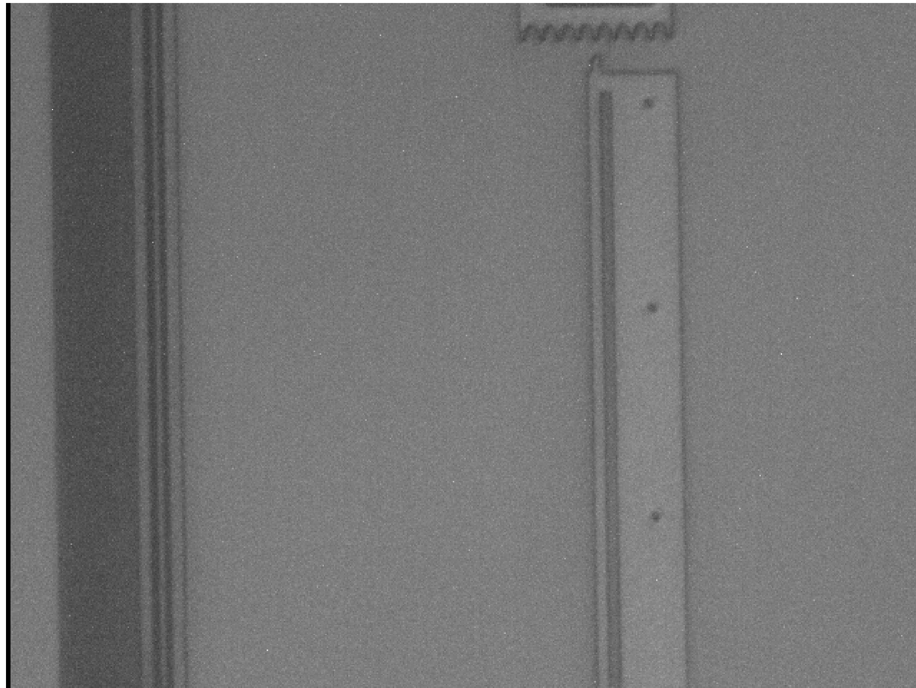

Figure 2.5 The *250 μm* long bimorph actuator.

Material models are taken from [7]. It contains exact estimations of thermal conductivity, electrical resistivity, thermal expansion coefficient and specific heat for polysilicon. The temperature-dependent material properties from [7] are rewritten in the form of polynomials $k_{poly} = c_3T^3 + c_2T^2 + c_1T + c_0$, to be suitable for FEA. Temperature-dependent material properties are given in table 2.2.

Table 2.2 Temperature dependent material properties for temperature range *300-800 K.*

Property	c_3	c_2	c_1	c_0	Unit
$k_{poly}(T)$ [7]	-9.25×10^{-8}	2.37×10^{-4}	-0.238	117.5	$Wm^{-1}K^{-1}$
$\rho_{poly}(T)$ [7]	*0*	4.12×10^{-9}	1.67×10^{-6}	2.2×10^{-3}	Ωcm
$\alpha_{poly}(T)$ [7]	7.4×10^{-15}	-1.65×10^{-11}	1.45×10^{-8}	-5.8×10^{-7}	K^{-1}
$K_{air}(T)$	0	-2.84×10^{-8}	9.35×10^{-5}	6.89×10^{-4}	$Wm^{-1}K^{-1}$

Specific heat is considered constant as only small volume of thermal actuator, e.g. hot arm, gets heated significantly. Specific heat is taken to be $c_p=712\ Jkg^{-1}K^{-1}$ [7]. Structural parameters, e.g. Young's modulus and Poisson's ration are taken to be constant, $E=160\ GPa$ and $\nu=0.22$, respectively.

The electro-thermal FE model was built in ANSYS finite elements software package and is illustrated in figure 2.6. The FE model was established both for polysilicon structure and the surrounding air. Room temperature boundary conditions are applied to the bottom of the model representing the substrate. Voltage is applied

over the pads. Radiation and convection effects were neglected as the maximal temperature reaches *800K* [7], [9].

The structural FE model is similar to the electro-thermal one with the exception of the air region being removed. Temperature distributions calculated during the electro-thermal analysis are applied as a thermal body load to the structural FE model. The pads are fixed.

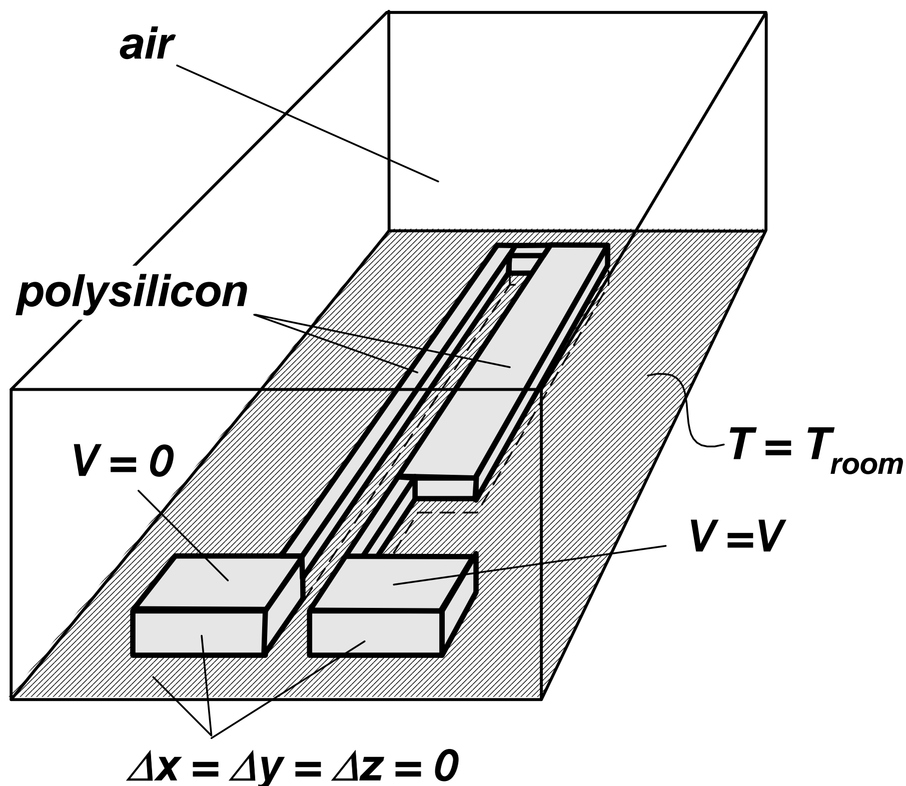

Figure 2.6 FEA Setup.

Assuming no radiation and convection effects are present [9], [7] (2.19) reduces to $q(\overline{T}_j) = q_{cond}(\overline{T}_j)$. However, there are two conduction mechanisms removing heat present in the system – conduction through the actuator structure and through air to the

silicon substrate. Therefore, the (2.19) can be rewritten as $q(\overline{T}_j) = q_{condpoly}(\overline{T}_j) + q_{condair}(\overline{T}_j)$. This is unnecessary step regarding the parameter extraction procedure itself, but distinguishes the two conduction-induced heat removal mechanisms. Following the identification procedure from subsection from figure 2.4, the temperature-dependent parameters are extracted for both actuators. Thermal conductions are shown in figure 2.7 and electrical conductions shown in figure 2.8. Temperature-dependent thermal and electrical conductions from figures 2.7 and 2.8 determine the electro-thermal part of the model (2.8)-(2.9).

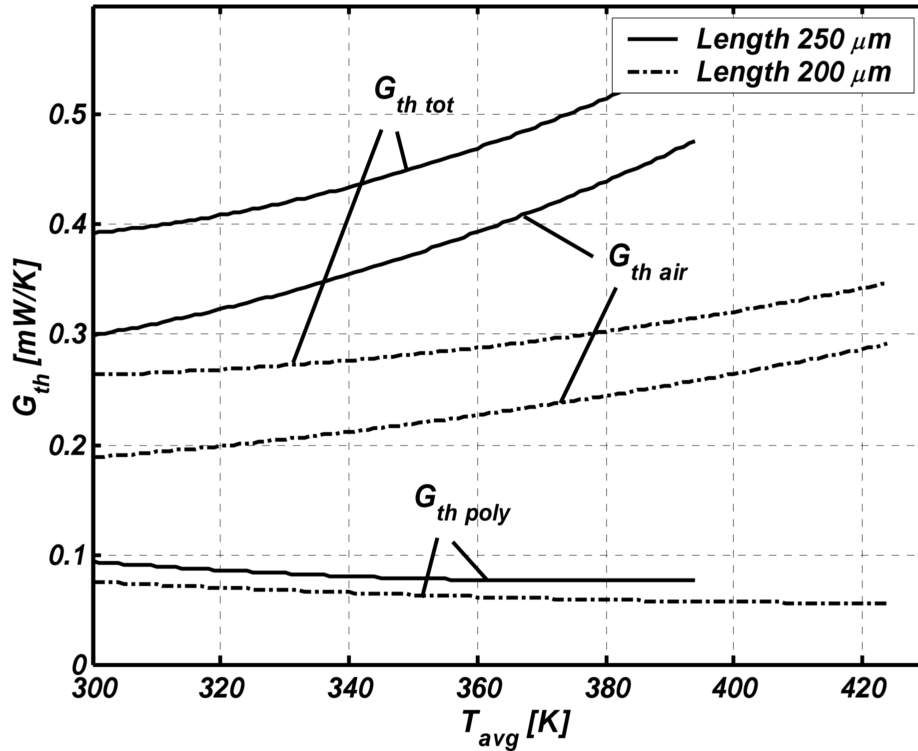

Figure 2.7 Thermal conductions of the air and polysilicon for the actuators in first and second example.

It is interesting to note that about 80% of the heat is removed through air. Consequently, the bending of the actuator that can be caused by initial stress in polysilicon film has tremendous influence on the both static and dynamic behavior of the surface micro-machined thermal actuators.

Following further the extraction procedure, deflection, stiffness, effective masses and corresponding resonant frequencies are determined. The deflections and corresponding forces generated by actuators *F=kx(t)* are shown in figure 2.9. Effective moving mass and the stiffness turns out to be negligibly depended on temperature and are considered to be constant. Finally, the modal analysis is conducted to determine the dominant mode of the devices. Results are summarized in table 2.3.

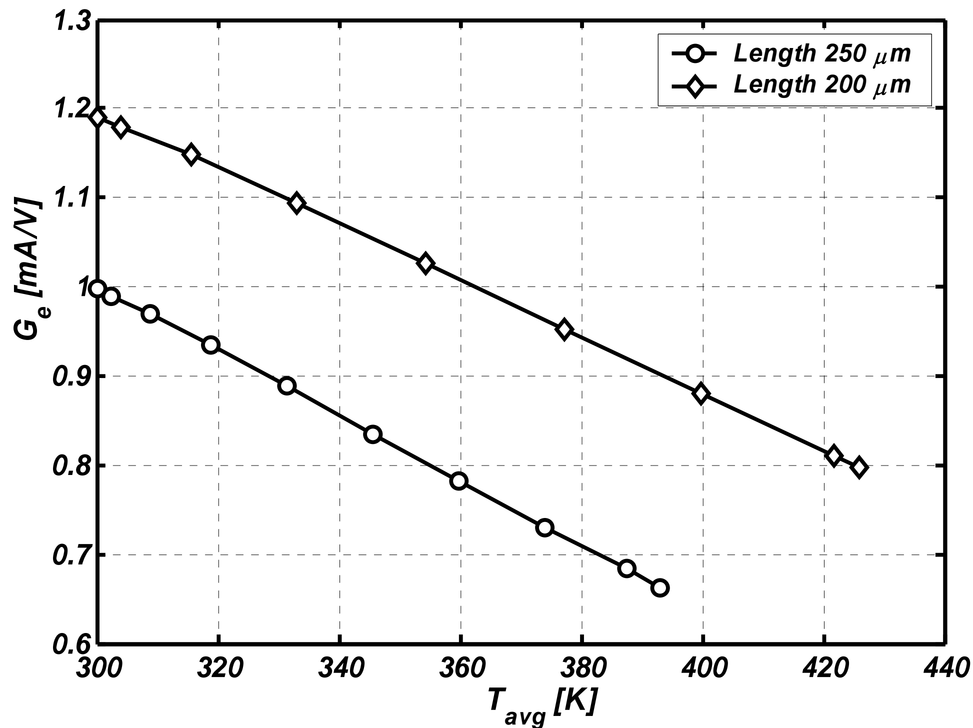

Figure 2.8 Electrical conductions for actuators in both first and second example.

Resonant frequency calculated from stiffness and effective mass of the main DOF basically determines the structural bandwidth of the devices. In both cases, the thermal bandwidth is narrower that the structural one and is around *3.2 kHz* (i.e. $\tau = \omega^{-1} = C_{th} G_{thtot}^{-1} \approx 50 \mu s$). This means the dynamical part of the (2.10) can be neglected, e.g. $\overline{m}\ddot{x} + kx = \alpha_f(\overline{T})$ reduces to $kx = \alpha_f(\overline{T})$.

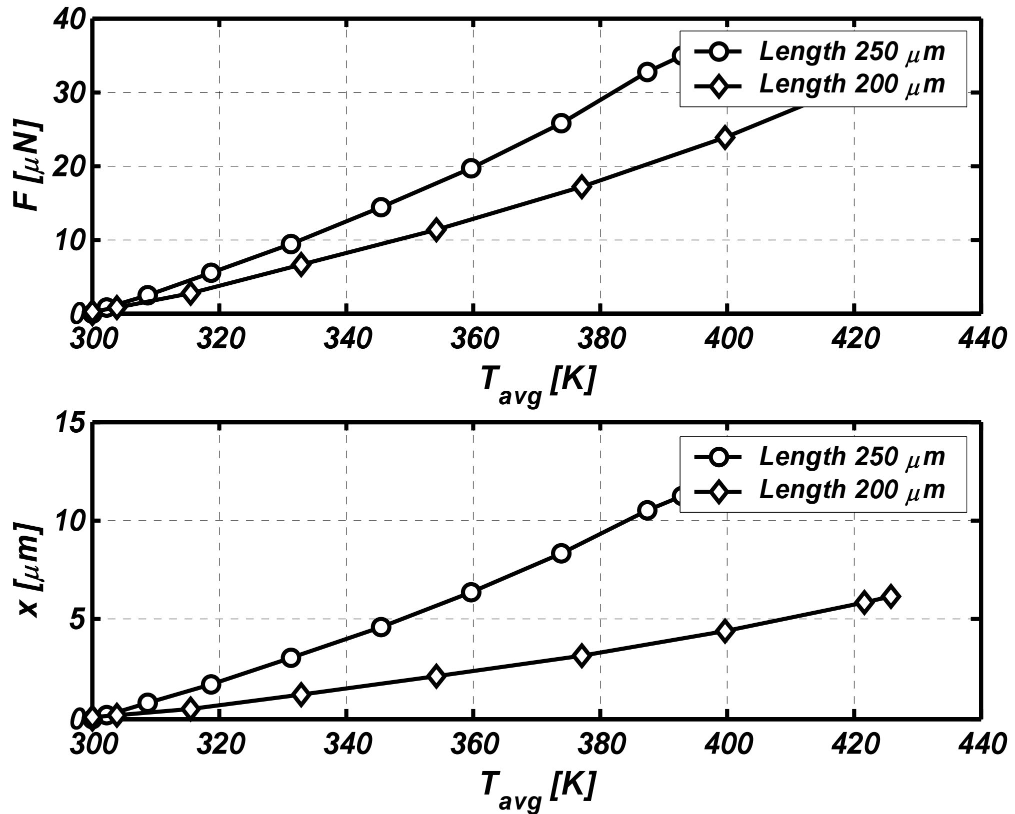

Figure 2.9 Generated force (top) and deflection (bottom) as a function of average temperature for both examples.

Table 2.3 Parameters of the mechanical model.

Parameter	Example 1	Example 2
$\overline{m}$	$0.76\times10^{-11}kg$	$1.35\times10^{-11}kg$
k	$5.37\,Nm^{-1}$	$3.09\,Nm^{-1}$
$f=\frac{1}{2\pi}\sqrt{\frac{k}{\overline{m}}}$	$129\,kHz$ (second mode)	$75\,kHz$ (second mode)
Dominant mode of the device	$80\,kHz$ (1st)	$44\,kHz$ (1st)

Finally, fitting the parameters from figures 2.7, 2.8, and 2.8, and table 2.3 into the (2.8) - (2.10) provides a resulting dynamical model of the device and is given as

$$q = G_e\left(\overline{T}\right)v^2 \tag{2.38}$$

$$C_{th}\dot{\overline{T}} + G_{condpoly}\left(\overline{T}\right)\overline{T} + G_{condair}\left(\overline{T}\right)\overline{T} = q \tag{2.39}$$

$$x = \alpha\left(\overline{T}\right) \tag{2.40}$$

In order to verify resulting model (2.38)-(2.40), the experimental results of the thermal actuator from example 1 were taken from [7]. Three pulses, *0.1*, *0.2* and *0.3ms* long, are applied to the thermal actuator. Deflection was recorded. The MATLAB/ SIMULINK software package was used to obtain the simulation results. Both simulated and experimental results are shown in figure 2.10. The resulting model matches the experimentally obtained deflection almost perfectly.

The experimental and simulated results for the second example are shown in figure 2.11. It is interesting to observe mismatching between the simulated and

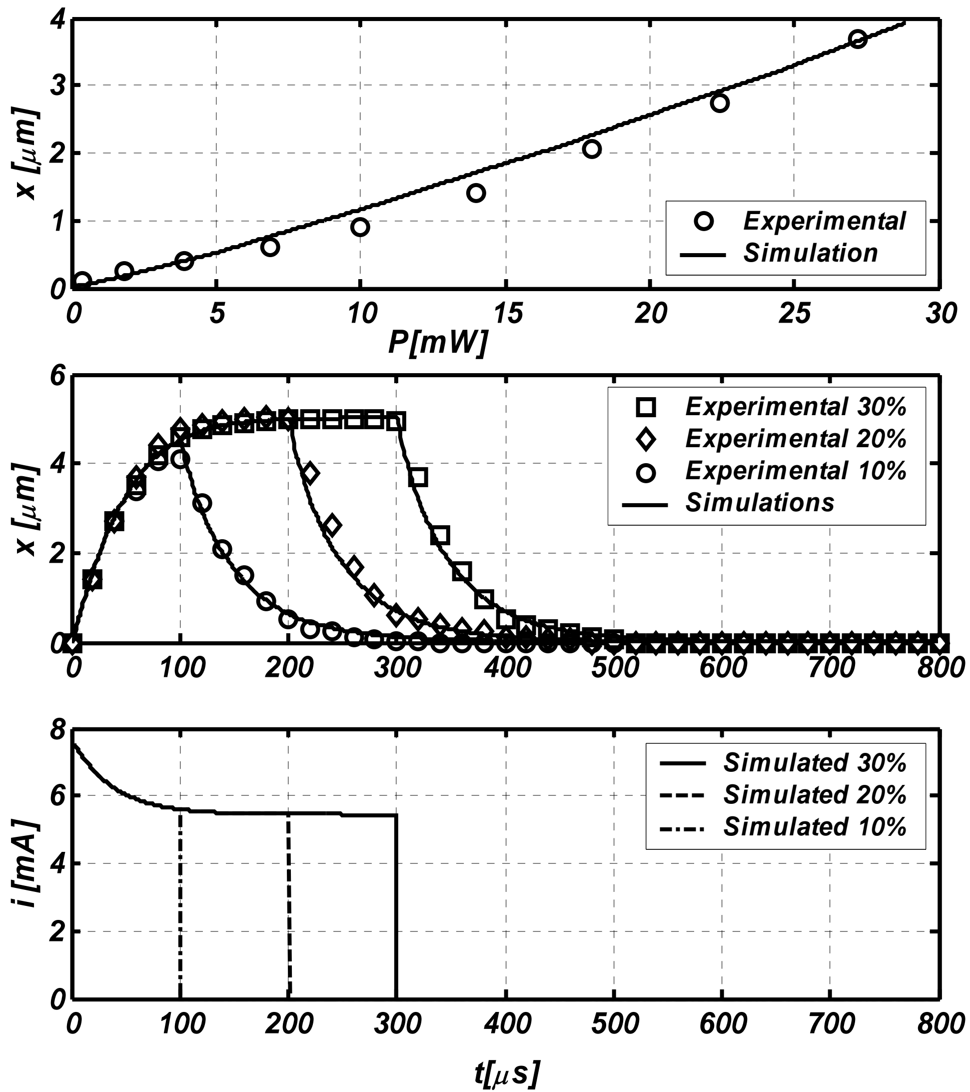

Figure 2.10 Static *P-x* characteristic (top), dynamic response of deflection (middle) and simulated dynamic response of the electrical current (bottom) for the *200 μm* long actuator [7] from example 1.

experimentally obtained deflection given on the bottom of figure 2.11. Voltage and current signals overlap almost perfectly with experimental ones. However, the

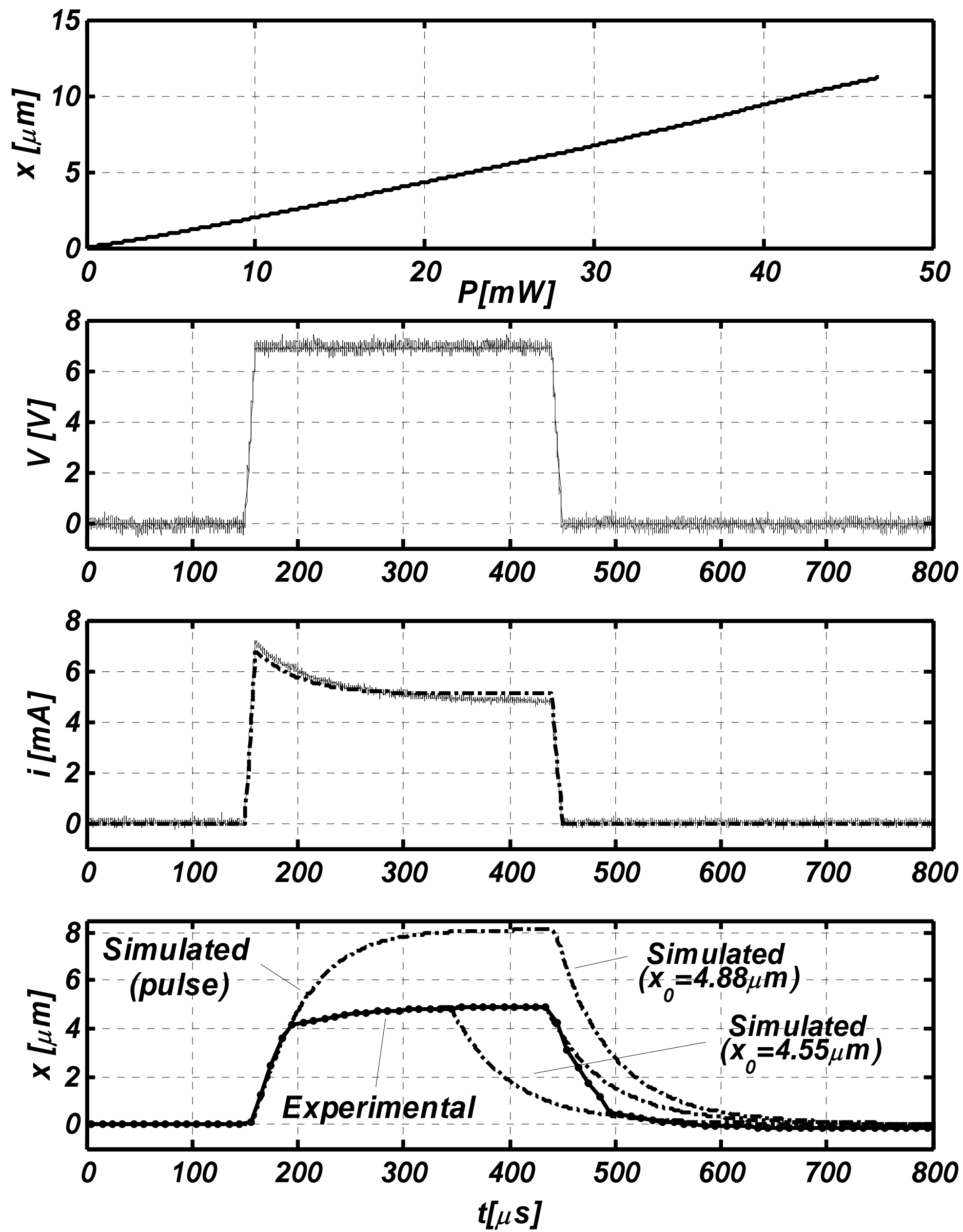

Figure 2.11 Static *P-x* characteristic (top); voltage, current and deflection (bottom) dynamic responses of the electrical current (bottom) for the *200 μm* long actuator from example 2.

simulated deflection response follows the experimental one only during the first phase of the transition period. At $t=200\ \mu s$, the responses abruptly become different. By observing the response one may discuss the reasons for mismatching. For instance, we can guess that if the actuator suddenly bends downwards due to growing thermal stress, the thermal conductance through air should increase, temperature should decrease and steady state deflection should be much smaller than in regular case. During the discharging, the actuator might keep being bended, conductance is still low and the time constant is smaller providing the faster initial response up to a certain point. After that point, the actuator gets back to the initial level, the time constant increases and the response becomes slower, showing the same dynamics as in the case of simulated response. Similarly, the reason for unpredicted behavior could be something else, horizontal thermally induced bending of the hot arm, or for instance friction force caused by actuator touching the substrate. Anyways, the comparison of simulated and experimental response gives deeper qualitative insight into the device.

2.5 Conclusion

A simple identification method for generating a lumped nonlinear dynamical model of an electro-thermo mechanical actuator has been presented. The method is based on a combined analytical and FEA approach. Several simple static FEA are needed to determine the parameters. The model can be evaluated outside the FEA environment by conducting numerical integration of ordinary differential equations. The structure of the model is reduced to a few states – temperature, velocity and position. The fictitious, average temperature is introduced as a state variable to preserve the

energy balance inside the model. Resulting parameters are intuitive and have physical meaning that can be easily related to the geometry and material properties of the device. Qualitative influence of the material properties and geometry can be directly tested on the simplified model. The resulting model was verified with available dynamic experimental results. It is flexible and enables a separate introduction of various phenomena and external forces. If necessary, the similar procedure can be extended to provide the higher order degree of the model. Results are illustrated on the two examples of the MEMS bimorph thermal actuator. The first example shows that the resulting model matches very well with experimental data. The second example illustrates the ability to have a better insight into a model when comparing simulations and experiments.

CHAPTER 3

OPEN-LOOP VS. CLOSED-LOOP CONTROL OF MEMS DEVICES: CHOICES AND ISSUES

3.1 Introduction

Microelectromechanical Systems (MEMS) are mechanically operated and therefore require an actuator to move them. Five basic on-chip actuators technologies have been developed [1]: magnetic, piezoelectric, thermal, optical and electrostatic. Regardless of the applied actuation technique, MEMS are typically driven directly in an open-loop fashion by applying simple input control signals. Straightforward and simple actuation provide the MEMS designer with the improved device designs as a single choice to achieving better dynamical behavior. Hence, MEMS actuators have traditionally been gradually modified and improved in terms of mechanical design, suitable open-loop driving signals, and better area-efficiency [13]-[15], [62]-[63], [71]-[73], [84], [86].

On the other hand, the requirements for better dynamical behavior of the MEMS devices in terms both of speed of response and precision have resulted in the gradual introduction of improved actuation approaches. If the simple input signal is made more complex, taking care of the system dynamics, the approach results in the so-called "pre-shaped control" [2], [16]-[17]. The dynamic model of the device is used to construct a

pre-shaped input signal that enables the device to achieve better and faster dynamical performance.

However, pre-shaped actuation schemes are sometimes not enough. The lack of accurate models, fabrication inconsistencies, and lack of repeatability of the device parameters, compounded by special requirements on the dynamical behavior, all call for the use of closed-loop control design [17]-[21], [49]. The first MEMS devices incorporating feedback were closed-loop sensors, with the objective of enhancing measurement accuracy [1]. An increase in complexity, device integration, and sophistication level of MEMS devices demands equally sophisticated integrated control systems. Unlike macro mechanical systems where the implementation of the feedback is relatively simple, it is quite problematic in the MEMS case. The presence of sensor dynamics, fast high-frequency system dynamics, and requirements for the integration of the control system on the actual MEMS device have introduced additional challenges for feedback control design.

Both input shaping and closed-loop approaches significantly improve the dynamical behavior of MEMS and both strategies have their own advantages and disadvantages. The choice of driving strategy depends on several factors – the purpose of the device, complexity of the sensor implementation, available space, complexity of the electronic circuitry, dynamics of the device and sensitivity of the dynamical response to the device parameters.

The purpose of this chapter is to compare and contrast open-loop and closed-loop design of MEMS control systems, detailing the design issues and choices. The

experimental results, obtained from implementation of the pre-shaped open-loop and closed-loop control methods, were used to compare the two approaches and point out their advantages and disadvantages. It is found that with minimum additional implementation complexity, the closed-loop approach speeds up the system and improves its dynamical response. Criteria for choosing between the two control approaches is also established. As a case study, an optical MEMS device (MOEMS) actuated by the electrostatic comb drive [22] was used. The actuator shuttle has a light-modulating shutter attached to it. Optical feedback was used to reconstruct the position of the shuttle, which cannot be directly measured. The device can be used both as an optical switch (OS) [46]-[47] or variable optical attenuator (VOA) [3]-[4], [23], [70],[87].

The description of the actual device is given in section 3.2, a short overview of its mathematical model in section 3.3, an experimental analysis of open and closed loop approaches is given in section 3.4. Discussion on small scale feedback, sensing and the choice of actuation strategy is given in section 3.5. At the end, some conclusions are drawn.

3.2 System Description

A MOEMS device similar to the actual device analyzed in this paper is shown in figure 3.1. Detailed geometry of the device is given in figure 3.2 [4]. The device was fabricated using Deep Reactive Ion Etching (DRIE) [24], [76]-[77] on SOI wafers with a 75um thick structural layer.

The device consists of two electrostatic comb drive actuators, a suspension mechanism, the body of the device also called a shuttle, and a shutter. A voltage applied to the comb drive actuator generates a force that moves the shuttle. The shutter which is attached to the shuttle then cuts and modulates a light beam.

The shuttle consists of the shutter and comb support frames, *508 μm* and *1430 μm* long, respectively. Support frames are made lighter by creating cavities in the structures (see figure 3.2). The widths of all features of the shuttle are *2 μm*. The shutter itself is *3 μm* wide and *190 μm* long. There are *158* fingers on the comb drive each having a width of *2 μm* and a length of *27 um*. The gap between the fingers is *2.5 μm*, with an initial overlapping of *5 μm*. The width of the folded beams of the suspension is *3 μm* with lengths *862.5 μm* and *854.5 μm* for the outer and inner beams respectively.

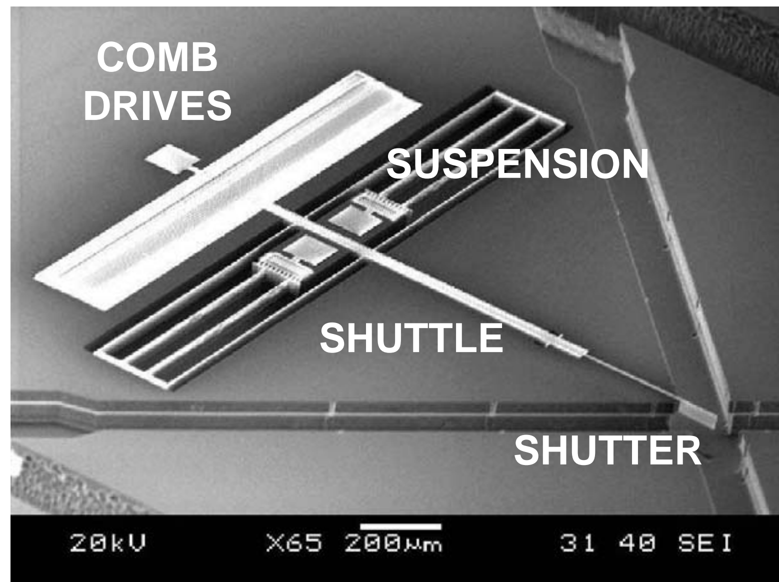

Figure 3.1 SEM image of the MEMS VOA showing electrostatic comb drive, moving shuttle with attached shutter, and optical fiber channels.

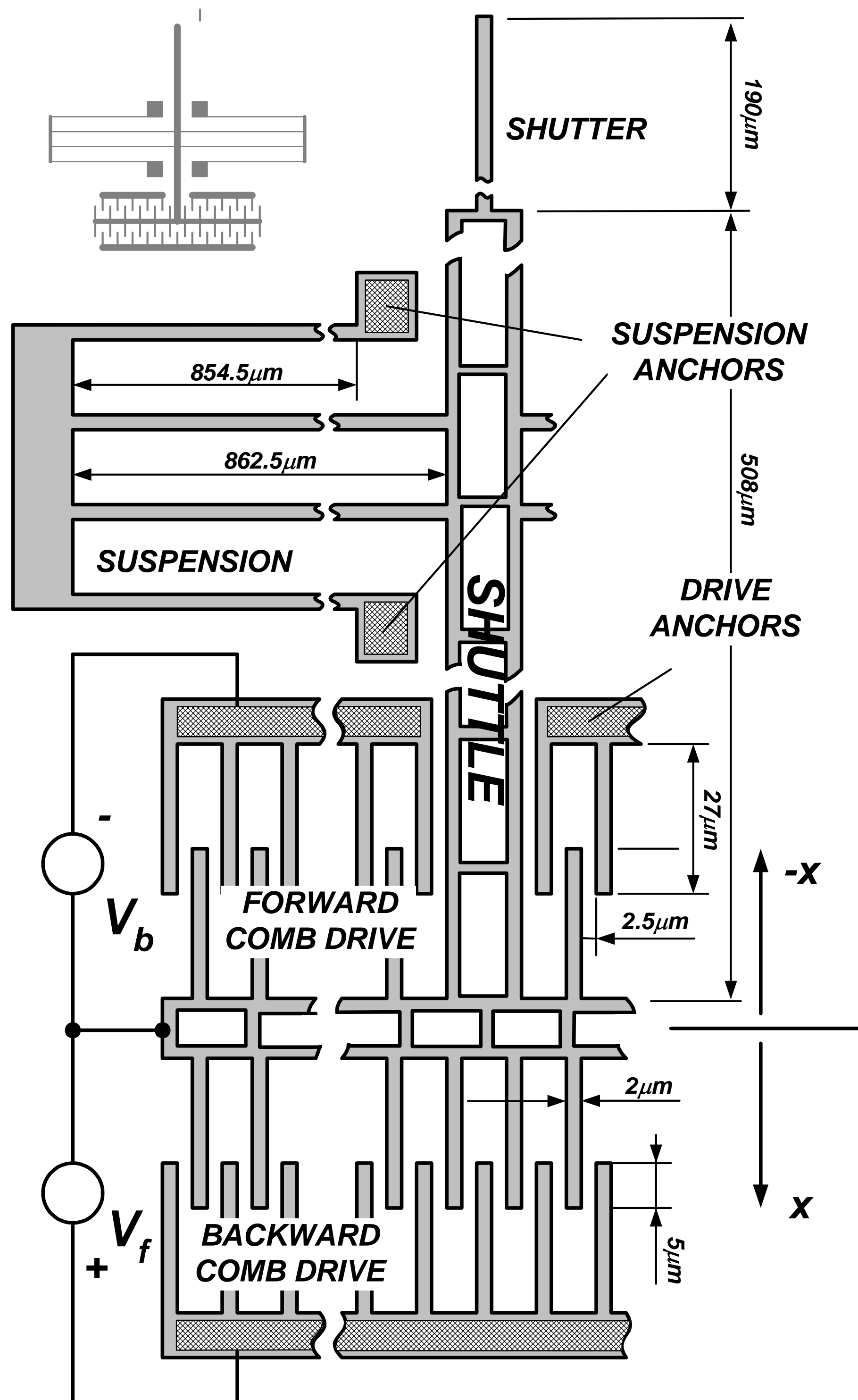

Figure 3.2 Design and geometry of the device from figure 3.1.

The experimental setup is shown in figure 3.3. The voltage applied to the actuator is separated and distributed to both forward (V_f) and backward (V_b) combs. The movement of the actuator modulates the light generated by laser diode and the light is sensed by photo-detector. The voltage from photo-detector V_{PD} is processed to determine the deflection x.

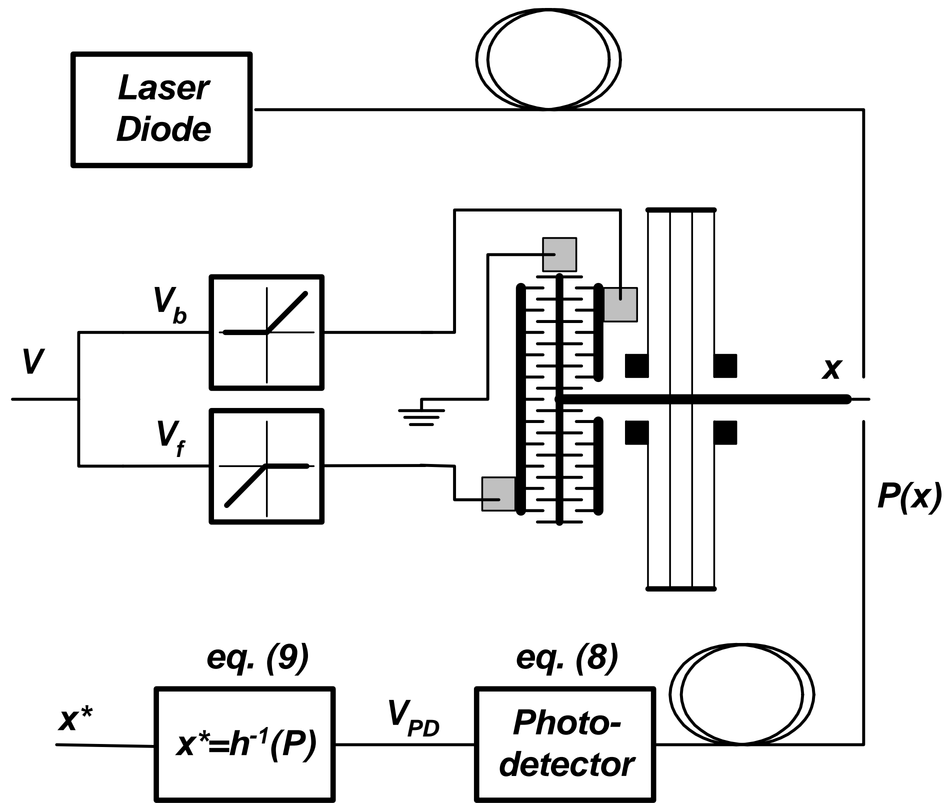

Figure 3.3 Experimental setup of the VOA.

3.3 Mathematical Model

A simplified model is used to represent the dynamic behavior of the device. It provides adequate insight and is sufficient for the purpose of the controller design. The

parameters of the model are identified analytically, but tuned experimentally. The dynamical model of the system is given as [17], [3], [25]

$$m\ddot{x} + d\dot{x} + kx = f_f\left(V_f, x\right) - f_b\left(V_b, x\right) \tag{3.1}$$

$$V_{PD} = h(x) \tag{3.2}$$

where x is the shutter position, m is the effective moving mass of the shuttle, d is damping, k is stiffness of the suspension, f_f and f_b are the electrostatic forces, V_{PD} is a photo-detector voltage, and h is a sensing function relating position and photo-detector voltage. Driving voltages $V_f \geq 0$ and $V_b \leq 0$ do not overlap in time, e.g. when $V_f > 0 \Rightarrow V_b = 0$ and $V_b < 0 \Rightarrow V_f = 0$. Therefore, we introduce $V = V_f + V_b$ which will be used frequently throughout this paper. The parameters of the model (3.1) and (3.2), that have to be estimated are m, k, d, f_f, f_b, and $h(x)$.

Existing empirical models are readily available to estimate both effective moving mass and stiffness for structures with typical suspensions. According to [4] the effective mass of the VOA relative to the main degree of freedom (DOF) x can be expressed as

$$m = m_{sh} + 2.74 m_b \tag{3.3}$$

where m_{sh} is the mass of shuttle and m_b is the effective mass of the eight suspension beams. Taking into account (3.3), the density of silicon $\rho_{Si} = 2.3 \times 10^3 kgm^{-3}$ and geometry given in figure 3.2, the effective mass of the system is $m = 7.75 \times 10^{-9} kg$.

The VOA suspension stiffness is assumed to be linear and is given by [4], [78]-[79]

$$k = 24\frac{EI_Z}{L^3} = 2ET\left(\frac{BW}{BL}\right)^3 \tag{3.4}$$

where E is Young's modulus ($E=160\ GPa$), BW width of the suspension beams, BL is length of suspension beams, and I_Z is the moment of inertia around the deflecting axis of the beam. Calculation, using (3.4) and the geometry in figure 3.2, gives $k=1.05Nm^{-1}$.

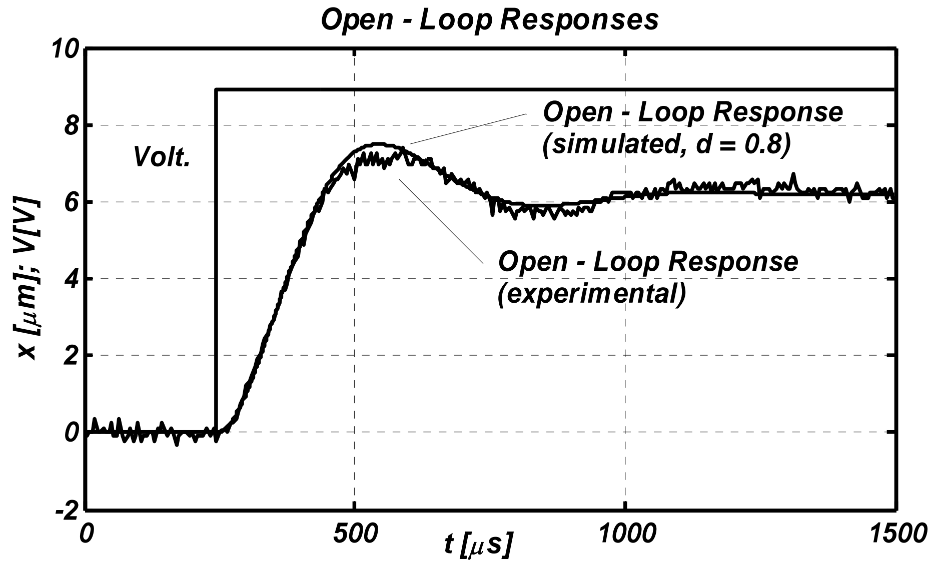

Figure 3.4 Open loop response of the simulated model (3.10), (3.11), compared with the experimental one.

Damping is the most difficult parameter to determine analytically, even through the use of FEA [12]. The reason for this is the number of different complex mechanisms that cause it, including friction, viscous forces, drag, etc. [12],[26]. Hence, experimental data is used to estimate damping of the system. Assuming that the damping coefficient is unknown, but constant, and comparing the simulated and experimental responses as shown in figure 3.4, the damping coefficient turns out to be $d_0 = 8\times10^{-5}kgs^{-1}$.

Next, the electrical part of the model is derived. This derivation was accomplished only for the forward comb drive. However, as experimental results will prove later, it is equally valid for the backward force, i.e., $f_f=f_b$.

In order to get the model of force acting between the two comb drive electrodes, the capacitance of the comb drive as a function of position should be determined first. The capacitance is calculated as a sum of parallel capacitances among pairs of comb electrodes. The total capacitance, as a function of the position x, is given by [4]

$$C(x)=\frac{\varepsilon_0 A}{d_G}=\frac{2n\varepsilon_0 T}{d_G}(x+x_0) \tag{3.5}$$

where ε_0 is the dielectric constant of a vacuum, n is the number of the movable fingers of the electrode, T is the thickness of the structural layer, d_G is the gap between fingers, and x_0 is the initial overlapping between the electrodes. The capacitance of the comb drive calculated at the rest position is $C(0)=0.42pF$. It increases as shuttle moves forward and decreases as it moves backwards. The electrostatic force between the electrodes of the capacitor is given as [12]

$$f_f(V_f,x)=\frac{1}{2}V_f^2\frac{\partial C}{\partial x} \tag{3.6}$$

which, combined with (3.5), yields

$$f(V_f,x)=\frac{n\varepsilon_0 T}{d_G}V_f^2=k_e V_f^2 \tag{3.7}$$

When calculated, the value of the electrostatic constant, k_e, is $41nNV^{-2}$. Note that the electrostatic force of the comb drive does not depend on its deflection. This is a typical property of comb drives.

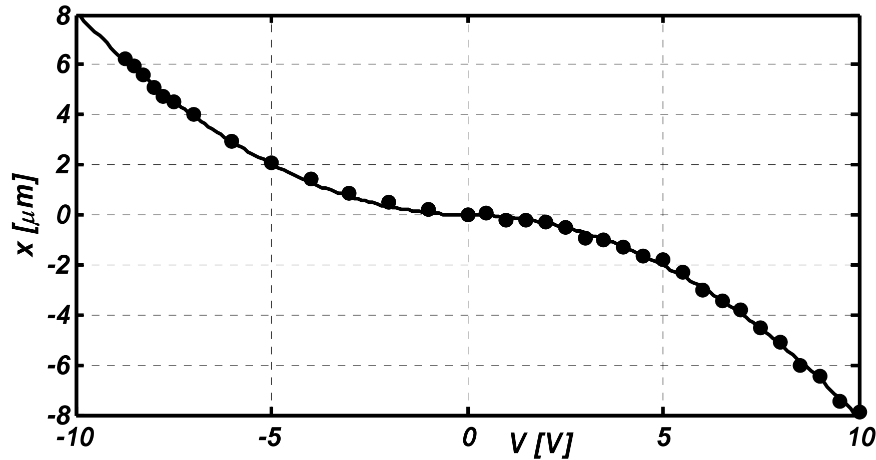

Figure 3.5 Experimental deflection vs. voltage relationship, representing the input nonlinearity of the system.

The electrostatic constant (3.7) can be verified by conducting static experiments, (i.e., $\ddot{x} = \dot{x} = 0$). Static conditions reduce (3.1) and (3.6) to $x = (k_e/k)V_f^2$ yielding the experimental deflection-voltage curve shown in figure 3.5, which fits into $x[\mu m]=-0.081[\mu m V^{-2}]V^2$. The analytically obtained value of k_e/k turns out to be half of the experimental value (i.e., $-0.039\mu m V^{-2}$). As the stiffness (3.4) can be determined very accurately, the calculation for k_e (3.7) seems to be inaccurate. The reason for this can be attributed to the finite aspect ratio of the silicon structure fabricated by DRIE, which increases the value of the capacitance (3.5) several times [27]. As a consequence, the experimental results of k_e/k are used in this paper.

The maximum static voltages that can be applied to the electrodes before they exhibit lateral pull-in are $V=V_b=-8.96\ V$ and $V=V_f=10.1\ V$.

The setup for determining the optical model (3.2) is shown in figures 3.3 and 3.6. The light beam is intercepted by the shutter, increasing and decreasing the

throughput of the light. Analytical techniques were developed to determine the relationship (3.2) theoretically in [3], [17], [19]. However, due to dissimilarities between the predicted model and an actual experiment, further discussion relies on the experimental results.

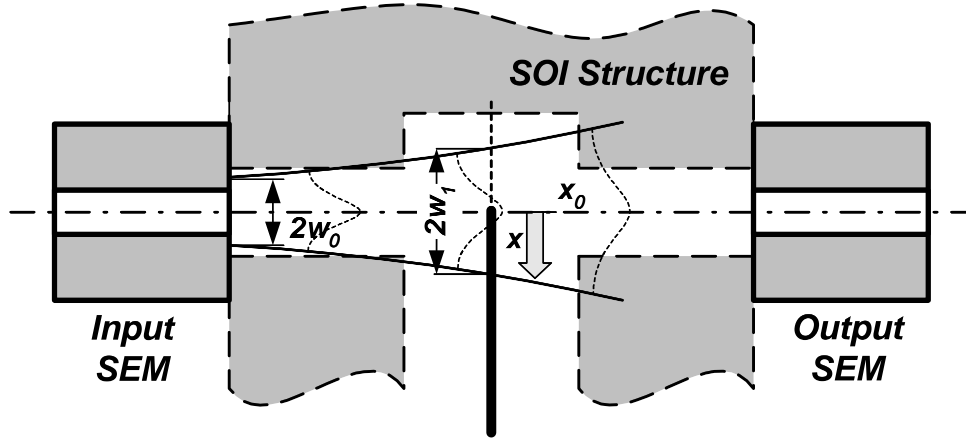

Figure 3.6 Optical Position Measurement [3], [19].

The experimentally determined relationship, $V_{PD}=h(x)$, is shown in figure 3.7. Experimental data from figure 3.7 is curve-fitted using a 4-th order polynomial for $0 \le x \le 7\mu m$ as

$$V_{PD}[V] = a_4 x^4 + a_3 x^3 + a_2 x^2 + a_1 x + a_0 \tag{3.8}$$

with the following parameters: $a_4 = 5.73\times10^{-5}\,V\mu m^{-4}$, $a_3 = -0.0024\,V\mu m^{-3}$, $a_2 = 0.018\,V\mu m^{-2}$, $a_1 = 0.03\,V\mu m^{-1}$, and $a_0 = -0.69\,V$. The light intensity is linearly related to the V_{PD} with its minimum corresponding to $V_{PD}=-800mV$ and its maximum corresponding to $0mV$.

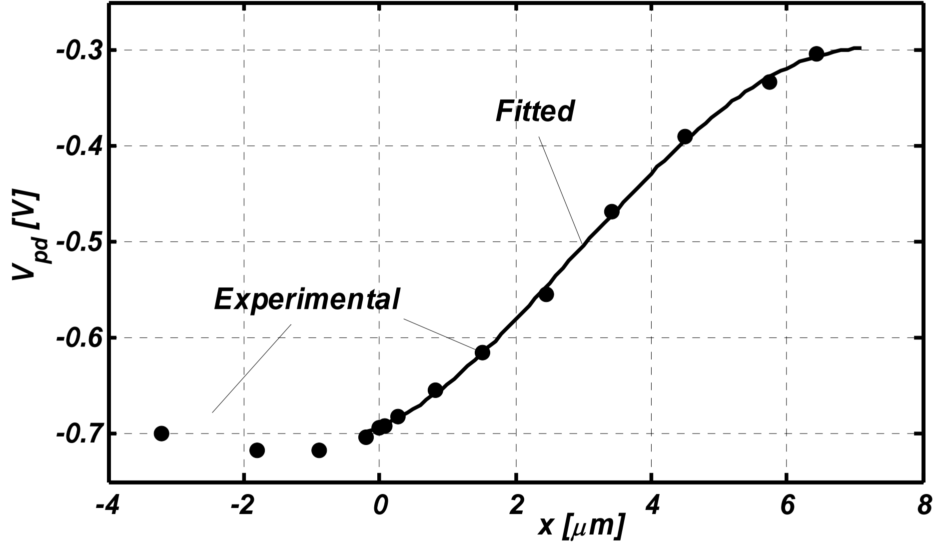

Figure 3.7 Position –Optical Intensity Characteristics (3.2) – output nonlinearity of the system.

In order to reconstruct the position from the optical power, which is necessary to measure deflection, the inverse of (3.2) has to be determined. The inverse of (3.2) inside the interval $-0.7V \leq V_{PD} \leq -0.3V$, and for $x \geq 0$, can be approximated using a third order polynomial as

$$x^*[\mu m] = b_3 V_{PD}^3 + b_2 V_{PD}^2 + b_1 V_{PD} + b_0 \tag{3.9}$$

where $b_3 = 116\,\mu m V^{-3}$, $b_2 = 175.5\,\mu m V^{-2}$, $b_1 = 100\,\mu m V^{-1}$, and $b_0 = 23.6\,\mu m$.

In summary, the model (3.1) and (3.2) can be populated by parameters by putting together the results calculated from (3.3), (3.4), (3.7), (3.8), and figure 3.4. The complete model is given as

$$7.75\times10^{-9}\ddot{x}+8\times10^{-5}+1.05x=8.2\times10^{-8}V^{2} \tag{3.10}$$

$$V_{PD}[V]=5.73\times10^{19}x^{4}-2.4\times10^{15}x^{3}+1.8\times10^{10}x^{2}+3\times10^{4}x-0.69 \tag{3.11}$$

Note that the deflection x from (3.10) and (3.11) is expressed in meters. The model given in (3.10) and (3.11) closely matches experimental results. The simulated and experimental open-loop step responses are shown in figure 3.4.

3.4 Open vs. Closed-Loop Control

In this section, the comparison between the pre-shaped open-loop and closed-loop driving approaches is given for the actual device. Both experimental and computer simulated results are used to illustrate the differences. The simulated results were based on model (3.10) and (3.11). Simulations were accomplished in *MATLAB / SIMULINK*. Experimental data was collected using a *Tektronix TDS 2014* oscilloscope. The control system was implemented using a *dSpace 1104* fast control prototyping system.

3.4.1 Open-Loop Strategies

Direct open-loop driving of the actuator is straightforward. An applied voltage step causes deflection of the actuator. The resulting step response is shown in figure 3.4. The rise time is *190μm* and the overshoot is *17%*. The settling time is approximately *550μs*.

Next, the simple step input signal is modified resulting in pre-shaped open-loop driving. The idea behind pre-shaping is to obtain a faster, aperiodic dynamic response. Here, different voltage pulses are combined to obtain a signal with a high voltage spike at the beginning and a trailing steady state voltage as shown in figure 3.8. A zero-voltage period exists between the initial spike and the steady state voltage. The signal is

defined by the amplitude of the initial spike, the steady state voltage and the values of the three triggering instants. Triggering instants define the beginning and the end of the initial spike as well as the beginning of the steady state voltage value.

For a specified steady-state voltage and a given maximum amplitude of the voltage spike, this input signal will give the fastest possible aperiodic response. The rise time of the response is determined by the difference between the third triggering instant. Detailed discussion of a similar signal shaping technique is given in [28].

The simulated results for different amplitudes of initial spikes are shown in figure 3.8. In order to speed up the response, the amplitude of the initial spike is increased. Consequently, the responses grow faster and all triggering instants are moved closer to the first one. The increase in rise time with respect to the amplitude of the initial spike is larger at low voltages than it is for higher voltages. On the other hand, when both the amplitude of the spike and the steady state voltage are the same, (e.g. *8.9V*) the rise time is the same as the direct open-loop's rise time; however, the response is aperiodic. The advantage of uniform voltage levels is that they enable simple implementation.

The implementation of the signal "pre-shaper" is shown in figure 3.9. Monostable multivibrators were cascaded to obtain desired triggering instants. Pulses generated by the multivibrators were collected by a summing amplifier. The particular pulse amplitude was determined by the corresponding input resistor. The amplifier output was delivered directly to the actuator.

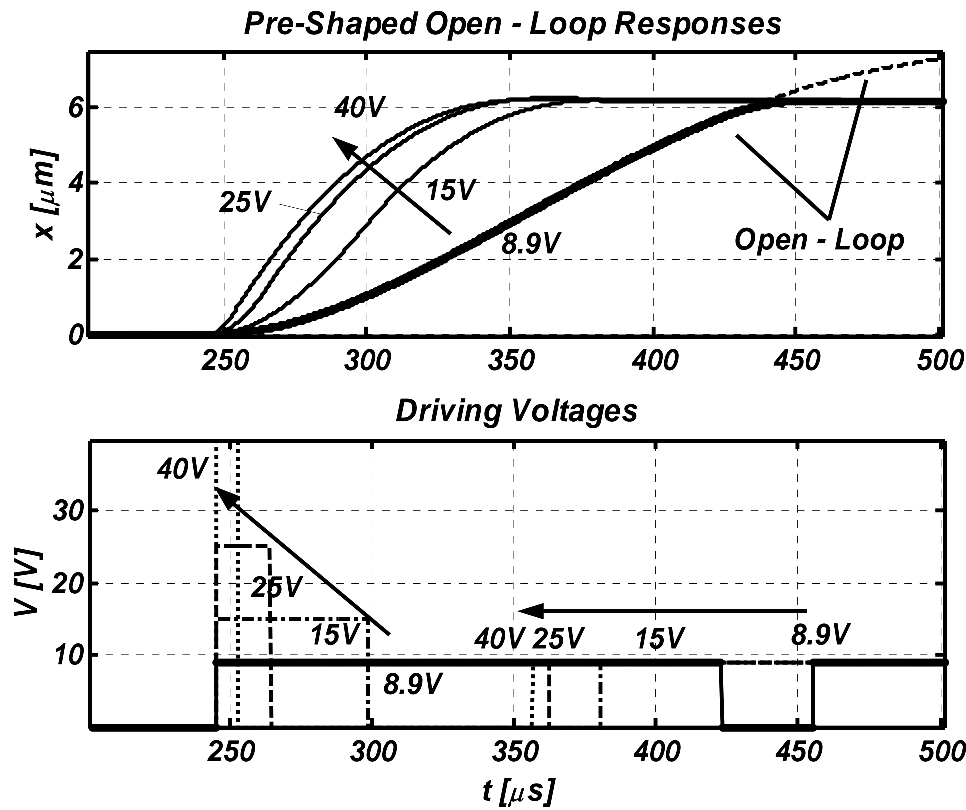

Figure 3.8 Pre-shaped open loop responses. All signals have the same voltage level (simulation results).

Experimental results are compared with those obtained from simulations and are given in figure 3.10. The simulated open-loop step response is shown for reference. Both simulated and experimental results are well matched having a similar rise time ($\sim 100\mu s$). As can be seen, unexpected residual oscillations are present in the experimental response. Examining the frequency of oscillations reveals that they are not a consequence of the dominant dynamics but of higher order vibration modes.

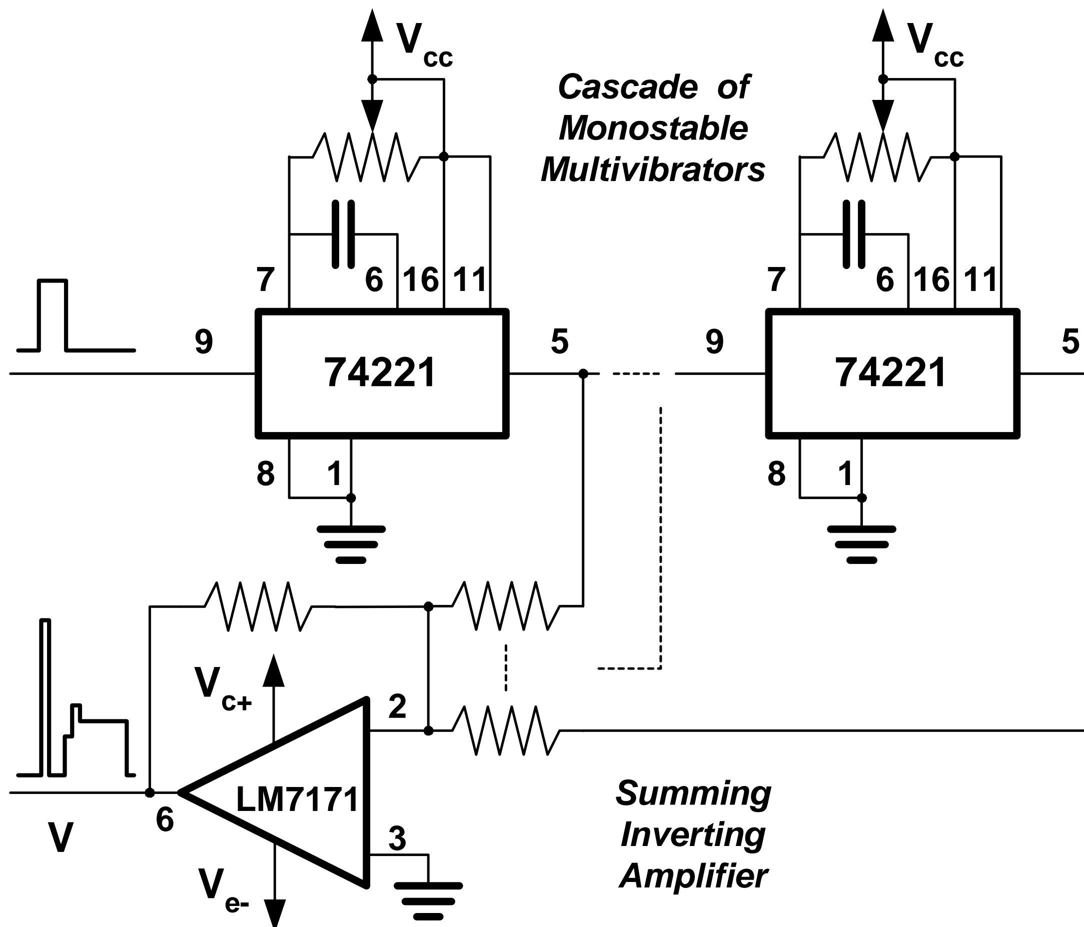

Figure 3.9 Cascaded multivibrators and summing op-amp for assembling the pre-shaped input signal.

In order to suppress residual oscillations while keeping the faster rise time, the pre-shaped input signal was reshaped once again by adding two more multivibrators. The results are shown in figure 3.11. Unfortunately, the situation was not significantly improved and the oscillations were not eliminated.

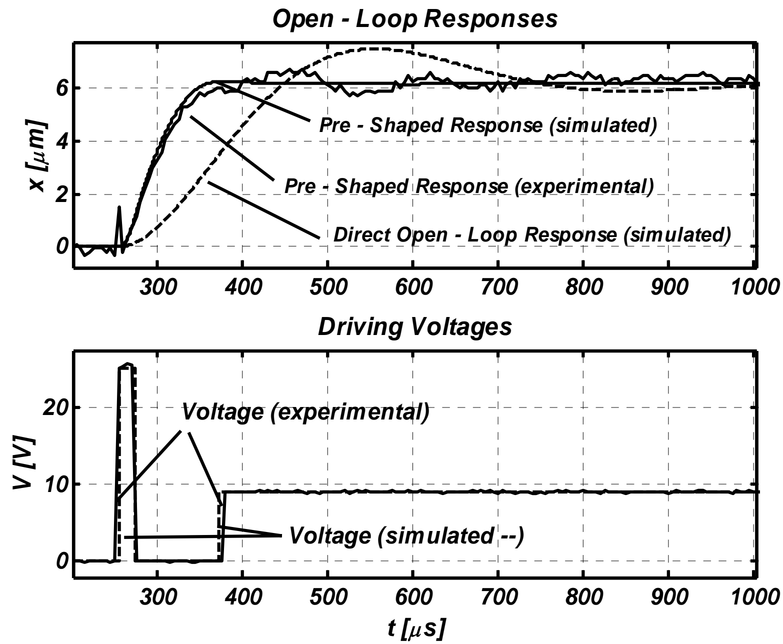

Figure 3.10 Pre-shaped open loop response – different voltage levels and dependence of the speed on maximal available voltage (experimental and simulated results).

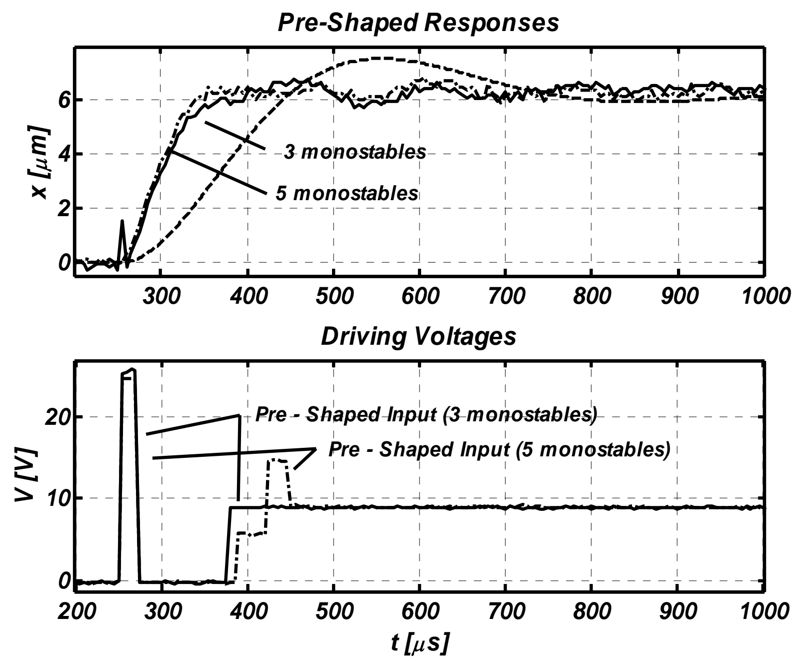

Figure 3.11 Pre-shaped open loop response with and without the compensation of the higher modes (experimental results).

3.4.2 Closed-Loop Actuation

The next step is the implementation of the feedback controller. Optical feedback (9) was used to measure the position as shown in figure 3.3. The controller contains feed-forward (FF) and feedback Proportional Derivative (PD) loop, and is shown in figure 3.12. The detailed design of the controller is provided in [19]. Realization was accomplished using a fast control prototyping dSpace system [54]. The sampling time was *12μs*. Under assumption of perfect position reconstruction, e.g. $x = x^*$ in (3.9), the control action is given as

$$u_{ff} = (k/k_e)x_d \; u_{fb} + (1/N)\dot{u}_{fb} = K_P(x_d - x) + K_D(x)(\dot{x}_d - \dot{x})$$

$$u = u_{ff} + u_{fb} \qquad u \geq 0 \tag{3.14}$$

$$V = \sqrt{u_{ff} + u_{fb}} \qquad 0 \leq V \leq 15V$$

with $K_D = 3.2 \times 10^3$ and $K_D = 3.2 \times 10^7$.

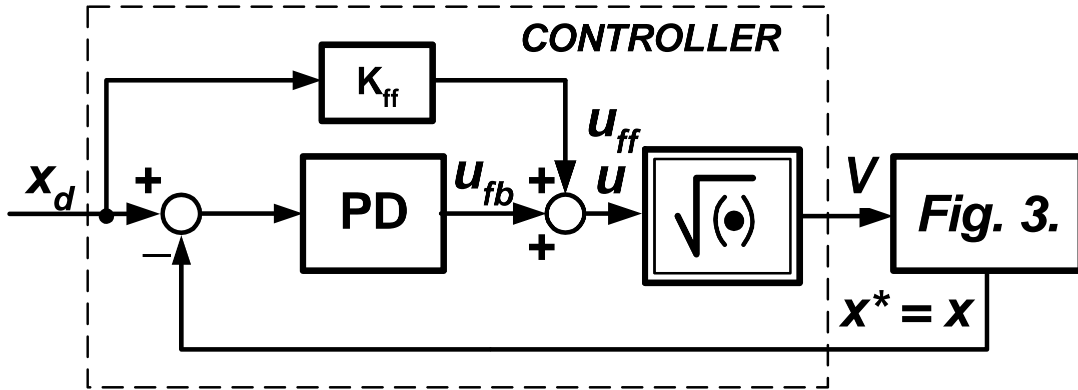

Figure 3.12 Controller Structure [17], [19].

The feed-forward gain ensures reaching the vicinity of the desired deflection. Proportional and derivative gains mitigate the remaining error, speed up the response and shape the signal, ensuring the aperiodic response. Experimental responses of the closed-loop system to the step input signal is shown in figure 3.13. The open-loop response is also shown for comparison.

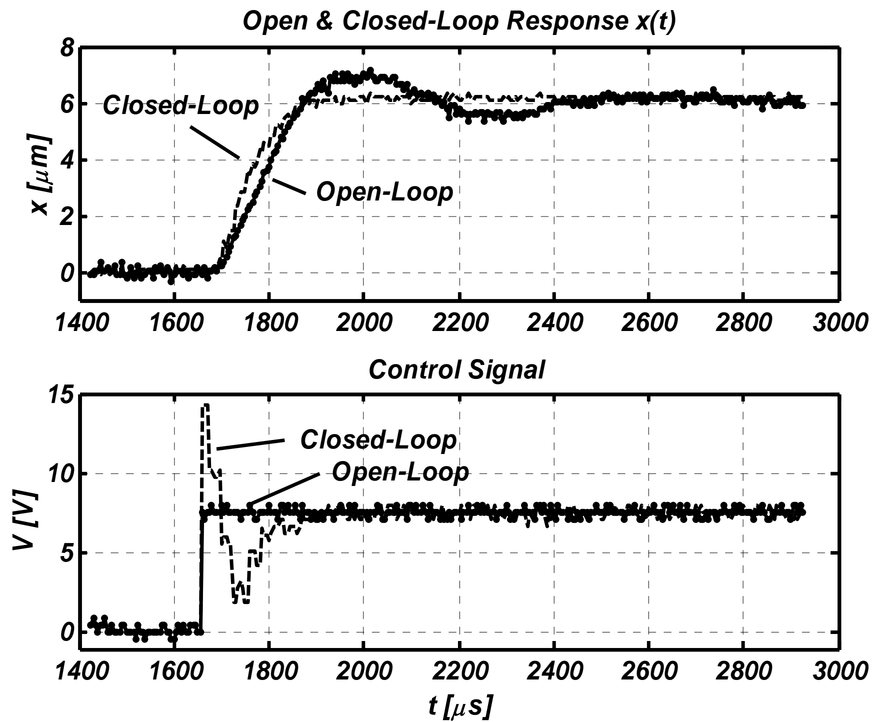

Figure 3.13 Open and Closed Loop Responses and voltage corresponding to closed loop response.

The rise time of the closed-loop system is around *170μs* which is faster than the rise time of the open-loop step response (*190μs*). However, it is slower than the rise time of the pre-shaped case (*100μs*). The rise time in the closed-loop case is limited by the minimum achievable sampling time (*12μs*). It is interesting to observe that there are

no visible residual oscillations present in the closed-loop response. Typically, closed-loop control dramatically reduces the system's sensitivity to vibrations [29].

3.5 Discussion: Comparison & Issues

Having accomplished the comparison between the pre-shaped open and closed-loop approaches, a meaningful discussion for choosing the driving approach can be presented. First, the discussion on how the purpose of the device affects the choice is discussed. Next, the comparison in terms of parameter's sensitivity is given. Finally, the small scale feedback and sensing problems are addressed.

3.5.1 Purpose of the device

The light modulating device presented in this paper can be used either as an optical switch (OS) or variable optical attenuator (VOA). OS mode requires switching the shutter position from fully closed to fully open and vice versa as quickly as possible, without an overshoot. As such, it does not require anything but a fast, aperiodic response. Therefore the pre-shaped open-loop approach can be employed. The results from figures 3.10 and 3.11 show that fast response ($100\mu s$) can be achieved with quite simple driving circuitry. The residual oscillations are not important if their amplitude is small enough, especially if it does not interfere with the light intensity.

On the other hand, the VOA is typically used to condition the optical signal intensity after laser diodes, before fiber-optic amplifiers and photo-detectors [23]. Therefore, in addition to fast, aperiodic response, the control of the light intensity requires an accurate positioning of the modulating shutter. In this case, the closed-loop control is a better approach.

3.5.2 Sensitivity of the parameters

The next step is to compare the driving approaches in terms of the system's parameter sensitivity. A series of simulations was conducted and the mass, damping, and stiffness were varied within $\pm 20\%$ of their nominal values. Simulated results of nominal values and the parameter variations are shown in figures 3.14, 3.15, and 3.16. The experimental data for nominal values is also included for reference. It is obvious that the closed-loop driving renders much less sensitivity to the parameter changes.

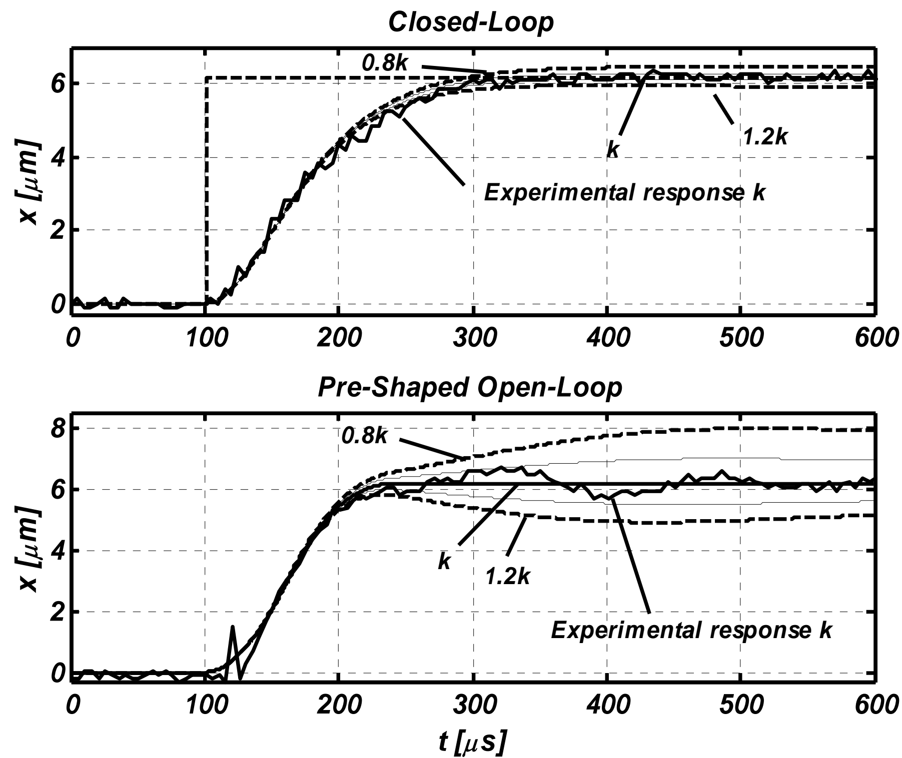

Figure 3.14 Sensitivity on change in stiffness, *k* represents the original stiffness of the device.

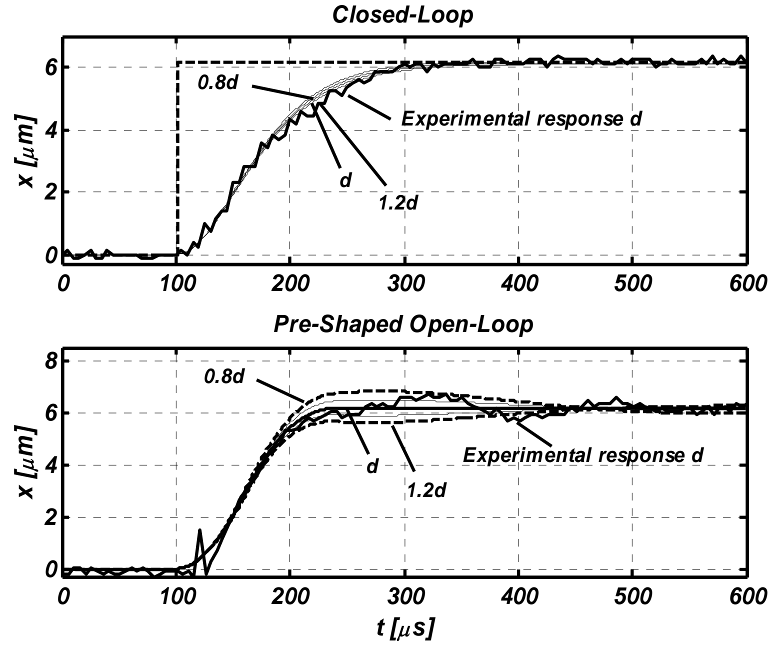

Figure 3.15 Sensitivity on change in damping, *d* represents the original damping of the device.

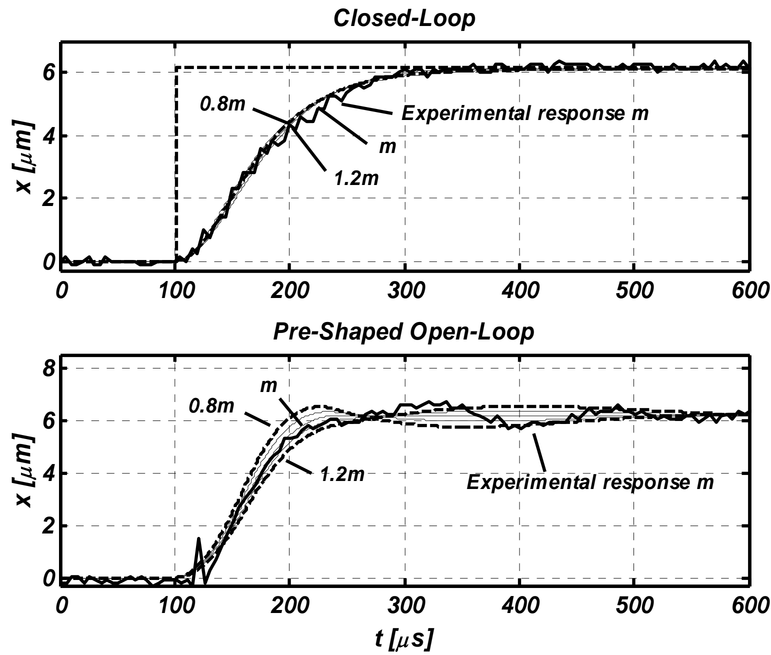

Figure 3.16 Sensitivity on change in mass; *m* represents the original mass of the device.

3.5.3 Problems - Small Scale Feedback

Contemporary macro-scale control systems are typically implemented with micro-controllers that execute a digital control algorithm. Sensors are relatively small in comparison to the controlled system and are quite easily implemented anywhere they need to be. Several factors make MEMS control systems unique. First, unlike macro systems, MEMS systems are small and typically very fast. Second, the implementation of the sensor on the device can significantly change the size and dynamics of the device. Third, the whole control system should be integrated with the MEMS device and therefore should be as small as possible.

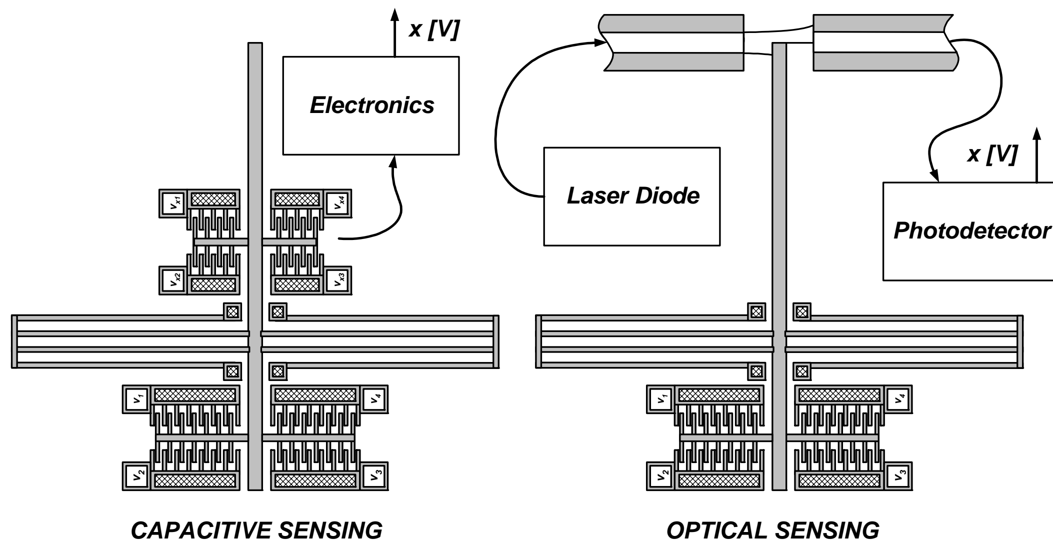

Figure 3.17 Difference between capacitive and optical sensing.

Response times of MEMS ranges from few ms for large DRIE fabricated thermal actuators to μs ranges for small surface electrostatic devices [12]. Conversion

times for the standard D/A and A/D converters range from *1-10μs*. This excludes the application of the microcontroller for devices faster than *100μs*. The use of a microcontroller becomes questionable not only because of conversion times, but because it is too large to be integrated with MEMS devices. Due to the implementation size, the control algorithm should be kept as simple as possible. Control algorithms can be implemented as digital filters with sequential stages of multiplication and accumulation [29], or they can be implemented using analog techniques [17].

Position sensing makes the control system even more complicated. There are several ways to sense position. For the MEMS device described in this paper we implemented optical sensing, which, as a sensing approach, has several problems. First, the relationship between the actual position of the device and the output optical intensity is nonlinear. Moreover, small fiber misalignments can cause relatively large errors in the sensor output. The shape of the optical cavity enclosing the sensing point (figure 3.6) can significantly influence the quality of the measurement (figure 3.7), especially if the cavity's dimensions are comparable to the wavelength (*1.5 μs*) of the light used. An unstable light source can also influence the measurement significantly.

Capacitive sensors are typically implemented as a differential capacitance [29]. As it is shown in the figure 3.17, the sensor becomes a part of the device. Electronic circuitry, converting the capacitance to a voltage and position, is attached to the sensor. A number of signal processing techniques have been developed [12],[26], [29]-[30] to extract the position from the measured capacitance. It is favorable to have as large of a capacitance as possible to get high resolution and high Signal-to-Noise Ratio (SNR)

[29]; however, the larger capacitor requires larger area which consequently increases the mass of the device slowing its response. Practically, however, the achievable values of microcapacitors are typically in the $fF - pF$ range, and therefore interfere with the value of the parasitic capacitance of the attached electronics (few pF) [29]. In order to mitigate the effects of these shunt capacitances it is desirable to integrate IC and MEMS devices together [29].

3.6 Conclusions

As a result of the analysis and experiments conducted for both open and closed-loop control of MEMS, some conclusions regarding the performance of different control approaches can be drawn.

In terms of the complexity for the driving and sensing electronics, an open-loop approach has advantages over closed-loop control as it uses only driving circuits. On the other hand, open-loop driving is sensitive to parameter uncertainties and the shape of the input signal. The input voltage spikes have to be timed very precisely. For studied device the accuracy of the triggering time is typically less than $0.1\mu s$. Faster responses and higher voltages require even higher precision. The closed-loop control approach is significantly less sensitive to changes in system parameters, and generates oscillation-free response [29].

In terms of application requirements, when a MEMS device is used for switching, only two signal levels are of interest and the best way to drive it is using pre-shaped open-loop signals. However, if the actuator has to be accurately positioned

between 0 and 100%, as in the case of VOA, it is more suitable to use a closed-loop approach.

In conclusion, the choice of the control systems for MEMS depends on the available sensor, the size, and the speed of the device. The most difficult aspect of implementation is related to the hardware necessary for control, rather than the control algorithms. Finally, the control algorithms should be kept as simple as possible so they can be integrated directly in hardware with IC and optical components.

CHAPTER 4

LIGHT-INTENSITY-FEEDBACK WAVEFORM GENERATOR BASED ON MEMS VARIABLE OPTICAL ATTENUATOR

4.1 Introduction

The introduction of fiber-optic networks into the communication industry has unleashed escalating demands on re-adaptation of many devices traditionally used for optical signal conditioning, especially in terms of device size, power consumption, mechanical reliability and cost. Variable optical attenuators (VOA) are among the variety of micro-electromechanical (MEMS) devices that have been developed during the last decade. The VOA are typically used to control optical signal intensity (power) between laser diodes and fiber-optic amplifiers and photo-detectors [3], [23], [87] and [31]. Several MEMS-VOA approaches have been developed, and an excellent overview is given in [23]. Typical architectures are a shutter (blade) insertion type, a rotating or sliding mirror type, and interferometry based types [46]-[48], [87], [70].

Advantages of the VOA in controlling light intensity are various. The direct tuning range of the laser source is typically less than *20dB*. In contrast, the tuning range of the MEMS VOA can go up to *40dB*, depending on the quality of the device. Another issue is the wavelength (frequency) dependency of the power of the light source, called chirping. Frequency shifting is unacceptable in optical communications, especially in dense wavelength division multiplexed (DWDM) systems. This problem does not exist

when MEMS VOAs are used. Laser sources also exhibits a large noise when used at low power levels, because a large part of the light comes from the spontaneous emission. This is unacceptable in optical communications. Additionally, MEMS-based VOAs combine a fast response time, precise attenuation control, long-term repeatability, and they are less expensive than the competetive products. MEMS VOAs are very flexible with respect to data rate or protocol, therefore eliminating the need for costly and lossy optical-electrical-optical conversion [74]-[75].

Due to its wavelength independency and excellent attenuation properties, the MEMS VOA, configured as a signal generator, can be used as a tool to simulate variable network losses and many scenarios of network events, such as adding/dropping of users, breakdowns in the network, etc. An excellent overview of the advantages of the controlled VOA is given in [32].

As a mechanically operated device, the MEMS VOA needs a MEMS actuator for movement. One of the most common types of MEMS actuators is an electrostatic comb drive actuator. The electrostatic comb drive actuator was introduced by Tang [22], and since then, it has been gradually modified and improved, finding more and more applications [33]-[37]. A milestone in the design of the MEMS actuators was the introduction of the Deep Reactive Ion Etching (DRIE) technology [24] which enabled the fabrication of high-aspect ratio MEMS structures, proving itself extremely suitable for the design of the comb drive actuators.

Simultaneously, increasing requirements for improved dynamical behavior has resulted in the gradual introduction of open-loop [2], [16], [17] and closed-loop [1], [20], [21], [18] control system techniques into the MEMS field.

In this chapter, the existing shutter-insertion type VOA, shown in figure 3.1 [3], is used as a platform for the design, implementation, and actual testing of a light intensity controller. Such feedback produces a very accurate VOA output signal that is independent of the reconstruction of the typically uncertain and complex relationship between position and light intensity. Although the idea of light intensity control emerges naturally and was introduced by [39], it is extremely interesting to extend controller capabilities to achieve fast, accurate, and well-shaped dynamical behavior. The purpose of the controller is two-pronged: to compensate for the disturbances in light intensity, typically generated by the light source, and to make possible the generation of complex light intensity time-waveforms. A hierarchical feedback controller is designed herein consisting of an outer, light intensity control loop and an inner, position control loop. The controller design is based on a simple but adequate mathematical model of the MEMS device as detailed in this paper. Light intensity is used as a sensing mechanism. The resulting feedback controller design is verified by experimental results and it is demonstrated that it dramatically improves the response of the MEMS VOA device. A physical description and some characteristics of the system used for implementation are given.

4.2 Device Description

An optical MEMS device from chapter 3 will be used as a platform to develop the light intensity controller, and it is shown in figure 3.1. The detailed geometry of the device is given in figure 3.2 [4] and in the section 3.2.

The experimental configuration is shown in figure 4.1. The voltages V_f and V_b are applied to the forward and backward actuators, causing them to move. The movement of the actuator modulates the light generated by laser diode, and the light is sensed by photo-detector. The voltage from photo-detector, V_{PD}, is processed to determine the deflection, x, and the light intensity, P.

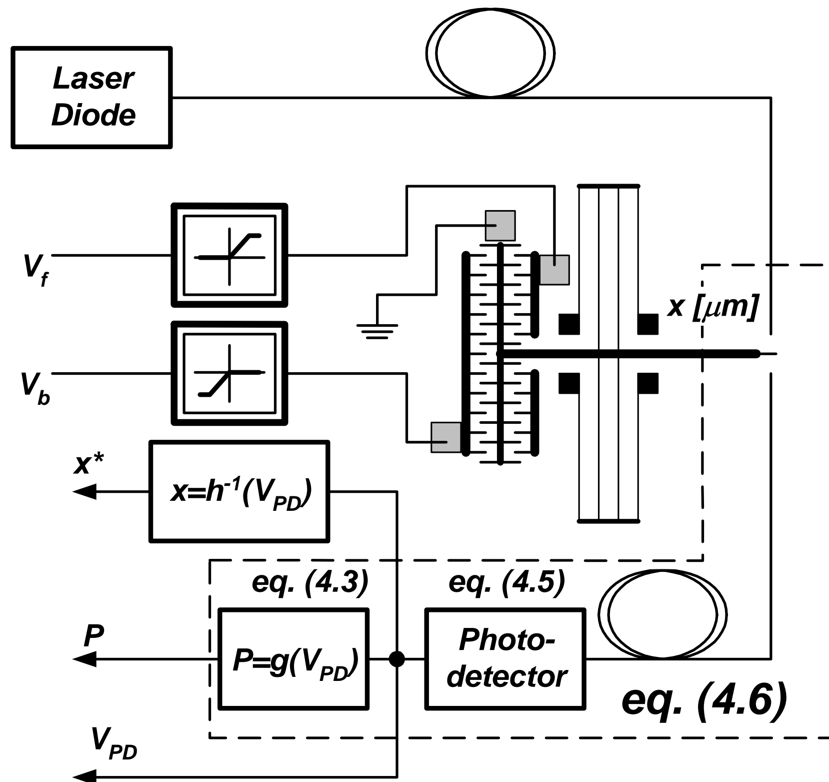

Figure 4.1 Experimental setup of the VOA.

4.3 Mathematical Model

Since the same device was used as in the chapter 3, only the optical part of the model is derived in detail. Mechanical and electrical models are the same, except that the direction of the *x*-axis is opposite that shown in figure 3.2. The forward and backward actuating voltages are switched, as well. The dynamical model of the system is then similar to eqs. (3.1) and (3.2)

$$m\ddot{x} + d\dot{x} + kx = f_f\left(V_f, x\right) - f_b\left(V_b, x\right) \tag{4.1}$$

$$P = h\left(x\right) \tag{4.2}$$

where P is a light intensity, and h is a sensing function relating position and photo-detector voltage. Other variables and parameters are defined in section 3.3.

4.3.1 Optical Sensing Model

The optical sensing model has a two-pronged purpose as shown in figure 4.1. First, it relates the intensity of light to the position of the shutter, and second, light itself is used as a feedback. The sensing mechanism is shown in figure 3.6. Notice again that the sensing model, developed in this chapter, assumes the opposite direction of the *x*-axis. The light beam is intercepted by the shutter, which modulates the throughput of the light. The light intensity is measured by a photo-detector. Light intensity is proportional to the photodetector voltage, V_{PD}, and it is given as

$$P = 2.08\, V_{PD} + 1.66 \tag{4.3}$$

Eq. (4.3) is valid over the photo-detector output voltage range $-0.8V \le V_{PD} \le 0V$. Light power in (4.3) is given in μW, and the voltage is in volts.

It is not simple to model the relationship between the shutter position and the intensity of the light beam. Several models can be used to address this effect [3], [19]. In this paper, the Rayleigh-Sommerfeld [3] model is used. It is based on a Gaussian distribution of the intensity across the light beam as shown in figure 3.6.

The waist of the Gaussian beam coming from the fiber is denoted by w_0. As the beam propagates in free space, the waist increases and has a value of w_1 at the point where it intersects the shutter. With the shutter in the middle of the beam at the rest position (see figure 3.6), the relationship between light intensity and deflection is given as [19]

$$P(x) = 1.58\left\{0.5\left[1 - erf\left(-\sqrt{2}\frac{x}{w_1}\right)\right] + 0.5\right\}[\mu W] \tag{4.4}$$

where w_1 is $7\mu m$.

With the inverse of (4.3) taken into account, $V_{PD}(x)$, can be analytically determined from (4.4), and it is shown in figure 4.2. The experimental results are also shown in figure 4.2. An unexpected discrepancy between the analytical model and the experimental data is obvious for positive deflections of x. The reason for this phenomenon most likely comes from the size and shape of the optical cavity (figure 3.6.) which could cause uncontrolled reflections or unwanted diffraction effects (i.e.,when the dimensions of the optical cavity are on the order of magnitude of the wavelength of the light $1.55\mu m$). Our feedback controller guarantees that the position $x(t)$ remains inside the attenuation range of the VOA so that the inverse of the curve-fitted model (4.6) can be used as position feedback.

The experimental data in figure 4.2. can be curve-fitted using a *4-th* order polynomial inside the deflection range $-6.5\mu m \le x \le 0$ by

$$V_{PD} = h^*(x) = a_3x^3 + a_2x^2 + a_1x + a_0 \tag{4.5}$$

with the following parameters: $a_3 = -0.0023V\mu m^{-3}$ $a_2 = -0.038V\mu m^{-2}$, $a_1 = -0.23V\mu m^{-1}$ and $a_0 = -0.54V$. In order to determine sensing nonlinearity, (4.2), (4.3) and (4.5) should be combined, yielding

$$P = h(x) = c_3x^3 + c_2x^2 + c_1x + c_0 \tag{4.6}$$

with $c_3 = -4.8\times10^{-3}\ \mu W\mu m^{-3}$, $c_2 = -7.97\times10^{-2}\ \mu W\mu m^{-2}$, $c_1 = -0.47\ \mu W\mu m^{-1}$, and $c_0 = 0.53\ \mu W$.

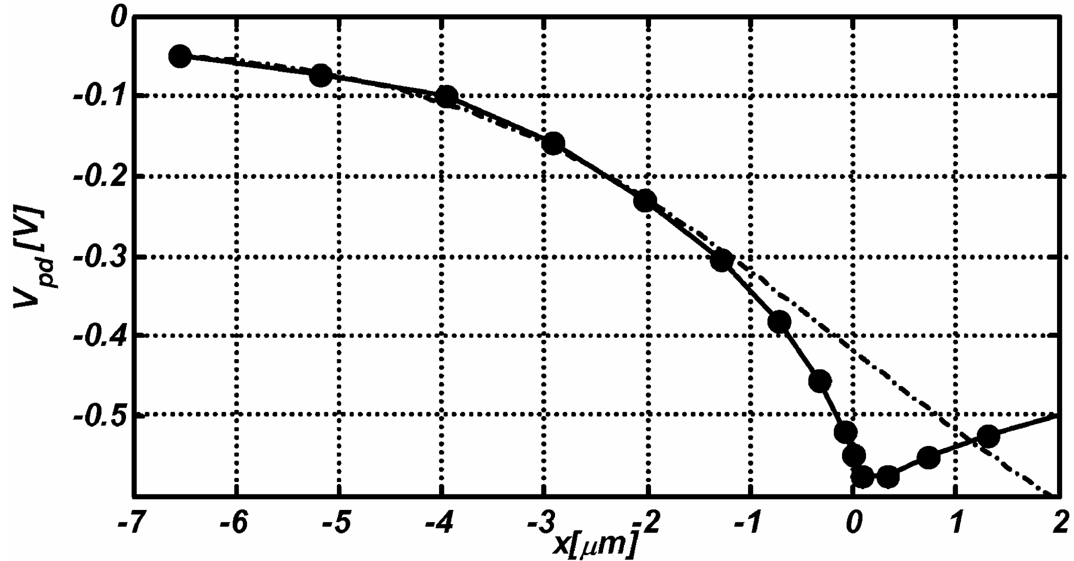

Figure 4.2 Theoretical (4.4) (dashed), and experimental (dotted full line) relationship between V_{PD} and x.

In order to reconstruct x from V_{PD} it is necessary to find the inverse of (4.5). The inverse of (4.5) was reconstructed as a set of affine functions, (i.e., as a lookup table), for the purpose of the controller design (see figure 4.1).

4.3.2 The Complete Model

The model in (4.1) and (4.2) can be populated by parameters determined from (4.3), (4.4), (4.7) and (4.6), and the damping coefficient that was determined experimentally. Summarized, the model is given as

$$7.75\times10^{-9}\,\ddot{x}+8\times10^{-5}\,\dot{x}+1.05x=8.2\times10^{-8}\left(V_f^2-V_b^2\right) \tag{4.7}$$

$$P=-4.8\times10^{15}x^3-7.97\times10^{10}x^2-4.7\times10^5x+0.53 \tag{4.8}$$

Note that the deflection x in (4.7) and (4.8) is expressed in meters, and that (4.6) is scaled from microns to meters yielding (4.8).

4.4 Controller Design

The controller consists of an inner, position control loop and an outer, light intensity control loop (see figures 4.1 and 4.4). The position controller is of a Proportional-Derivative (PD) type with a feed-forward gain. The purpose of the position feedback is to speed up the system, linearize it, and simplify the design of the outer loop. The position feedback x^* is reconstructed from figure 4.2.

The light intensity controller is of Proportional-Integrate-Derivative (PID) type with photo-detector voltage feedback that is linearly related to light intensity through (4.3). The purpose of the outer control loop is to achieve accuracy tracking of the desired light intensity profiles. Direct light intensity feedback ensures that accuracy of

the output waveform does not rely strongly on the light-intensity to position relationship (4.4) and (4.6), which is typically problematic.

4.4.1 Position Control Loop

The control voltage is given in terms of the control signal defined as the contribution of the feed-forward and feedback part as

$$u = u_{ff} + u_{fb} = V^2 = (V_f + V_b)^2 \qquad V_f \geq 0, \quad V_b \leq 0 \tag{4.9}$$

Note that $V_f \neq 0 \Rightarrow V_b = 0$, and vice versa. Merging (4.1), (4.5) and (4.9) yields

$$\frac{m}{k}\ddot{x} + \frac{d}{k}\dot{x} + x = (k_e/k)(u_{ff} + u_{fb}) \tag{4.10}$$

with $\sqrt{u_{ff} + u_{fb}} = V_f + V_b$. A square root is used to compensate the quadratic term in the input to the system (4.7), thereby linearizing the input nonlinearity.

The fact that the open-loop system (4.7) and (4.8) is stable enables the direct use of the feed-forward gain, bringing the position close to the desired one. The feed-forward gain of the system is determined by eliminating the velocity $\dot{x}$, acceleration $\ddot{x}$, and the feedback part of the control signal, u_{fb}, from (4.10), reducing it to

$$x_{ss} = \frac{k_e}{k} u_{ff} \tag{4.11}$$

If the steady-state deflection (4.11) is to be equal to the desired one, the feed-forward portion of the control signal is given as

$$u_{ff} = \frac{k}{k_e} x_d \tag{4.12}$$

yielding $x_{ss}=x_d$.

Next, the PD controller is introduced to speed up the system, mitigate the control error left behind by the feed-forward loop, and achieve a nearly aperiodic response. The differential equation describing the controller is given as

$$u_{fb} = K_P\left(x_d - x^*\right) + K_D\left(\dot{x}_d - \dot{x}^*\right) \tag{4.13}$$

Substituting (4.13) into (4.10), neglecting feed-forward gain, and assuming perfect position reconstruction; i.e., $x^* = x$, yield the closed-loop dynamics

$$\frac{m}{k}\ddot{x} + \left[\frac{d}{k} + \frac{k_e}{k}K_D\right]\dot{x} + \left[1 + \frac{k_e}{k}K_P\right]x = K_D\frac{k_e}{k}\dot{x}_d + K_P\frac{k_e}{k}x_d \tag{4.14}$$

Since a pure derivative cannot be implemented, the additional fast pole is added to the controller to make its transfer function causal [44]. Equation (4.13) becomes

$$u_{fb} + \left(\frac{K_D}{K_P N}\right)\dot{u}_{fb} = K_P\left(x_d - x^*\right) + \frac{K_D(N+1)}{N}\left(\dot{x}_d - \dot{x}^*\right) \tag{4.15}$$

with $N=5$. The controller parameters K_D and K_P were determined through the root locus method, considering the limited voltage available for the control effort. The controller parameters are $K_D = 1.12\times10^3$ and $K_P = 2.1\times10^7$.

The total control effort is summarized by collecting (4.9), (4.12), (4.15), the inverse of (4.5), and the limited available control voltage as

$$u = u_{ff} + u_{fb}, \quad u_{ff} = \frac{k}{k_e}x_d$$

$$u_{fb} + \left(\frac{K_D}{K_P N}\right)\dot{u}_{fb} = K_P\left(x_d - x^*\right) + \frac{K_D(N+1)}{N}\left(\dot{x}_d - \dot{x}^*\right) \;\; V_f = 2.3\sqrt{u}\,, \;\; u \geq 0\,, \tag{4.16}$$

$$V_f \leq 14V\,,\;\; V_b = -2.3\sqrt{-u}\,,\;\; u < 0\,,\;\; V_b \geq -14V$$

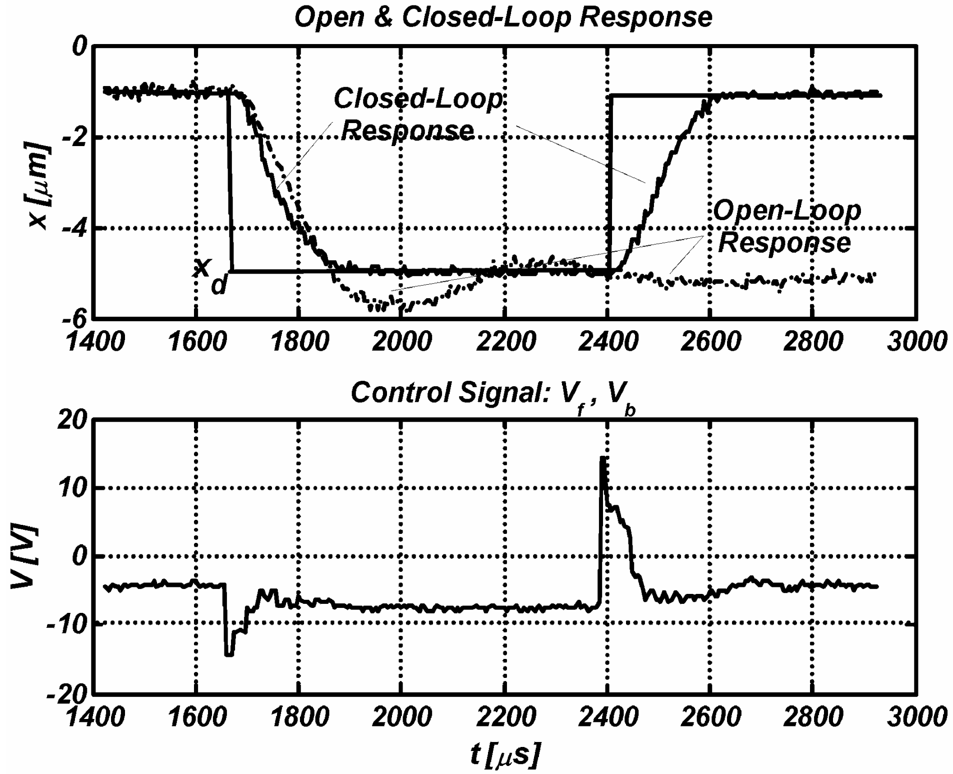

Figure 4.3 Desired value (x_d) and closed-loop response of the inner position loop (top). Open loop position for single transition (*0* to *-5μm*) is given for comparison. Control voltages V_b and V_f are given in the bottom part.

A transformation from the differential equations (4.16) to difference equations is obtained by substituting the derivatives of the signals $u_{fb}(t)$ and $x^*(t)$ with their approximate derivatives using the forward difference (1st Euler method). The approximate derivative of the of the generic signal, $\varphi(t)$, is given in [44] as

$$\dot{\varphi}(t) \approx \frac{\varphi(t+h_s)-\varphi(t)}{h_s} \qquad (4.17)$$

where h_s is the sampling time.

The experimental responses to the step input signal are shown in figure 4.3. It is interesting to observe that the dynamic voltages applied to the switch are far higher than the maximal pull-in static voltage (*8.96V*). Actually, the voltages up to *30V* were applied to this device in dynamic working conditions. This is exactly the reason why the controller is able to speed up the system.

4.4.2 Light Intensity Control Loop

From the results shown in figure 4.3., the position-control closed-loop can be approximated as a first-order differential equation

$$\dot{x} = \frac{1}{T_{pos}}\left(K_{pos}x_d - x^*\right) \tag{4.18}$$

with unity gain and the time constant being approximately $T_{pos} \approx 80\mu s$. The output of the system is a light intensity (4.5)

To satisfy the closed loop requirements, the PID controller is chosen

$$x_d = K_{LP}e + K_{LD}\frac{de}{dt} + K_{LI}\int^t e(\tau)d\tau \tag{4.19}$$

with a light intensity error signal, $e=V_{PDd} - V_{PD}$. The initial controller parameters are determined through the root locus method. The iterative experimental approach was then implemented, keeping in mind that nonlinear feedback (4.5) gives the best and final values of the parameters of the controller. They were found to be $K_{LP} = 0.475$, $K_{LD} = 17.6\times10^{-6}s$ and $K_{LI} = 17.2\times10^{3}s^{-1}$.

Regarding implementation, the total control action should be limited to the applicable feedback interval, V_{PD}. From figure 4.2. it can be seen that its values lay inside the *-0.05* and *-0.55V* interval, corresponding to *P=1.55* and $0.51\mu W$. The derivative gain should be limited in similar way (4.15) since it was done for the position controller. A discretization method used to transform the continuous controller (4.19) into a discrete one was the forward difference technique (4.17).

Finally, it is often useful to introduce the model of the desired system behavior in the command signal path (i.e., V_{PDref}) of the servo system [44]. The model, or pre-filter, helps ensure that the system is not driven too hard in response to a command signal. The chosen dynamic behavior of the model was determined by conducting computer simulations, and it is given in a standard transfer function form [44] as

$$\frac{V_{PDd}(s)}{V_{PDdref}(s)} = \frac{b_2 s^2 + b_1 s + b_0}{a_2 s^2 + a_1 s + a_0} \tag{4.20}$$

with $a_0 = b_0 = 17.2 \times 10^3$, $b_1 = 0.475$, $a_1 = 1.475$, $b_2 = 1.7 \times 10^{-5}$ and $a_2 = 9.7 \times 10^{-5}$.

The total light intensity servo controller action can be summarized by collecting (4.19), (4.20), and considering a limited control signal, x_d, as

$$\begin{gathered} \frac{V_{PDd}(s)}{V_{PDdref}(s)} = \frac{b_2 s^2 + b_1 s + b_0}{a_2 s^2 + a_1 s + a_0} \\ e = V_{PDd} - V_{PD} \\ x_d = K_{LP} e + K_{LD} \frac{de}{dt} + K_{LI} \int^t e(\tau) d\tau \\ -6.5\mu m \le x_d \le 0\mu m \end{gathered} \tag{4.21}$$

The complete controller (4.16) and (4.21) is shown in figure 4.4.

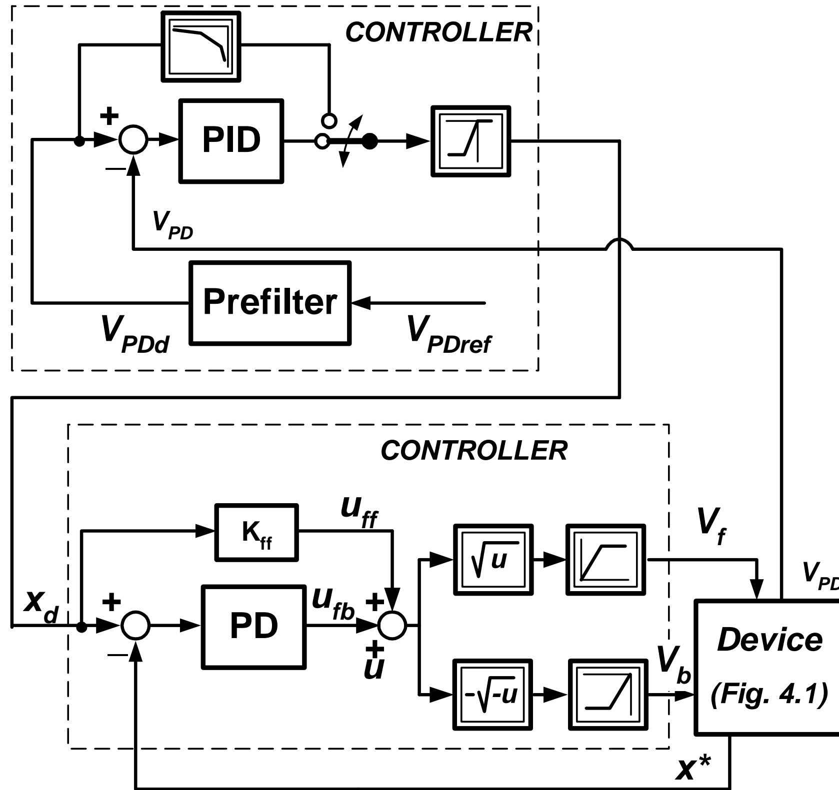

Figure 4.4 Block scheme of the controller.

4.5 Experimental Results

The light intensity control system was implemented using the fast *dSpace 1104* control development kit. Sampling time was $12\mu s$. The A/D conversion time was $2\mu s$, and the D/A conversion time was $10\mu s$. Algorithm processing time was negligible compared to the conversion times. The light intensity of the light source was adjusted such that the maximal light intensity (i.e., $1.55\mu W$) corresponds to the maximal allowable opening of the VOA (i.e., $-6.5\mu m$). The experimental analysis was done for

two cases - with and without the light intensity controller (see switch shown in figure 4.4). The inner position controller was active in both cases. Various desired light intensity waveforms were applied to the system in order to characterize it. The resulting light intensity waveforms were recorded. The results are presented in terms of the light intensity, P, rather than photo-detector voltage, V_{PD}, which was used as the actual feedback (see eq.(4.3)).

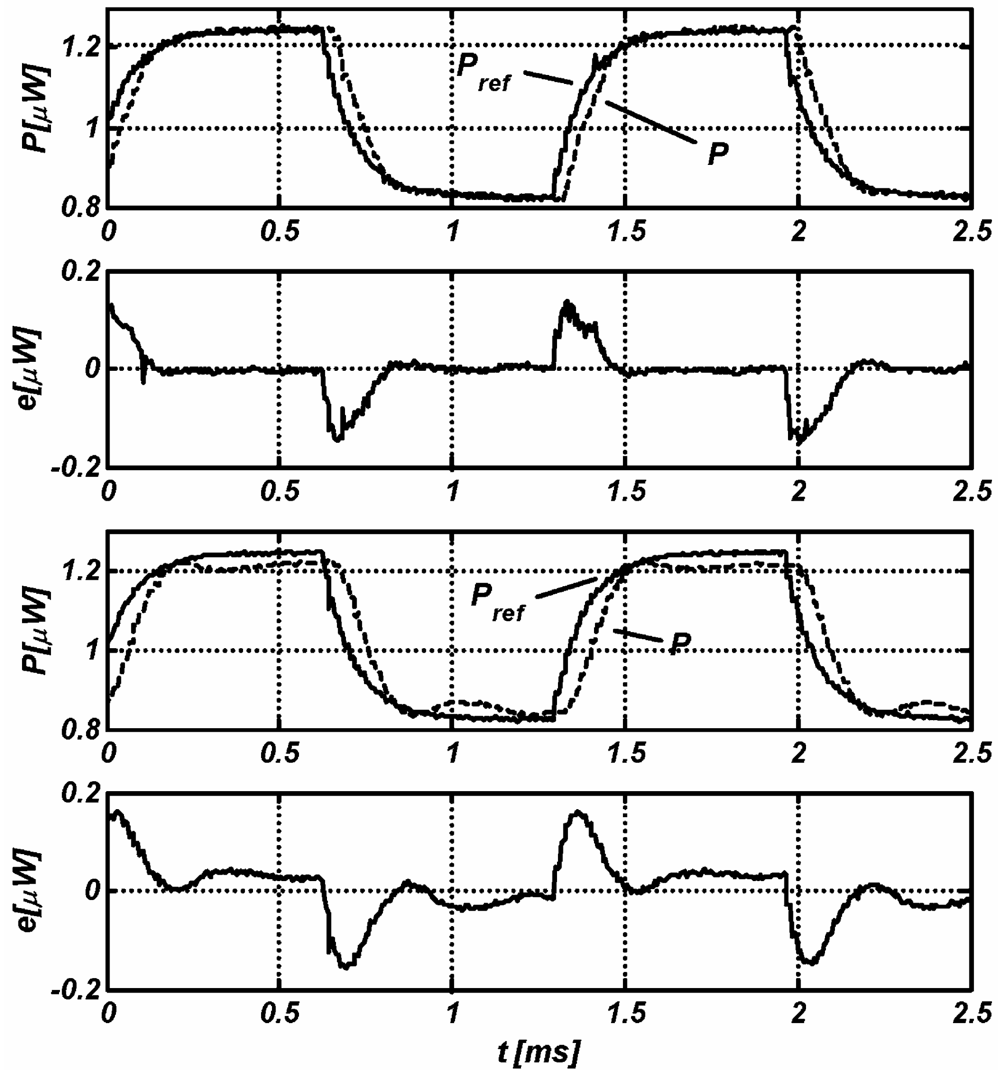

Figure 4.5 Desired and actual light intensity for square-wave like signal.

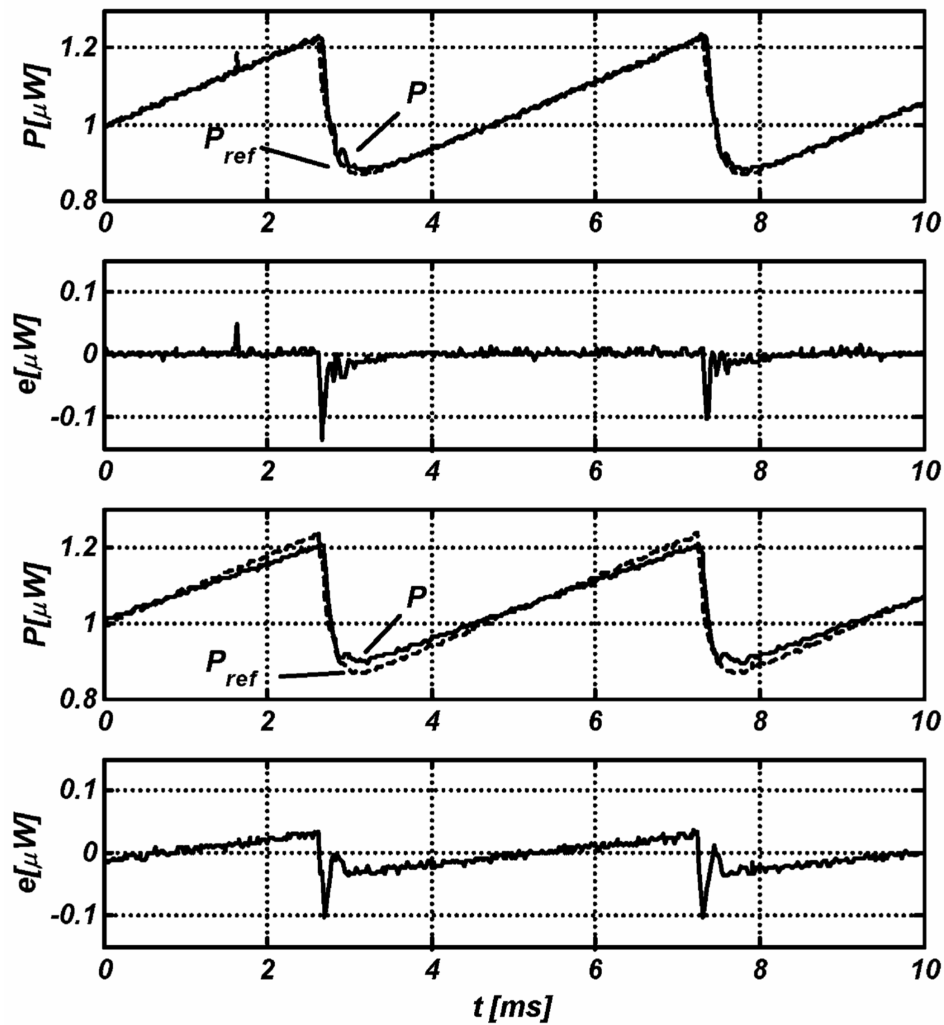

Figure 4.6 Desired and actual light intensity for saw-wave like signal.

The response of the system to the square-wave like signal was applied as a desired signal. The period of the signal was *1.4ms* and the desired light intensity varied between $0.82\mu W$ and $1.25\mu W$. The desired and actual signals for the controlled case are shown in the upper part of figure 4.5, and the corresponding tracking error is shown below it. The uncontrolled signals and the tracking error are shown in the bottom half of

figure 4.5. The steady-state error is *10%* in the uncontrolled case, and *0%* in controlled case. The minimum achievable rise time (*0-90%*) was less than *200μs*. Moreover, if the results from the top of figure 4.5 are compared to the directly-driven open-loop dynamic response of the VOA shown in figure 4.3., when both the position and light intensity

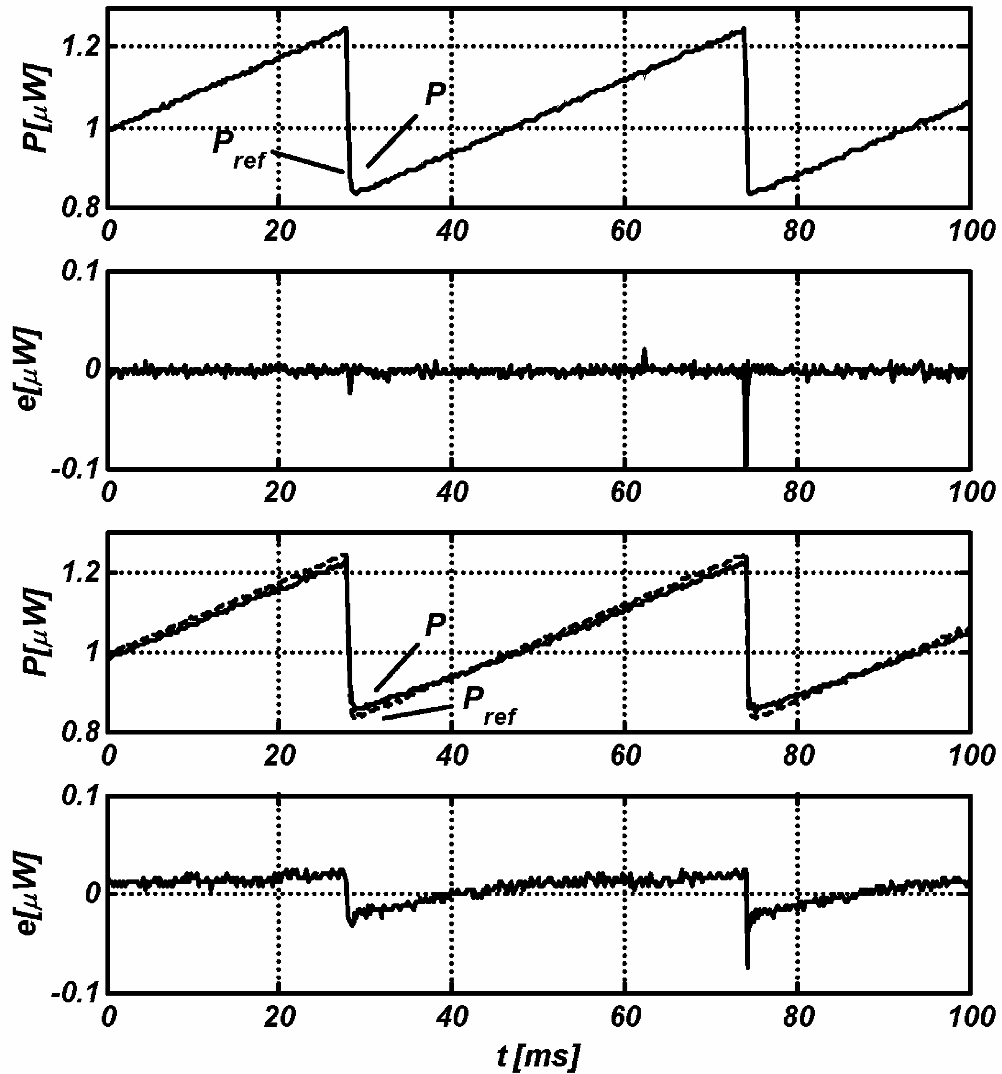

Figure 4.7 Desired and actual light intensity for saw-wave like signal of lower frequency.

controllers are turned off. The improvements are obvious. The rise time is similar, but there is no overshoot, and the settling time is *30%* of the open loop settling time.

The next example illustrates the response of the system to the saw-like referent signal with a period of *4.2ms*. The desired light intensity varies between $0.88\mu W$ and $1.22\mu W$. The results are shown in figure 4.6. When the optical intensity controller is switched on, the tracking error is dramatically reduced. The trajectory following is almost perfect, except during fast transitions.

Next, the frequency of the saw-like signal was decreased by a factor of approximately *10*. The period of this signal was *45ms*. The desired signal alternates between $0.85\mu W$ and $1.22\mu W$. The results are shown in figure 4.7. When the optical intensity controller is switched off, the average error is within *8%* of the input light intensity range. When it is turned on, the tracking is practically perfect.

4.6 Device Properties

The concept for implementing the optical waveform generator is shown in figure 4.8. The light coming from the light source is modulated by the MEMS VOA. The VOA is controlled using a microcontroller. Feedback, in terms of light intensity, is provided by the photo-detector attached to the optical-coupler. The interface electronics provide adjustments of signals being exchanged between the microcontroller, photo-detector, and VOA. The waveform generator can be integrated as a multichip package, containing the MEMS chip, microcontroller, interface electronics, and optical connection.

This light intensity waveform generator can be used to generate relatively accurate, time-dependent signals with zero third and higher order derivatives. It is an excellent tool to simulate variable network losses and many scenarios of network events, such as the adding/dropping of users, breakdowns in the network, etc.

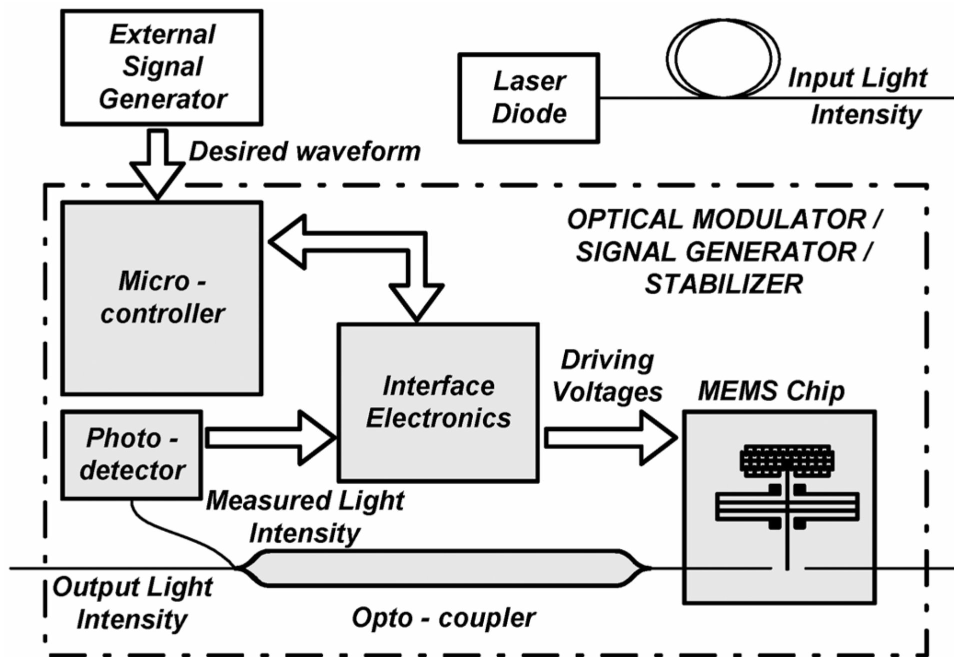

Figure 4.8 Light intensity waveform generator.

For the purpose of system performance analysis, the waveform generator, with its aperiodic response (figure 4.5), can be seen as the first-order dynamic system with unity gain and a dominant time constant. The dominant time constant is $143\mu s$, and it is defined as the time required for the response to reach *2/3* of its steady-state value. This corresponds to frequency band with a cutoff frequency $\omega=6950rad/s$ or $f=1.1kHz$. The rise time is $T_{0-90\%} < 200\mu s$. These results are superior to the results obtained with direct

open-loop driving (figure 4.3), which shows an oscillatory response with a comparable rise time, but large settling time $>500\mu s$.

The output light intensity range of the waveform generator is determined by the original range of the VOA, with the exception of the power taken away by the optical coupler as feedback.

Accuracy of the output light intensity depends primarily on the photodetector's accuracy. The more accurate that the light intensity measurement is, the more accurate that the output of the generator will be. If light intensity measurement is assumed perfect, the attenuation error in the steady-state condition is zero, as shown in figures 4.5 - 4.7.

The waveform generator is linear inside the achievable attenuation range; i.e., the light intensity controller ensures that there is no steady-state error between the desired and the actual light intensity, therefore, making the static input-output relationship linear.

4.7 Conclusions

Increasing demands on the dynamical behavior of MEMS devices are reaching a point where mechanical design by itself cannot provide further improvements. Alternative approaches, based on control theory, such as open-loop or closed-loop driving strategies, need to be considered to provide further performance enhancements. In this research, an experimental setup and a practical system characterization of the light intensity control system for an optical waveform generator are discussed. The feedback control system is implemented on an actual MEMS VOA. The results verify

that the control system proposed in this research do significantly improve the dynamical behavior of the existing device. It can be assumed that the implementation of the light intensity feedback may improve the accuracy of any VOA. Direct light feedback solves the problem of the usually complex and uncertain relationship between position and light intensity. The price to be paid is implementing the feedback itself.

As it is, the light intensity controller used in this paper is not perfect. First, there exists a non-unique reconstruction of the position caused by geometry of the modulating cavity. This requires reshaping the modulating cavity in order to improve the sensing range, and it is actually not a controller, but a VOA design problem. The second problem is the use of the linear single input double output (SIDO) controller for the nonlinear problem. An improved SISO nonlinear tracking controller based only on light intensity feedback enables a wider application range of the device [50]. Additionally, instead of digital implementation, the controller should be replaced by an analog version, i.e., by operational amplifiers. The reason for this lays in the settling time of the standard D/A converters ($2\text{-}10\mu s$), which becomes significant compared to the MEMS dynamics.

The MEMS VOA, with its excellent light modulation properties combined with the accuracy provided by controller, however, represents a flexible and useful tool in the analysis and testing of various optical networks.

CHAPTER 5

LATERAL INSTABILITY PROBLEM IN ELECTROSTATIC COMB DRIVE ACTUATORS: MODELING & FEEDBACK CONTROL

5.1 Introduction

Electrostatic actuators have an important role in MEMS technology. Compared with the other types of micro actuators [1], [15], electrostatic actuators generate relatively modest force (several μN), but they consume virtually no electrical power [23]. One of the most common electrostatic actuators is the comb drive, which exhibits an interesting and useful property in that the generated force does not depend on actuator position (deflection), but only on the square of the applied voltage. The actuator mathematical model, developed in a one degree-of-freedom (DOF) context, is relatively simple [3], [19], and operating the actuator is quite straightforward.

The main issue of the comb drive design is achieving large deflections while minimizing the actuation voltage, resulting in a small deflection-to-size ratio of the actuator. These requirements are typically satisfied by balancing the design of actuator's suspension and varying the size of the force-generating comb structure. The comb drives, however, inherently suffer from a electromechanical instability called lateral or side pull-in, or lateral instability [40], [53], [64]-[65]. Although fabricated to be perfectly symmetrical, the actuator's comb structure is always unbalanced, causing the neighboring electrodes to contact each other when the voltage-deflection conditions are

favorable. Weak suspensions and large forces, designed to achieve large traveling ranges, increase this problem even more. An example of the comb fingers in the state of lateral instability is shown in figure. 5.1.

The lateral instability occurs when the electrostatic stiffness transverse to the axial direction of motion exceeds the transverse mechanical stiffness of the suspension [40], [41]. Therefore, the most common way to avoid it is by increasing the transverse stiffness of the suspension [1], [14], [42], [82]. Unfortunately, all of the suspension-stiffening approaches, eventually, limit travel range of the actuator.

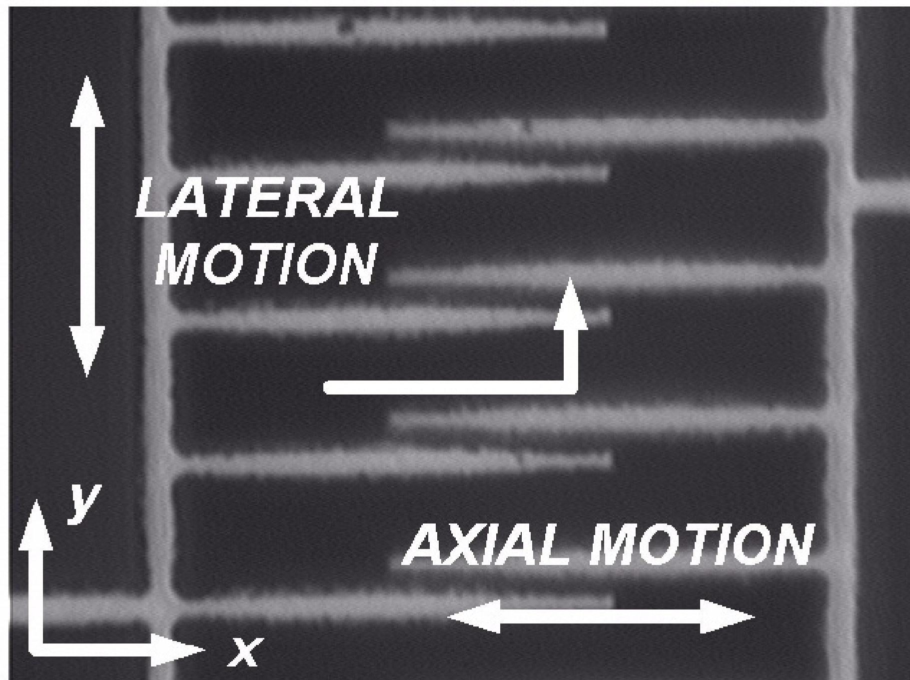

Figure 5.1 Electrostatic comb drive actuator in the state of lateral instability.

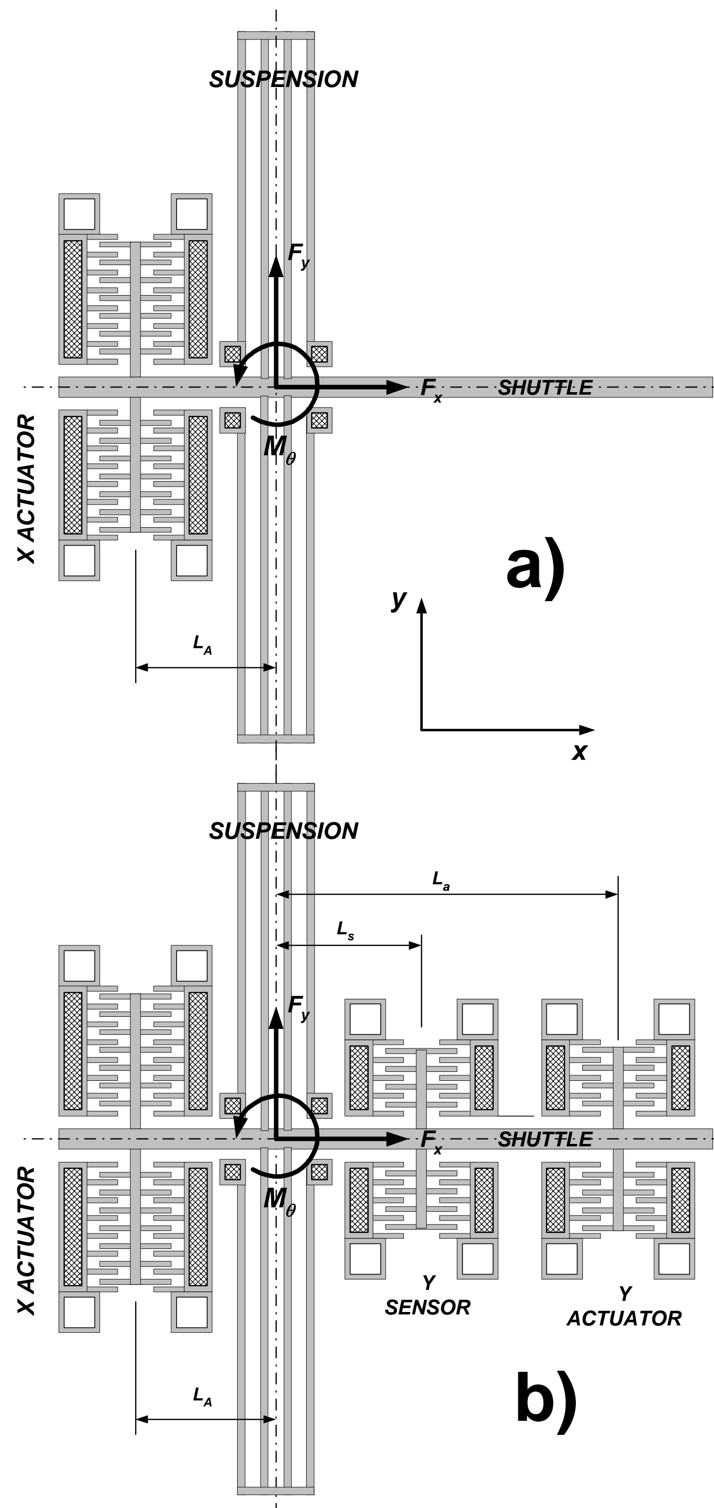

Figure 5.2 The original electrostatic comb drive actuator [43] (top), and the hypothetical device for lateral DOF feedback control (bottom).

A novel approach that relies on the use of feedback control to counteract the lateral instability will be investigated. A requirement for doing so is to have a lateral motion sensing capability and an appropriate model of the device for the subsequent control system design. The introduction of the lateral feedback may impact the design of the comb drive, mitigating the requirements on the suspension, lowering the actuation voltage, and, therefore, decreasing the ratio between the size of the actuator and achievable deflection. To do this, a suitable model for lateral stability analysis will be determined, and then an appropriate control system will be designed.

In section 5.2, the existing comb drive, fabricated using deep reactive ion etching (DRIE), with a well-developed, experimentally verified mathematical model in one degree of freedom (DOF) [43], is extended to include the asymmetrical lateral DOF. The device is shown in figure 5.2a. The parameters of the lateral DOF model are determined through the combined finite element analysis (FEA) and static experimental results in section 5.3. In section 5.4, following the model verification, the structure of the device is extended with both sensor and actuator functionality for lateral movement, as shown in figure 5.2b. These additional features enable the design of the controller for lateral motion, described in section 5.5. A discussion of the implementation issues concludes this chapter.

5.2 Mathematical Model

The mathematical model presented in this section is done for the actual actuator shown in figures 5.1. and 5.2a. First, the modal FEA is conducted to determine the modes of the device that participate in the motion so as to actually define the structure

of the mechanical model. This exercise is followed by derivation of the electrostatic forces.

5.2.1 Structure of the Mechanical Model

The flexible comb drive is a Lagrangian system and, as a flexible structure, can be generally modeled as an infinite set of second-order differential equations [51], [80]. For practical purposes, however, it is necessary to include only the first few significant modes in the model, making it finite dimensional. The dynamic model of such a structure is generally written as

$$\mathbf{M}\ddot{\mathbf{x}} + \mathbf{D}\dot{\mathbf{x}} + \mathbf{K}\mathbf{x} = \mathbf{F} \tag{5.1}$$

where **M** is the inertia matrix, **D** is the damping matrix, **K** is the stiffness matrix, and **F** contains external forces acting on the system.

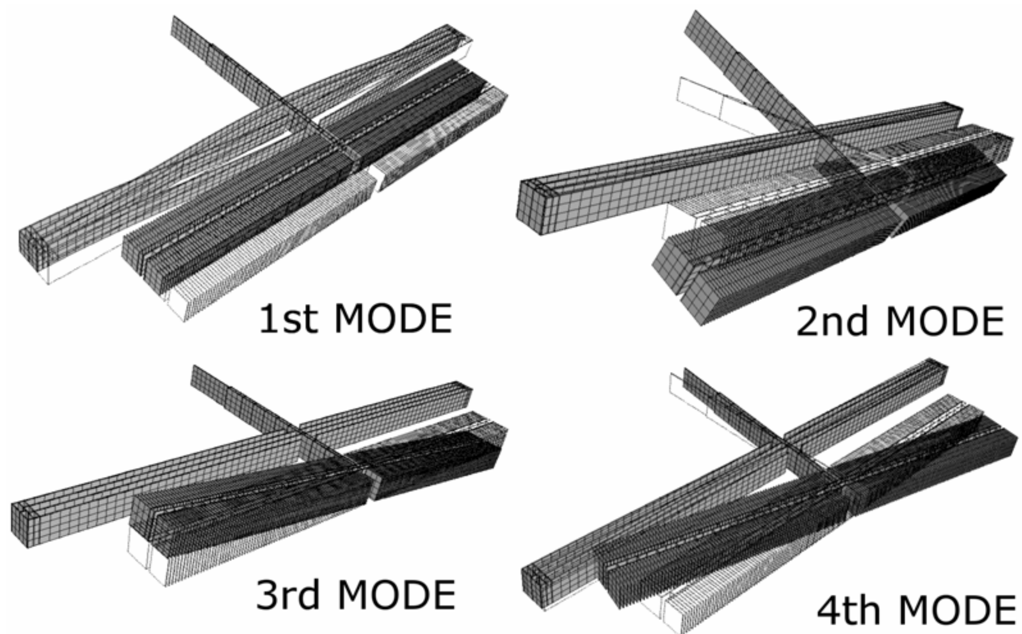

Figure 5.3 The first four modes of the actuator.

In order to determine the parameters **M** and **K** of the model (3.1), a static and modal FEA were conducted. The FEA results can be used to populate the **M** and **K** matrices with the parameters. Mode values and the corresponding parameters are shown in Table 5.1. Mode shapes are shown in figure 5.3.

Table 5.1 FEA computed values for the modal frequencies, effective masses, and stiffness parameters.

Mode (i)	Value	m_{ii}	k_{ii}	
1	*1692Hz*	*7.75x10e-8 kg*	*1.08 N/m*	Along *x*
2	*3744 Hz*	*3.85e-16 kgm2*	*2.13e-7 Nm/rad*	Around *y*
3	*5427 Hz*	*1.39e-15 kgm2*	*1.62e-6 Nm/rad*	Comb around *x*
4	*6812 Hz*	*1.88e-15 kgm2*	*3.45e-6 Nm/rad*	Around *z*

The FEA was also used to observe the cross sectional elements of the inertia matrix **M**. They are negligible when compared to the main inertial elements. Therefore, it can be assumed that matrices **M** and **K** are diagonal with zeros out of diagonal. We can also neglect the contributions of the higher-order modes (*>4th*).

5.2.2 General Model: Assumptions and Structure

To begin, it will be assumed that the second- and the third-modes do not participate in the motion along the *x*-axis nor around the *z*-axis. For the purpose of developing the simple model, we need a two degree-of-freedom (DOF) model, containing the first and the fourth modes. Additional modes can, however, influence the motion of interest, and this issue will be discussed later.

With only two DOFs left, the mathematical model [1] is reduced to

$$m_x\ddot{x} + d_x\dot{x} + k_x x = F_x \tag{5.2}$$

$$J_z\ddot{\theta} + d_\theta\dot{\theta} + k_\theta\theta = M_z \tag{5.3}$$

where m_x and J_z are the effective moving mass along the x-axis, and the effective moment of inertia around the z-axes, respectively. Notations d_x and d_θ describe damping, and k_x and k_θ are the stiffnesses along the x-axis and around the z-axis, respectively.

Since lateral movements are small; i.e., $y << L_A$, we can approximate $tg\theta = y/L_A \approx \theta$, modifying (5.3) as

$$\frac{J_z}{L_A}\ddot{y} + \frac{d_\theta}{L_A}\dot{y} + \frac{k_\theta}{L_A}y = -F_Y L_A \tag{5.4}$$

and, after dividing (5.4) by L_A

$$\frac{J_z}{L_A^2}\ddot{y} + \frac{d_\theta}{L_A^2}\dot{y} + \frac{k_\theta}{L_A^2}y = -F_Y \tag{5.5}$$

Eqs. (5.1) and (5.5) represent the dynamics of the comb drive actuator in a two DOF context.

5.2.3 Electrostatic Model: Actuator and Lateral Instability

The structure of the comb drive actuator is shown in figure 5.4. The virtually symmetrical comb drive actuator is made laterally unbalanced by introducing Δd. The models for force-generation in x- and y-directions need to be determined.

The capacitances C_F and C_B as a function of the variables x and y is given as

$$C_F(x,y) = N\varepsilon_0 T(x + x_0)\left(\frac{1}{d - \Delta d - y} + \frac{1}{d + \Delta d + y}\right) \tag{5.6}$$

$$C_B(x,y) = N\varepsilon_0 T(-x + x_0)\left(\frac{1}{d - \Delta d - y} + \frac{1}{d + \Delta d + y}\right) \tag{5.7}$$

where C_F and C_B are the forward- and backward-actuating capacitances, N is the number of finger electrodes of the each comb drive, ε_0 is the permittivity of the vacuum, T is the thickness of the structure, and x_0 is the initial overlapping between the fingers.

The force in x direction, F_x, is given as [12],[26]

$$F_x = \frac{1}{2}\frac{\partial C_F}{\partial x}V_F^2 + \frac{1}{2}\frac{\partial C_F}{\partial x}V_B^2 \tag{5.8}$$

where V_F and V_B are the forward- and backward-driving voltages.

Introducing (5.6) and (5.7) into (5.8), the resulting force in x-direction is given as

$$F_x = \frac{1}{2}N\varepsilon_0 T\left(\frac{1}{d - \Delta d - y} + \frac{1}{d + \Delta d + y}\right)\left(V_F^2 - V_B^2\right) \tag{5.9}$$

Similarly, the lateral force, F_y, is given as:

$$F_y = \frac{1}{2}\frac{\partial C_F}{\partial y}V_F^2 + \frac{1}{2}\frac{\partial C_F}{\partial y}V_B^2 \tag{5.10}$$

and, after substituting (5.6) and (5.7) into (5.10), the lateral force can be expressed as

$$F_y = \frac{1}{2}N\varepsilon_0 T\left[\frac{1}{(d - \Delta d - y)^2} - \frac{1}{(d + \Delta d + y)^2}\right]\left[x_0\left(V_F^2 + V_B^2\right) + x\left(V_F^2 - V_B^2\right)\right] \tag{5.11}$$

Notice that when $\Delta d=0$ lateral force exists only if y is not zero.

Eqs. (5.1) and (5.5), together with (5.9) and (5.11), represents the dynamic model of the actuator in two DOF. The model is nonlinear and coupled through the generation of the electrostatic forces in (5.9) and (5.11).

5.3 Model Verification and Refinement

The model developed in Section 5.2 presents an overview of the dynamic behavior of the device. However, it does not accurately represent the actual device. Therefore, several refinements are needed, and several parameters need to be determined. The interdigitated capacitances are assumed to be larger than the capacitances due to the finite aspect ratio and fringing fields.

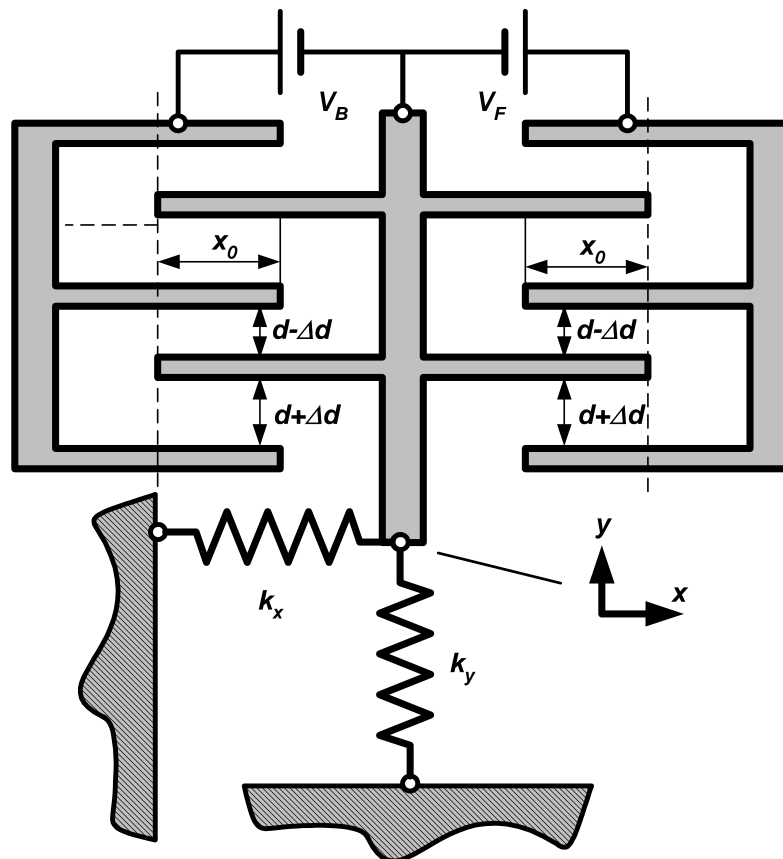

Figure 5.4 Comb drive with *Δd* used to model the unbalanced lateral geometry.

Consequently, the force can be modified by a constant, determined from the experimental results. A set of FEA computations were conducted to determine the aspect ratio and contribution of the fringe fields, and to determine the y and z dependence of the capacitance. The lateral "unbalance" coefficient, Δd, was determined from the experimental results, and the model was refined into its final form.

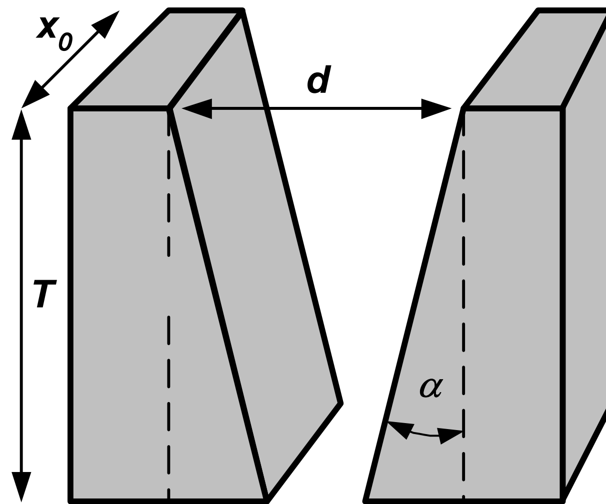

Figure 5.5 Illustration for calculating the influence of the final aspect ratio angle, α, on the capacitances, C_F and C_B, for the DRIE fabricated comb drive electrodes [27].

The device described in this paper is fabricated using DRIE. So far, it has been assumed that the sidewalls of the device are perfectly perpendicular to the substrate (see dashed lines in Figure 5.5). However, in reality, this is not true. As illustrated in Figure 5.5, the aspect ratio is not infinite but has a finite value. As such, it modifies the interdigitated capacitance and, consequently, the electrostatic force. The increase of the value of the capacitance as a function of the angle α is given as a capacitance ratio [27]

$$\frac{C(\alpha)}{C(0)} = \frac{g_0}{2T\tan\alpha}\ln\frac{g_0}{g_0 - 2T\tan\alpha} \tag{5.12}$$

$$\lim_{\alpha\to 0}\frac{C(\alpha)}{C(0)} = 1 \tag{5.13}$$

and a plot of the $C(\alpha)/C(0)$ ratio for $d = 2.5\mu m$ is illustrated in figure. 5.6.

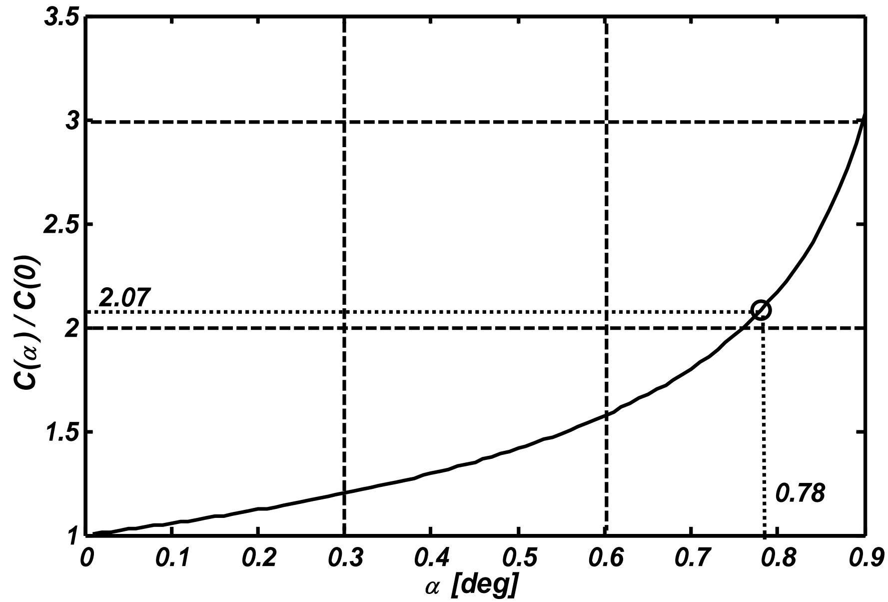

Figure 5.6 The influence of the finite aspect ratio $C(\alpha)/C(0)$ on the capacitances C_F and C_B. For $\alpha = 0.78\ deg$, the ratio of the capacitances is *2.07*.

Besides the finite aspect ratio of the structure, fringing fields also affect the interdigitated capacitance. Generally, the modification of the electrostatic force in terms of the modified capacitance can be described by introducing the constant, η. That is

$$F_m = \frac{1}{2}\frac{\partial(\eta C_0)}{\partial x}V^2 = \frac{1}{2}\eta\frac{\partial C_0}{\partial x}V^2 = \eta F_0 \tag{5.14}$$

Applying (5.14), to the model in (5.2) and (5.4), yields

$$m\ddot{x} + d_x\dot{x} + k_x x = \eta F_x \tag{5.15}$$

$$\frac{J_z}{L_A}\ddot{y} + \frac{d_\theta}{L_A}\dot{y} + \frac{k_\theta}{L_A}y = -\eta F_Y L_A \tag{5.16}$$

Assuming steady-state conditions, the model in (5.15) and (5.16) reduces to

$$k_x x = \eta F_x = k_{ex} V_F^2 \tag{5.17}$$

$$\frac{k_\theta}{L_A}y = \eta F_Y L_A \tag{5.18}$$

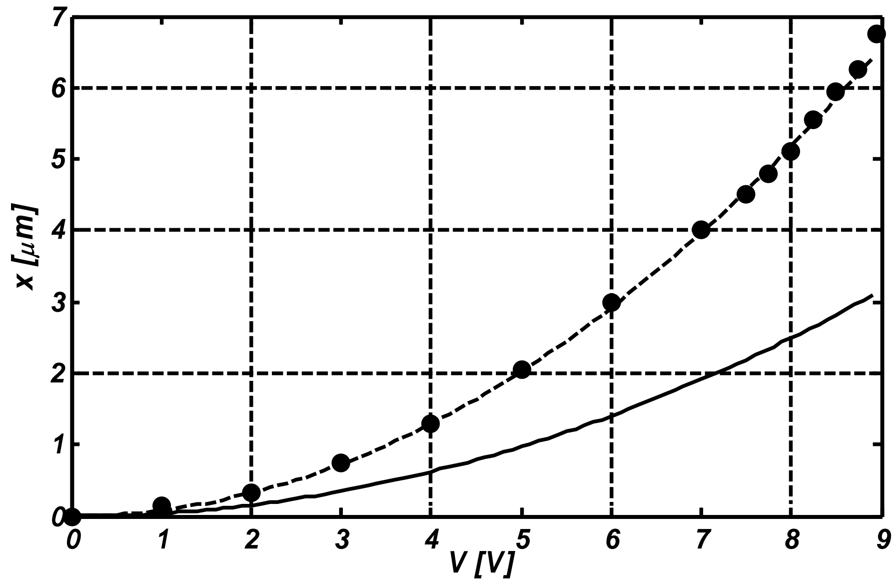

Figure 5.7 Experimental deflection vs. voltage relationship associated with the input nonlinearity of the system [43].

Both experimental and analytical determined curves of (5.17) are plotted in figure 5.7 [43]. The theoretically calculated value (k_{ex}/k_x) fits for $0.039\mu mV^{-2}$. Experimental results, however, show that its value is $0.081\mu mV^{-2}$. The ratio between

these two functions is $\eta = 2.07$ (see figure 5.6). It is important to mention that the experimental observation shows that the influence of the lateral motion over the majority of the travel range of the actuator is negligible. Lateral movement does not affect the force in the x-direction. Lateral motions become visible when the applied voltage approaches the value of the pull-in voltage. This assumption allows us to determine η independetly from (5.17) and figure 5.7.

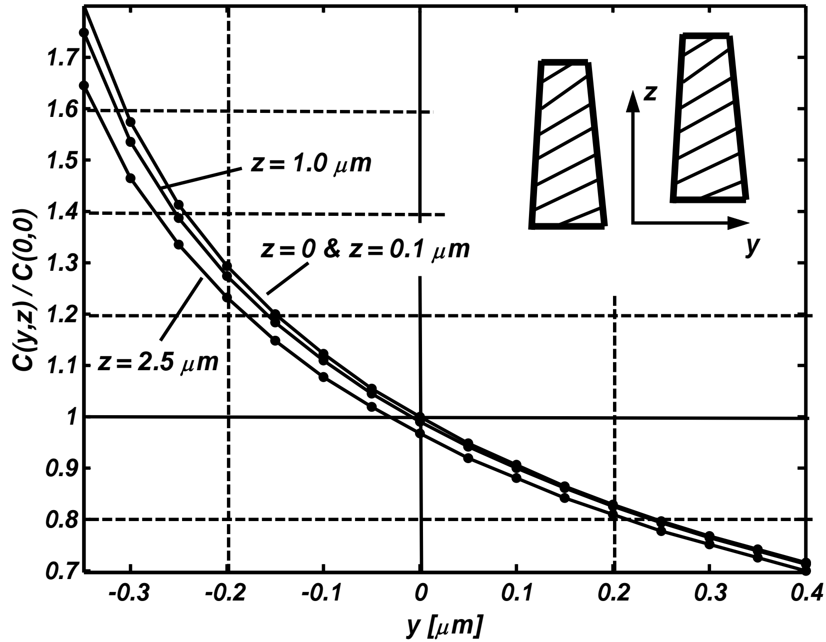

Figure 5.8 Relative increase in the capacitance due to x-z movement of the electrodes. The change in capacitance for $z<0$ can be assumed to be symmetrical.

In order to determine and separate the contribution of the finite aspect ratio and fringing fields on the capacitance, an electrostatic FEA was conducted. The aspect ratio was varied, and the increase in the capacitance was observed. When the capacitance

increase was *2.07* times its original value (5.6)-(5.7), the angle α was computed to be *0.786 deg*. Additionally, the majority of the capacitance increase was due to the finite aspect ratio, and only *2-3%* was attributed to the fringing fields.

Keeping the angle α constant (i.e., *0.786 deg*), another FEA investigation was conducted to observe the influence of the out-of-plane motion on the capacitance. Both y and z were varied over the interval of interest, and the results are shown in figure 5.8.

Figure 5.8. yields several important insights regarding the change in capacitance. The influence of the z-direction, in the worst case, $z = 2.5\mu m$, over the y-range, is *2-10%*. Up to $1.0\ \mu m$, the influence of the out-of-plane motion is hardly visible, especially around $y=0$. Changes due to y motion inside the interval of interest (i.e. $<-0.1,\ 0.1>$); however, are larger than *10%*. The interval of interest is where we expect the controller to limit lateral motion. It is also obvious that any out-of-plane movement [85] will decrease the capacitance and, therefore, cause the structure to develop the force which tends to bring the structure back towards $z=0$. The higher the actuating voltage, the more the out-of –plane motion seems to gain stability.

With η known, the remaining parameter to be determined is Δd from (5.11), which affects F_y in (5.18). The experimental results of the lateral part of the model are shown in figure 5.9. The last stable voltage and lateral deflection before pull-in were $8.96V$ and $0.65\mu m$, respectively. In order to determine the value of Δd from (5.11), which implicitly affects F_y in (5.18), a set of simulations in MATLAB-SIMULINK were conducted. The applied voltage was increased gradually, as it was in the actual experiment. The value of Δd was $0.31\mu m$ when pull-in occures at $8.96V$.

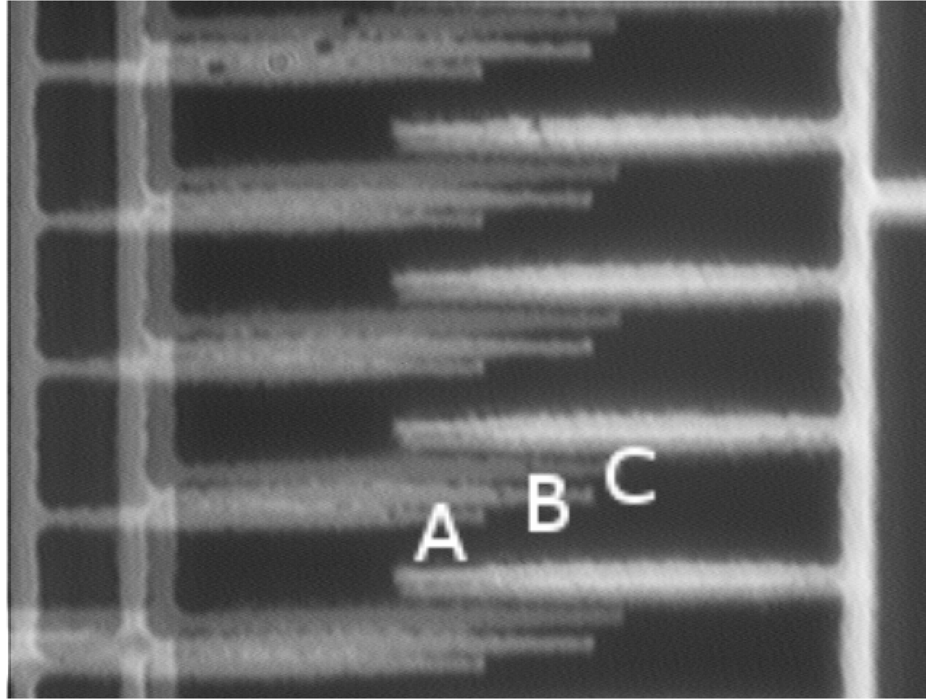

Figure 5.9 Progress of the lateral instability – A) *0* volts, B) stable state immediately before pull-in, $V_F=8.95\ V$, and $y=0.65\mu m$ and C) pull-in.

5.3.1 Model Summary and Characteristics

Summarized, the model looks like

$$m_x\ddot{x} + d_x\dot{x} + k_x x = \eta F_x \tag{5.19}$$

$$\frac{J_z}{L_A^2}\ddot{y} + \frac{d_\theta}{L_A^2}\dot{y} + \frac{k_\theta}{L_A^2}y = -\eta F_Y \tag{5.20}$$

where:

$$F_x = \frac{1}{2}N\varepsilon_0 T\left(\frac{1}{d - \Delta d - y} + \frac{1}{d + \Delta d + y}\right)\left(V_F^2 - V_B^2\right) \tag{5.21}$$

$$F_y = \frac{1}{2} N\varepsilon_0 T\left[\frac{1}{(d-\Delta d-y)^2} - \frac{1}{(d+\Delta d+y)^2}\right]\left[x_0\left(V_F^2+V_B^2\right)+x\left(V_F^2-V_B^2\right)\right] \tag{5.22}$$

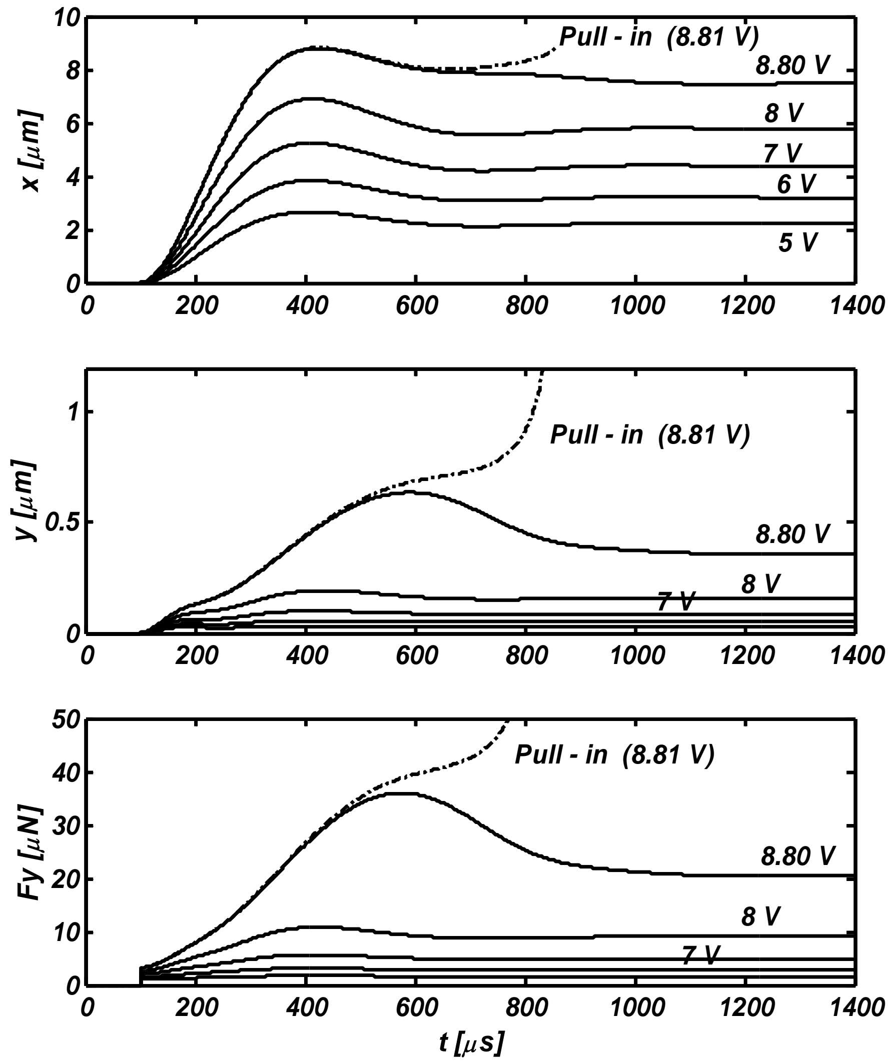

Figure 5.10 Verification of the model. The first simulation was done for a stable voltage step-function with an amplitude of *8.8V,* the second one with the unstable one with an amplitude of *8.81V*.

and the associated parameters are given as follows: $m_X=7.75x10^{-8}$ *kg*, $J_Z=1.88x10^{-15}$ kgm^2; $k_X=1.08$ *N/m*, $k_\theta=3.45e\text{-}6$ *Nm/rad*; $L_A=246\mu m$, $d_X=8x10^{-5}kgs^{-1}$; $\eta=2.07$, $\Delta d=0.31\mu m$, $N=158$, $T=75\ \mu m$, $\varepsilon_0=8.854e\text{-}12Fm^{-1}$ and $x_0=5\mu m$.

The simulation results illustrating the dynamic bahavior of the system at the edge of the lateral instability are shown in figure 5.10. Notice that for transient conditions, the pull-in voltage may be slightly different than for steady state conditions.

5.4 Extended Model for Lateral Actuator/Sensor

With the model of the actual device developed in the section 5.3, the additional features, intended for lateral sensing and actuation, can be added to the device, as shown in figure 5.2b. For the lateral control analysis, these features are assumed not to have mass and damping. The detailed structure of both the lateral actuator and sensor are shown in figure 5.11.

The lateral actuators contain top and bottom comb drive structures designed to generate force in the *y*-direction. These comb drive structures are unbalanced with different gaps (*a* and *b*) between the electrodes, as shown enlarged in figure 5.11. The maximum generated force occurs when the ratio between the smaller and the larger electrode gap is $a/b=0.42$ [27]. Hence, the smaller gaps are defined by the minimum processing geometry; i.e., $a=2.5\mu m$. The larger gap is $6\mu m$ wide.

The lateral sensor has a similar gap geometry in order to achieve maximum sensitivity. The number of fingers, N_s, and the initial electrode overlap, x_{So}, may vary. Movable capacitors are connected to the bridge structure through serial capacitors C_s. Deflection in the *y*-direction can be determined from the difference between voltages

V_{sT} and V_{sB}. Note that, due to the bridge structure of the sensor, any out-of-plane motion affects both sensing voltages equally, thereby canceling its influence with respect to lateral sensing. The structure of both the actuator and sensor ensures that no force is generated in the x-direction.

The capacitance of the two parallel top actuating capacitors, C_{TP}, with respect to the x- and y-directions is given as:

$$C_{TP}(x,y) = 2\varepsilon_0 T N_a x_{a0}\left(\frac{1}{a-y}+\frac{1}{b+y}\right) \tag{5.23}$$

Similarly, the two parallel bottom capacitances, C_{BT}, are given as:

$$C_{BT}(x,y) = 2\varepsilon_0 T N_a x_{a0}\left(\frac{1}{a+y}+\frac{1}{b-y}\right) \tag{5.24}$$

Both capacitances in (5.23) and (5.24) do not depend on x. Consequently, their contribution to the force along the x-axis does not exist. The unbalance coefficient Δd is omitted in (5.23) and (5.24), because it is assumed that the sensing voltage is too low to influence lateral instability, and the actuation voltage is assumed to be an issue for the controller.

The total force in the lateral direction , F_{ya}, is given as

$$F_{ya} = \frac{1}{2}\frac{\partial C_{TP}}{\partial y}V_{aT}^2 + \frac{1}{2}\frac{\partial C_{BT}}{\partial y}V_{aB}^2 \tag{5.25}$$

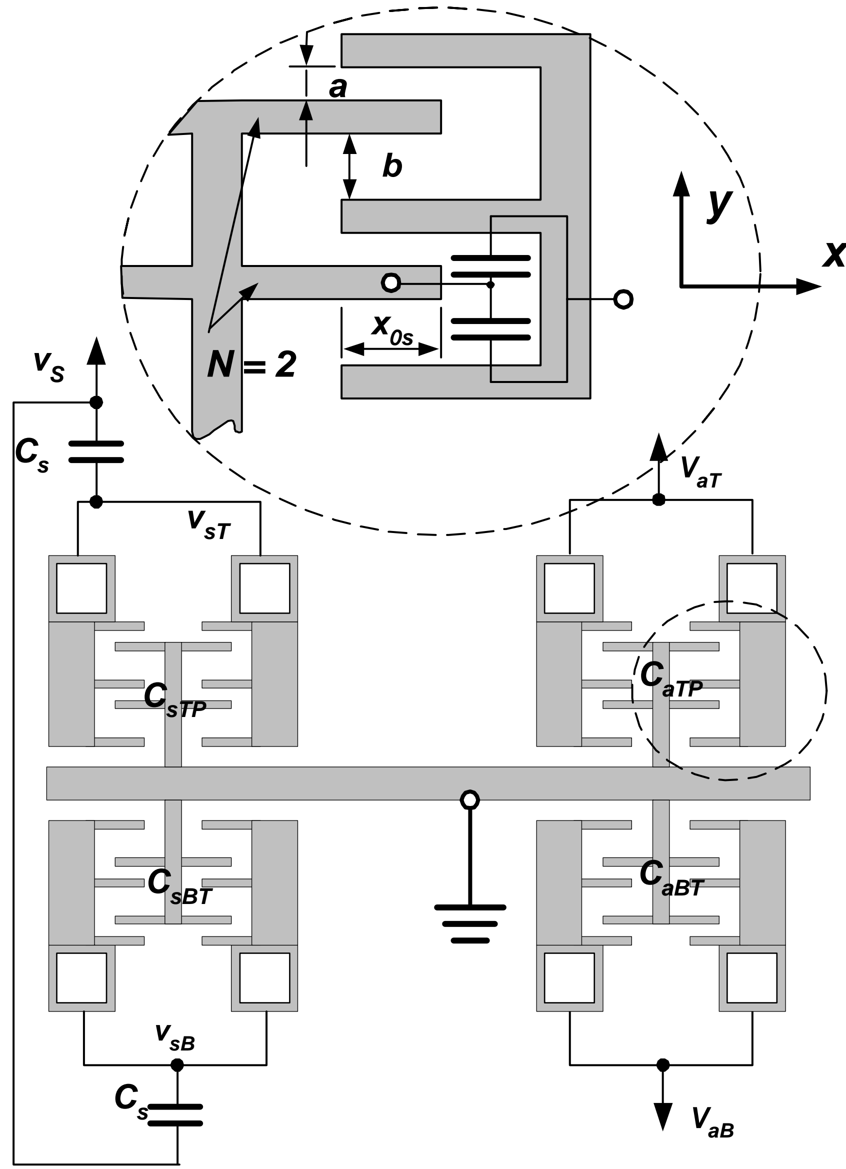

Figure 5.11 Lateral Actuation and sensing schematics.

and, after some algebraic manipulation

$$F_{ya} = \varepsilon_0 T N_a x_{a0} \left[\left(\frac{1}{(a-y)^2} - \frac{1}{(b+y)^2} \right) V_{aT}^2 + \left(\frac{1}{(b-y)^2} - \frac{1}{(a+y)^2} \right) V_{aB}^2 \right] \tag{5.26}$$

Following a similar procedure, the force generated by the sensor is given as

$$F_{ys} = \varepsilon_0 T N_s x_{S0} \left[\left(\frac{1}{(a-y)^2} - \frac{1}{(b+y)^2} \right) V_{sT}^2 + \left(\frac{1}{(b-y)^2} - \frac{1}{(a+y)^2} \right) V_{sB}^2 \right] \tag{5.27}$$

Now, the new forces in (5.26) and (5.27) are integrated into the model in (5.20) as

$$\frac{J_z}{L_A^2}\ddot{y} + \frac{d_\theta}{L_A^2}\dot{y} + \frac{k_\theta}{L_A^2}y = -\eta F_Y + \eta \frac{L_a}{L_A}F_{ya} + \eta \frac{L_s}{L_A}F_{ys} \tag{5.28}$$

Additional parameters, necessary to conduct simulations and design the controller, are: $a=2.5\mu m$, $b=6\mu m$, $N_a=N_s=60$, $La=246\mu m$ $L_s=400\mu m$ and $x_{a0}=x_{s0}=20\mu m$.

5.5 Control System Design

This section describes a feedback approach that prevents lateral pull-in and extends the working range of the comb drive actuator in the *x*-direction DOF. The primary requirement for the controller is to keep $y=0$. Additional shaping of the dynamics is also desirable. The detailed design of the controller is the subject of follow-on research, but the structure, parameters, and operational description are discussed.

The structure of the controller is shown in figure 5.12. In order to simplify the analysis, a PID controller is implemented for the lateral DOF. We assume that the deflection y is measurable and available. When the lateral feedback loop is closed, the sensed value of y is compared to the referent $y=0$, and the error signal is then passed through the controller. Saturation-type nonlinearities distribute voltages to the two channels leading to the left and right *y*-direction comb drive electrodes. The signal is then taken through the square root functions that take care of the electrostatic force being dependent on the squared value of the voltage (5.11).

In order to keep the controller as simple as possible, the lateral degree of freedom (5.28) can be rewritten as

$$\frac{J_z}{L_A^2}\ddot{y}+\frac{d_\theta}{L_A^2}\dot{y}+\frac{k_\theta}{L_A^2}y=\eta\frac{L_a}{L_A}F_{ya}+F_D \tag{5.29}$$

where all lateral forces, except for the actuator, are considered as a disturbance to the system, F_D.

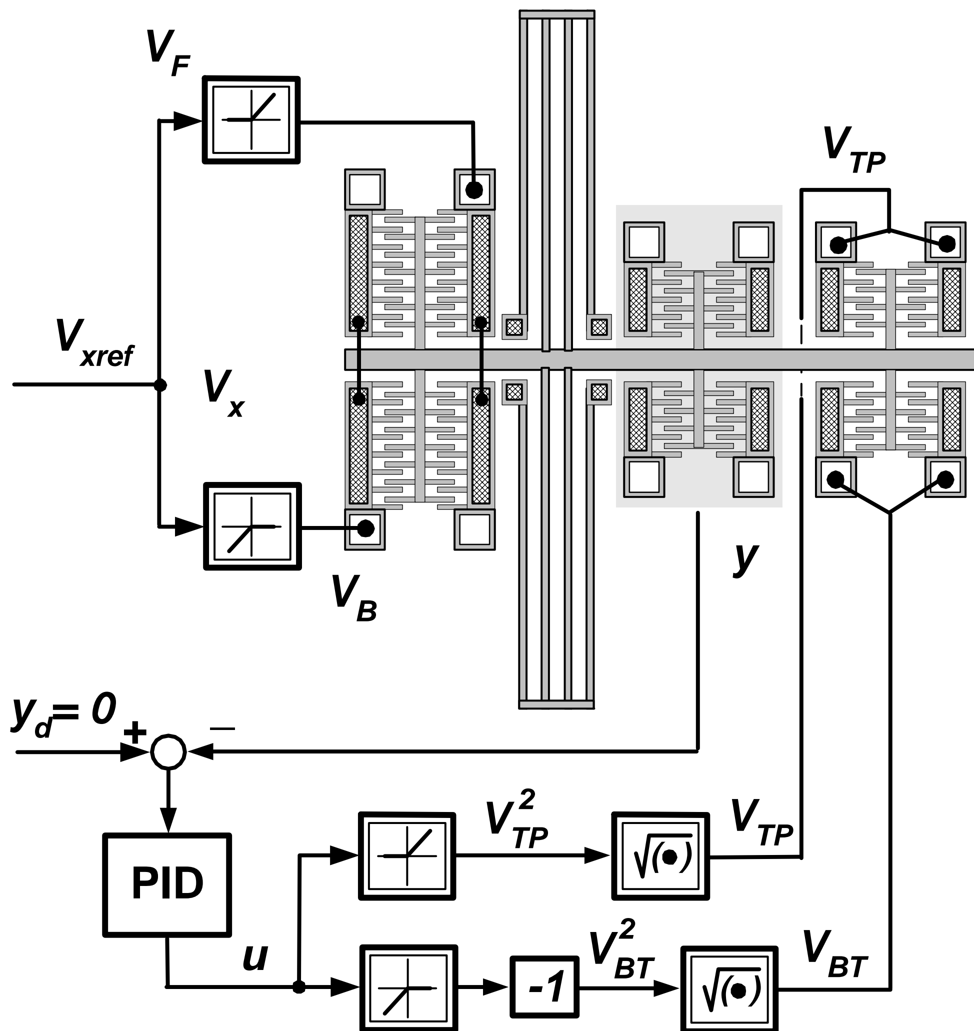

Figure 5.12 Lateral controller.

Furthermore, by substituting $y=0$ into (5.26) yields

$$F_{ya} = \varepsilon_0 T N_A x_{A0} \left(\frac{b^2 - a^2}{a^2 b^2} V_{aT}^2 + \frac{a^2 - b^2}{a^2 b^2} V_{aB}^2 \right) \tag{5.30}$$

Merging (5.29) and (5.30), and defining $k_{ab} = \left(b^2 - a^2\right) / (ab)^2$, yields

$$\frac{J_z}{L_A^2} \ddot{y} + \frac{d_\theta}{L_A^2} \dot{y} + \frac{k_\theta}{L_A^2} y = \eta \frac{L_a}{L_A} \varepsilon_0 T N_a x_{a0} k_{ab} \left(V_{aT}^2 - V_{aB}^2 \right) = k_L \left(V_{aT}^2 - V_{aB}^2 \right) \tag{5.31}$$

with $k_L = \eta (L_a / L_A) \varepsilon_0 T N_a x_{a0} k_{ab}$.

The controller is of the PID type, and it is given as [44]

$$\begin{gathered} u = -Py - D\frac{dy}{dt} - I\int_0^t y(\tau)d\tau \\ V_{aT} = \sqrt{u} \quad u \geq 0, \quad V_{aB} = \sqrt{-u} \quad u < 0 \end{gathered} \tag{5.32}$$

The parameters of the controller (5.32) are chosen as $P=7.5x10^3\ V^2m^{-1}$, $D=5x10^{-2}sV^2m^{-1}$, and $I=7.5x10^8\ V^2m^{-1}s^{-1}$. The PID controller is shown in figure 5.12.

A simulation was first conducted for the case without and with the controller at the edge of the lateral instability; i.e., a *8.96V* signal was applied to the comb drive actuator. The results are shown in figure 5.13. It is obvious that the controller takes care of the lateral motion, not allowing the actuator to rotate around the *z*-axis.

Next, a set of simulations, shown in figure 5.14, depict the controlled case when different voltages, all of them higher than the pull-in value, have been applied to the actuator. It can be seen that the controller keeps the lateral motion at zero. Achievable deflections depend on how much force the lateral steering actuators can provide, and

their values are several times larger than the maximum deflection in the uncontrolled case (i.e., $6.75\mu m$).

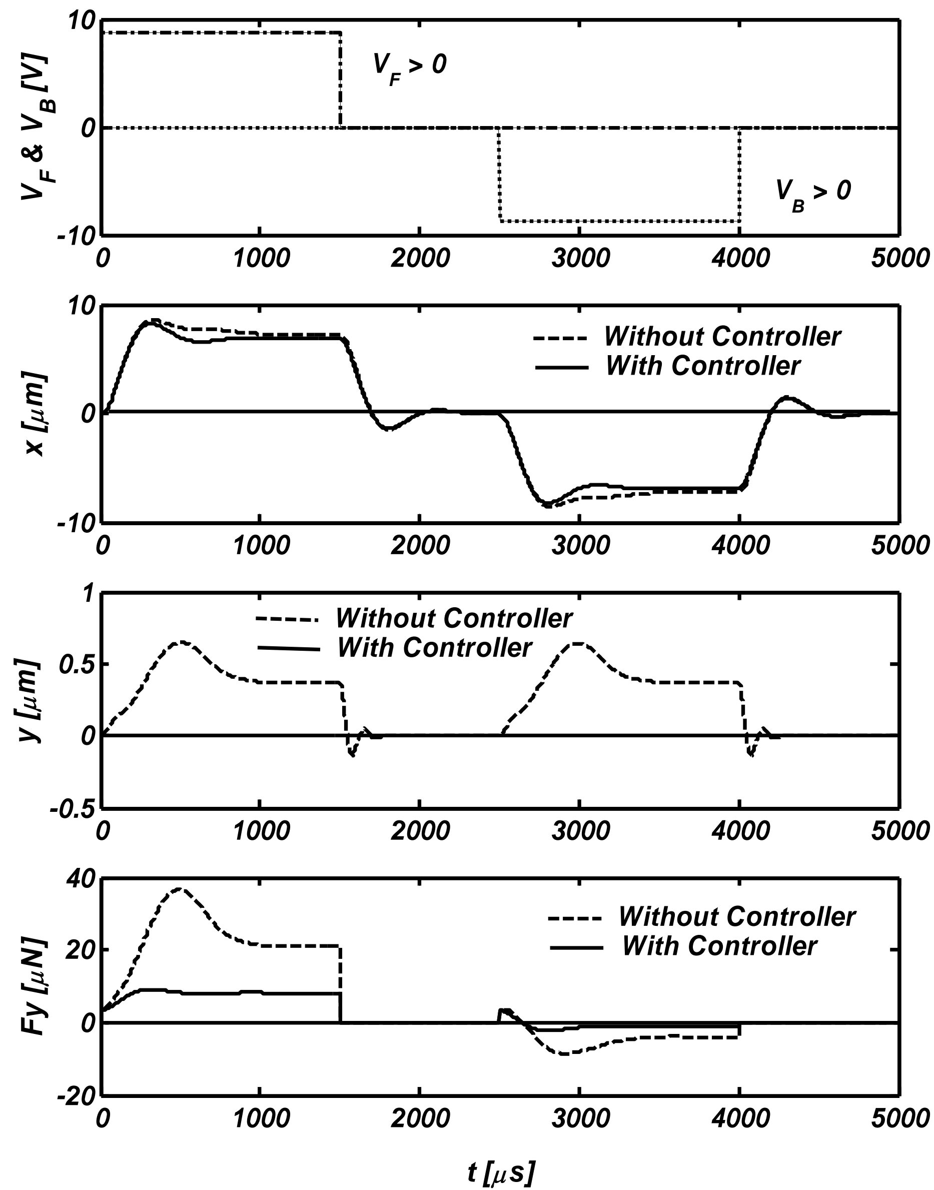

Figure 5.13 The dynamic behavior of the system with and without the controller for the step input ($8.8V$).

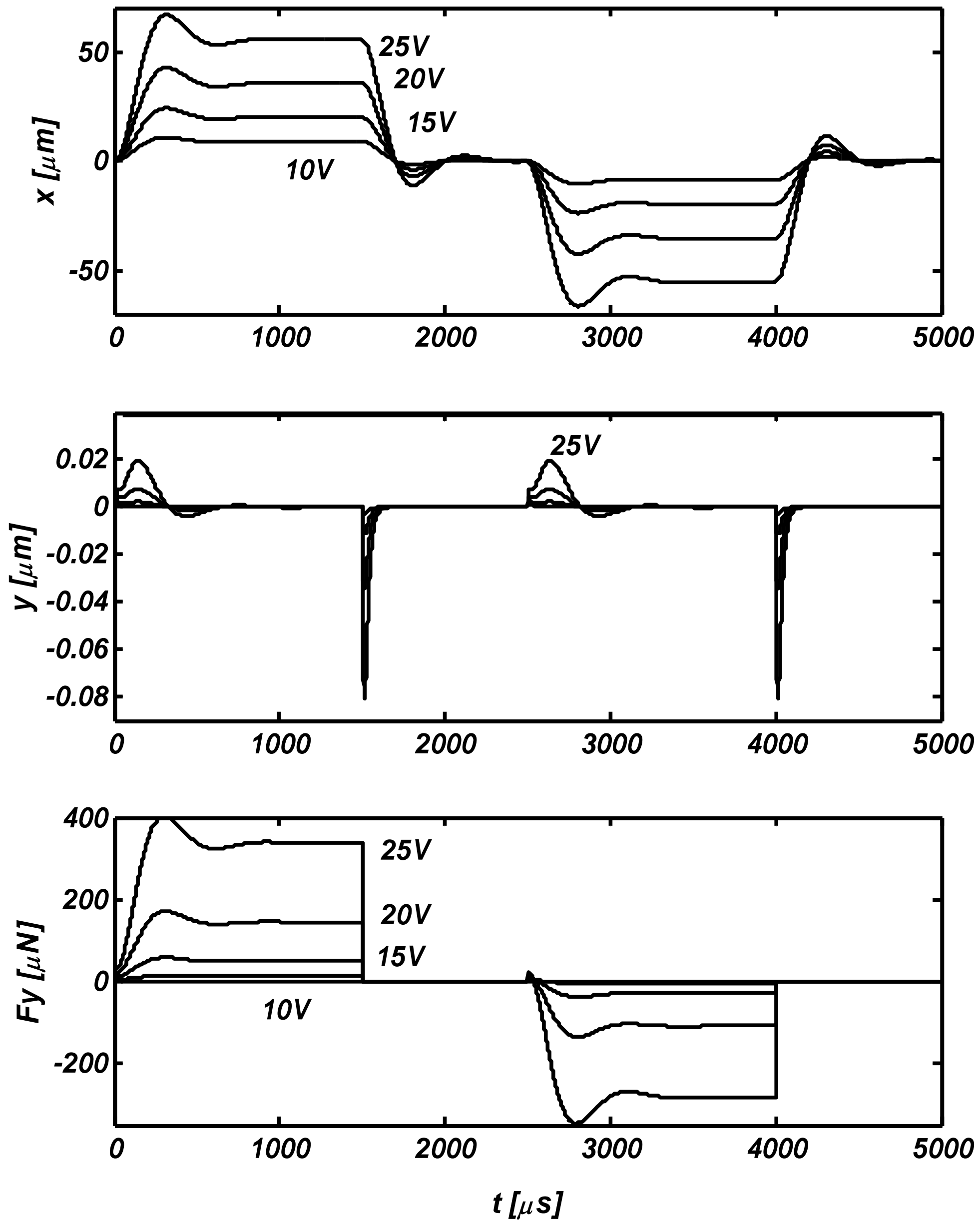

Figure 5.14 Dynamic behavior of the controlled system for the various voltage levels. In all cases, the achievable deflections are greater than the maximum value for the uncontrolled case.

5.5.1 Implementation Issues - Discussion

The approach discussed in this paper adds lateral sensor and actuator features on the MEMS electrostatic comb drive device. These features can significantly change the inertia and, consequently, the dynamics of the device. Additional electronics should be added, as well. The sensing function should not be a problem since good techniques are available for capacitance measurements [29], [30], and several commercial companies market sensors with sensitivities in the femtofarads, sometimes even atofarads. If the sensing electronic speed is of concern, there are other approaches available. For example, the measurement of dy/dt and the reconstruction of y [81]. Also, the controller contains electronic circuits that have to be integrated in the device's design. Complex controllers can consume valuable space. Therefore, it is desirable to keep the controller simple.

5.6 Conclusions

A novel approach to counteract the lateral instability of the electrostatic comb drive actuator was presented. The existing comb drive, with its well-developed, experimentally-verified mathematical model in one degree-of-freedom (DOF) [43] was extended with the lateral two DOF model. The parameters of the lateral DOF model were determined through finite element analysis (FEA) and verified by static experimental results. This model was hypothetically extended with both sensor and actuator functions for lateral movement. Additional features were used to design the controller for lateral motion. Observations of the simulation results accomplished for the control system motivated several important conclusions.

The introduction of lateral feedback extends the deflection range of the electrostatic comb drive actuator. The amount of extended deflection depends on how much force is generated with the lateral actuators.

The introduction of lateral feedback may impact the mechanical design of the device. By including the lateral feedback, the suspension can be made less stiff and one can get larger deflections with lower voltages and a smaller MEMS device. Lateral feedback gives more freedom in device design.

Unfortunately, the addition of both the lateral sensor and the actuator to the MEMS device is needed. Additional features increase the inertia of the system and retard the original, axial response. The space for the lateral deflection sensor and the controller electronics needs to be carefully considered.

The approach discussed in this chapter has its advantages and disadvantages. The advantages, however, are promising and may pave the way for using the lateral feedback in practice.

CHAPTER 6

LATERAL MOTION CONTROL OF THE ELECTROSTATIC COMB DRIVE: SENSING AND FORCE CONTRIBUTION MODEL

6.1 Introduction

In chapter 5, the feedback approach was used to counteract the lateral instability problem related to electrostatic comb drive actuators. It was also mentioned that the requirement for doing so is to have the ability to sense lateral motion. The lateral deflection was, however, assumed to be available, and there was no focus on the sensing strategy. The sensor for lateral stability sensing can not be neglected and it is, therefore, analyzed in detail in this chapter.

Motivated by this idea, a new comb actuator structure with built-in sensors that allows feedback control of axial as well as lateral motion was developed. The model of this structure is given in two DOF. The sensor is shown to be able to sense and distinguish lateral from axial motion and is not affected by out-of-plane motions. Special attention was paid to sensor sensitivity, influence of the sensing electronics to measurement, and the force contribution model. This novel design provides a means for more effective control of future comb drive actuators, including control of their lateral instability.

The chapter is organized as follows. A comb drive actuator with a novel sensing / actuating arrangement for the control of lateral instability is described. Its linearized

mechanical model is given in section 6.2. This is followed by the calculation of the capacitances for the new comb structures in section 6.3. Electrostatic forces and their contribution to the motion of the actuator are examined in detail in section 6.4. In section 6.5, the sensitivity of the comb-like capacitive sensors is discussed. Finally, section 6.6 discusses how the capacitance measurements are affected by the choice of an electronic amplifier and by the finite aspect ratio of the Deep-Reactive-Ion-Etching (DRIE) process used to fabricate the device.

6.2 System Description

A general layout of the comb drive with sensors for both lateral and axial motion is shown in figure 6.1. This device is based on a four-element bridge structure that allows the discrimination of positive and negative motion in lateral and axial directions. It consists of a body of the device known as a shuttle, an electrostatic comb drive actuator capable of creating force in the x-direction and torque around z-axis, a suspension, and two capacitive sensors for sensing both x- and y-deflections. The suspension is attached to the shuttle at one end and fixed to the substrate at the other one, enabling limited movements and electrical ground connection. Comb-like structures contain both movable and fixed electrodes. Voltages applied to the actuating electrodes cause generation of the electrostatic forces and movement of the device. Motion is sensed by connecting the sensing capacitances into appropriately designed bridges which will be discussed later, and observing voltages (v_{xi}, v_{yi}) on the fixed electrodes.

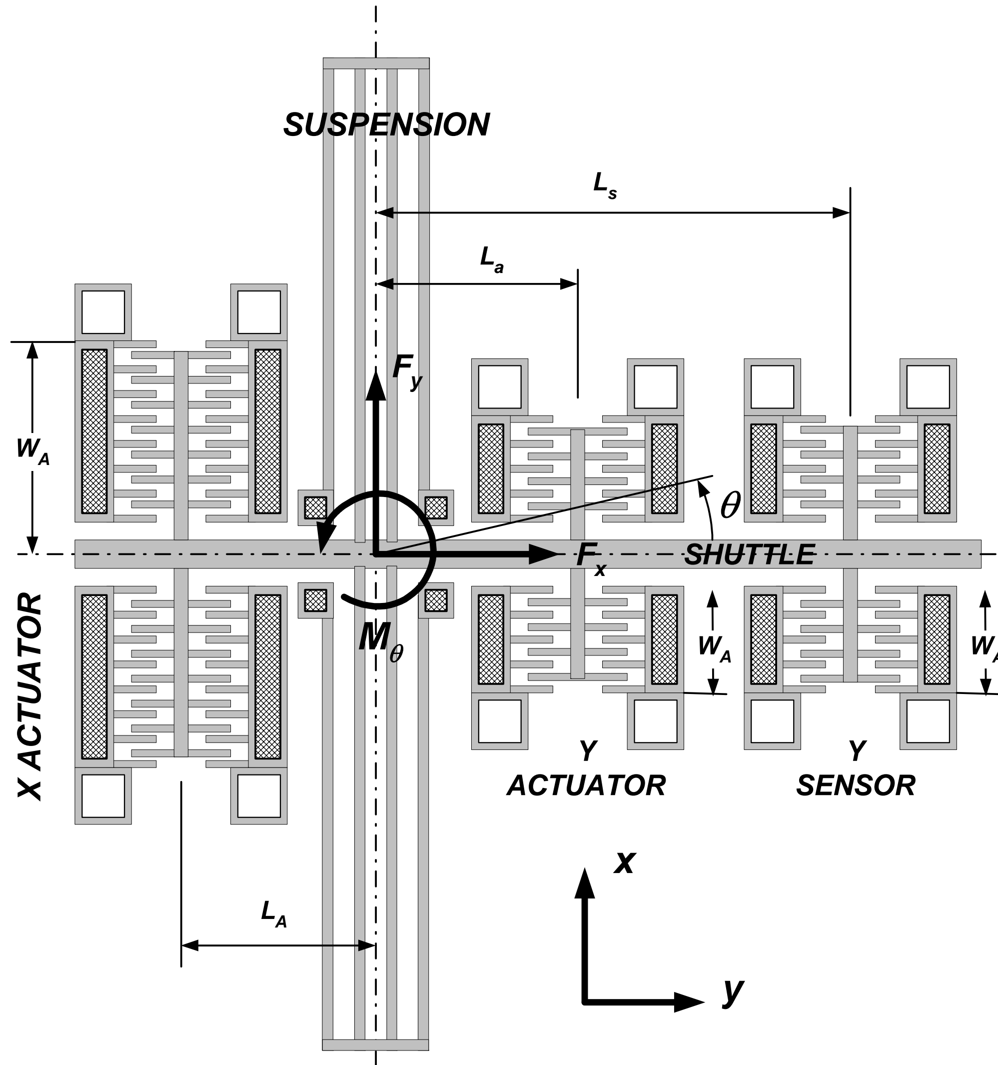

Figure 6.1 Electrostatic comb drive actuator with *x*- and *y*-sensing functionality.

Generally, the mathematical model of the device, shown in figure 6.1, assuming small angle θ, is given as

$$m\ddot{x} + d_x\dot{x} + k_x x = F_x \tag{6.1}$$

$$J_z\ddot{\theta} + d_\theta\dot{\theta} + k_\theta\theta = M_z \quad (6.2)$$

where m and J_z are the effective moving mass and moment of inertia around z-axis, respectively, d_x and d_θ describe damping, and k_x and k_θ are the stiffnesses along the x- and around z- axis, respectively.

Due to small θ and $y << L_y$, we can approximate $\tan\theta = y/L_y \approx \theta$ yielding $\theta \approx y/L_y$, and modifying (6.1) and (6.2) as

$$m\ddot{x} + d_x\dot{x} + k_x x = F_x \quad (6.3)$$

$$\frac{J_z}{L_A^2}\ddot{y} + \frac{d_\theta}{L_A^2}\dot{y} + \frac{k_\theta}{L_A^2}y = -F_Y \quad (6.4)$$

where $m_y = J_z/L_A^2 \;\; d_y = d_\theta/L_A^2 \;\; k_y = k_\theta/L_A^2$ and $F_Y = M_z/L_Y$.

On the other hand, in the sensor model; e.g., the output voltages of the sensor are defined as

$$\begin{bmatrix} v_{x1} & v_{x2} & v_{x3} & v_{x4} \end{bmatrix} = h_X(x, y) \quad (6.5)$$

$$\begin{bmatrix} v_{y1} & v_{y2} & v_{y3} & v_{y4} \end{bmatrix} = h_Y(x, y) \quad (6.6)$$

where $h_X(x,y)$ and $h_Y(x,y)$ are functions that depend on the design of the sensor. The aim of the design is to create $h_X(x,y)$ independent of y, $h_X(x)$, and $h_Y(x,y)$ independent of x, $h_X(y)$. In the following chapter, the focus will be to describe the forces on the left side of (6.3) and (6.4), as well as design and describe of the sensor model for both the x- (6.5) and the y- (6.6) directions.

6.3 Capacitances

Both the generated force and the sensitivity of the position sensors will depend on the capacitance. Therefore, a detailed model of one of three comb drive units shown in figure 6.1, and in more detail in figure 6.2 will be derived. The comb unit contains four comb capacitances, and its model is applicable both for actuation and sensing purposes.

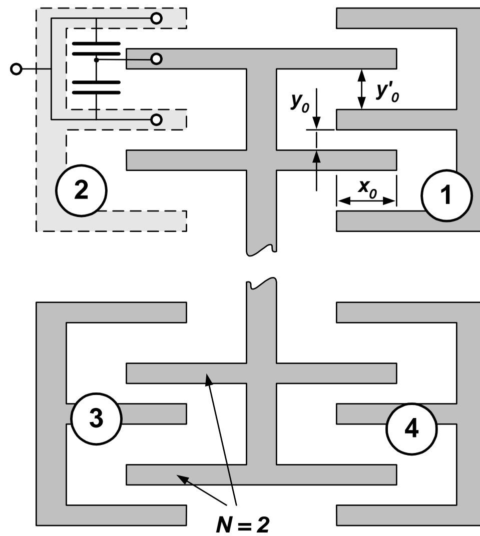

Figure 6.2 Sensing comb unit with four variable capacitors.

6.4 Electrostatic Forces and Contribution Matrix

The capacitance of the first capacitor (see figure 6.2) with respect to x and y is given as

$$C_1(x,y) = \varepsilon_0 TN\left(\frac{x_0 + x}{y_0 - y} + \frac{x_0 + x}{y_0' + y}\right) \tag{6.7}$$

where ε_0 is permittivity of the vacuum, and T is the thickness of the structure. Eq. (6.7) can be rewritten as

$$C_1(x,y) = \varepsilon_0 TN \frac{x(y_0 + y_0') + x_0(y_0 + y_0')}{y_0 y_0' - (y_0' - y_0)y - y^2} \tag{6.8}$$

and by introducing $a = y_0 + y_0'$, $b = x_0(y_0 + y_0')$, $c = y_0' - y_0$ and $d = y_0 y_0'$, equation (6.8) can be simplified as

$$C_1(x,y) = \varepsilon_0 TN \frac{ax + b}{d - cy - y^2} \tag{6.9}$$

Similarly, we can get capacitances for the other three capacitors:

$$C_2(x,y) = \varepsilon_0 TN \frac{-ax + b}{d - cy - y^2} \tag{6.10}$$

$$C_3(x,y) = \varepsilon_0 TN \frac{-ax + b}{d + cy - y^2} \tag{6.11}$$

$$C_4(x,y) = \varepsilon_0 TN \frac{ax + b}{d + cy - y^2} \tag{6.12}$$

In order to determine the forces generated by the electrostatic structures driven by the externally applied voltage, we should observe the co-energy of the system [12], [26]. For the two DOF example, the co-energy is given as

$$W' = -0.5Cv^2 + 0.5k_x x^2 + 0.5k_y y^2 \tag{6.13}$$

The change in the co-energy can come from the change in the voltage or the mechanical work from the outside. That is,

$$dW' = -Cvdv + F_x dx + F_y dy \tag{6.14}$$

or, it can be rewritten as

$$dW' = -\left(\frac{\partial W'}{\partial v}\right)_{x,y} dv + \left(\frac{\partial W'}{\partial x}\right)_{v,y} dx + \left(\frac{\partial W'}{\partial y}\right)_{v,x} dy \tag{6.15}$$

For example, if C_1 is considered, the partial derivatives are given as:

$$\left(\frac{\partial W'}{\partial v}\right)_{x,y} = -\varepsilon_0 TN \frac{ax+b}{d-cy-y^2} v \tag{6.16}$$

$$\left(\frac{\partial W'}{\partial x}\right)_{v,y} = -0.5\varepsilon_0 TNa \frac{1}{d-cy-y^2} v^2 + k_x x \tag{6.17}$$

$$\left(\frac{\partial W'}{\partial y}\right)_{v,x} = -0.5\varepsilon_0 TN \frac{(ax+b)(c+2y)}{\left(d-cy-y^2\right)^2} v^2 + k_y y \tag{6.18}$$

The first term on the right-hand side of eq. (6.17) represents the forces in the *x*-direction and, for the four comb capacitors, the set of forces is given as:

$$F_{x1} = 0.5\varepsilon_0 TNa \frac{1}{d-cy-y^2} v_1^2 \tag{6.19}$$

$$F_{x2} = -0.5\varepsilon_0 TNa \frac{1}{d-cy-y^2} v_2^2 \tag{6.20}$$

$$F_{x3} = -0.5\varepsilon_0 TNa \frac{1}{d+cy-y^2} v_3^2 \tag{6.21}$$

$$F_{x4} = 0.5\varepsilon_0 TNa \frac{1}{d+cy-y^2} v_4^2 \tag{6.22}$$

Similar to the *x*-direction, the first term on the right hand side of (6.18) gives the force in the *y*-direction. The corresponding set of four forces are:

$$F_{y1} = \frac{1}{2}\varepsilon_0 TN \frac{(ax+b)(c+2y)}{\left(d-cy-y^2\right)^2} v_1^2 \tag{6.23}$$

$$F_{y2} = \frac{1}{2}\varepsilon_0 TN \frac{(-ax+b)(c+2y)}{\left(d-cy-y^2\right)^2} v_2^2 \tag{6.24}$$

$$F_{y3} = -\frac{1}{2}\varepsilon_0 TN \frac{(-ax+b)(c-2y)}{\left(d+cy-y^2\right)^2} v_3^2 \tag{6.25}$$

$$F_{y4} = -\frac{1}{2}\varepsilon_0 TN \frac{(ax+b)(c-2y)}{(d+cy-y^2)^2} v_4^2 \tag{6.26}$$

Therefore, It can be concluded that the forces are functions of the applied voltage and the displacement in both the *x*- and *y*-directions and of design parameters *N*, y_0, y_0' and x_0. Equations (6.19) to

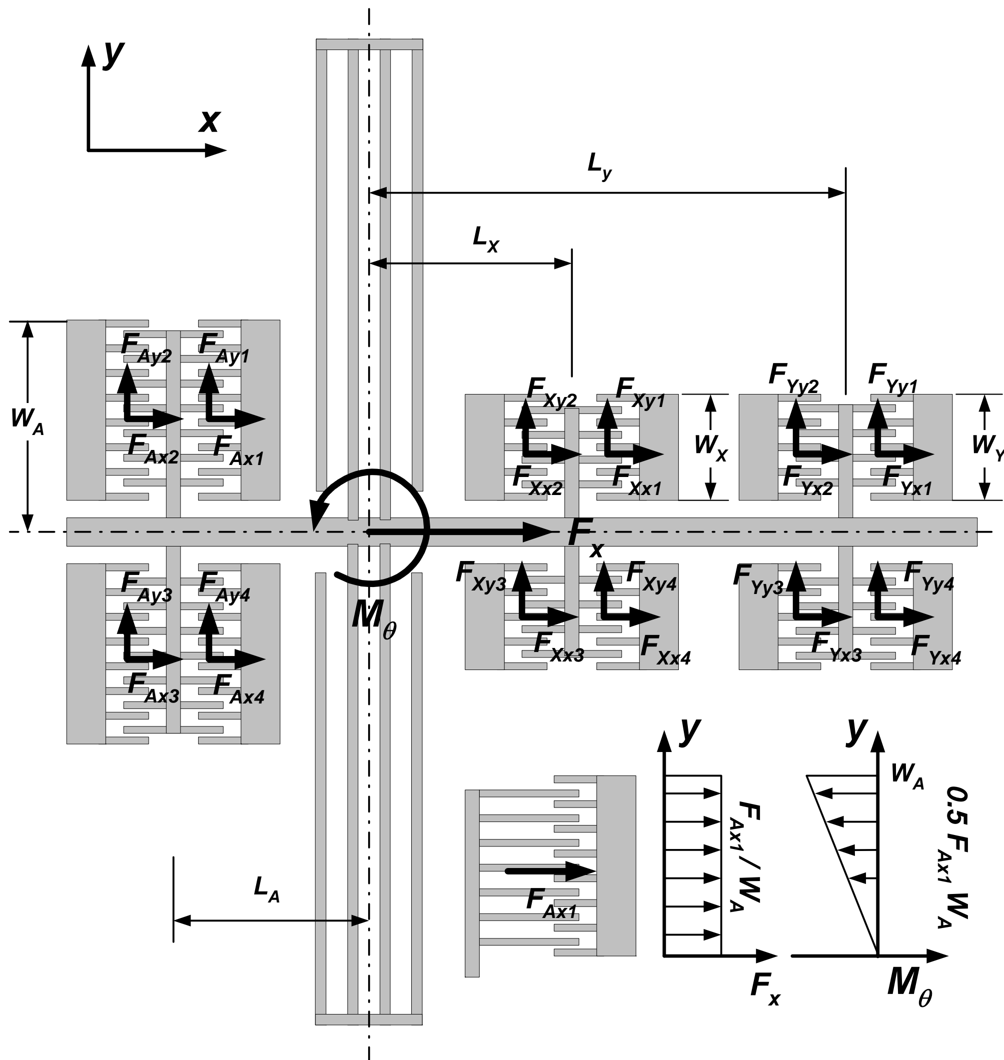

Figure 6.3 Calculation of the force distribution matrix.

(6.26) are valid for all forces, both actuating ones, $F_{Axi}\left(x, y, v_i^2\right)$, $F_{Ayi}\left(x, y, v_i^2\right)$, and the unwanted, parasitic ones, $F_{Xxi}\left(x, y, v_{xi}^2\right)$, $F_{Xyi}\left(x, y, v_{xi}^2\right)$ and $F_{Yxi}\left(x, y, v_{yi}^2\right)$ $F_{Yyi}\left(x, y, v_{yi}^2\right)$ coming from the sensor.

As depicted in figure 6.3. there are many forces acting upon the mechanical model contributing both to the force (6.3) and torque (6.4). From the figure 6.3, the total force along the x-axis, F_x, and the total torque around z-axis, M_z, are given as

$$F_x = \sum_{i=1}^{4} F_{Axi} + \sum_{i=1}^{4} F_{Xxi} + \sum_{i=1}^{4} F_{Yxi} \tag{6.27}$$

$$\begin{aligned} M_z = & -\frac{W_A}{2} \sum_{i=1}^{4} F_{Axi} - \frac{W_X}{2} \sum_{i=1}^{4} F_{Xxi} - \frac{W_Y}{2} \sum_{i=1}^{4} F_{Yxi} - \\ & - L_A \sum_{i=1}^{4} F_{Ayi} + L_X \sum_{i=1}^{4} F_{Xyi} + L_Y \sum_{i=1}^{4} F_{Yyi} \end{aligned} \tag{6.28}$$

While designing the actuator and sensor comb capacitances we have to make sure that part of the force (6.27) and the torque (6.28) generated by the actuating comb unit is larger that the parasitic counterpart generated by the sensors for all values of x and y inside their interval of interest.

6.5 Capacitance sensitivity

The sensor diagram and its principle is shown in figure 6.4. By using variable capacitors in combination with fixed capacitors in a bridge configuration, the capacitance variations can be sensed and their x and y contributions can be properly extracted.

As shown in figures 6.3, 6.4, and 6.5, the design parameters for a particular sensing comb unit are N, y_0, y_0' and x_0. The design requirement is to achieve large

sensitivity ($pF/\mu m$) in x- and low sensitivity in the y-direction for the x sensing element (6.5), shown on the left in figure 6.4, and opposite for the y sensing element (6.6), shown on the right side in figure 6.4.

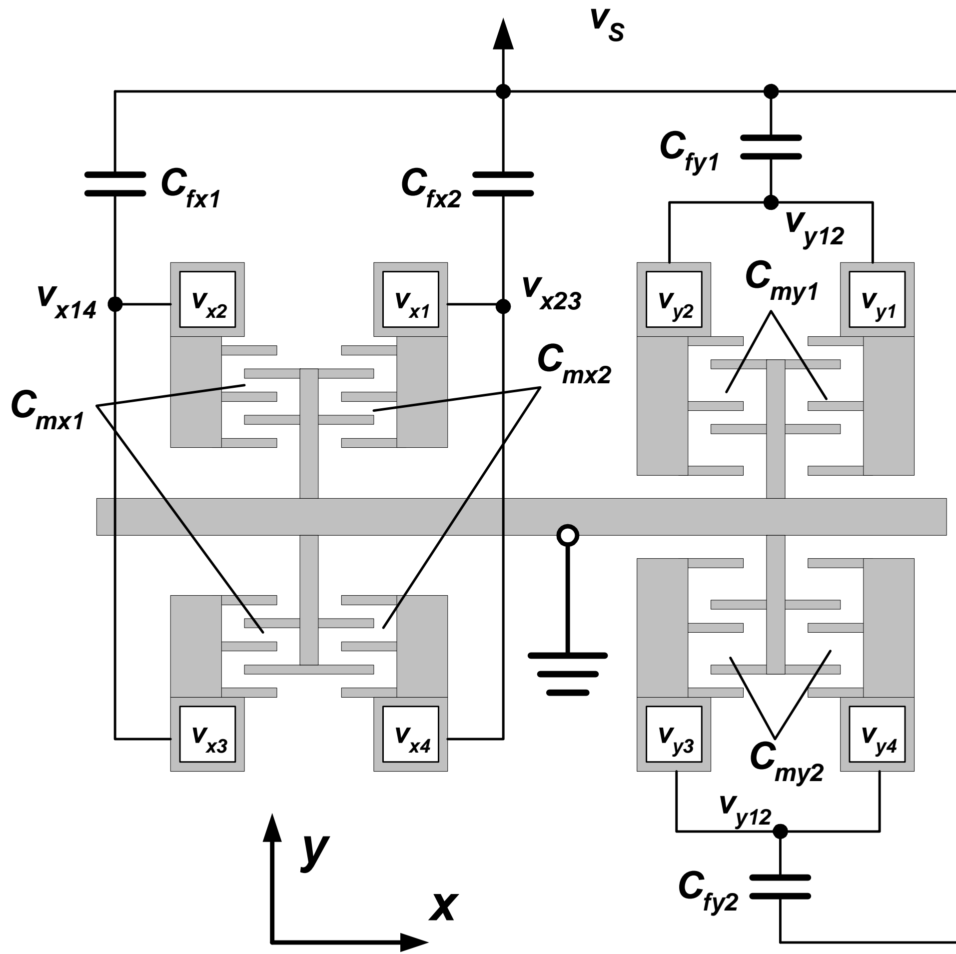

Figure 6.4 Sensing schematics.

In general, the sensitivity is given as

$$\Delta C(x, y) = \frac{\partial C}{\partial x}\Delta x + \frac{\partial C}{\partial y}\Delta y \tag{6.29}$$

The maximal sensitivity in the x-direction and the minimal sensitivity in y-direction can be achieved by keeping the gap minimal and equal on the both sides of the capacitor $y_0 = y'_0$ and by placing the sensor close to the center of rotation to minimize unwanted lateral motion. By applying these conditions, to the sensor configuration shown in figure 6.4, the sensitivity of the sensor in the x-direction reduces to

$$\frac{\partial C}{\partial x} = \frac{2\varepsilon_0 TN}{y_0}, \quad \frac{\partial C}{\partial y} \approx 0 \tag{6.30}$$

For a thickness $T=50\mu m$, it turns out that the sensitivity is $0.17N\ [fF\mu m^{-1}]$ for $y_0=5\mu m$ and $0.11N\ [fF\mu m^{-1}]$ for $y_0=8\mu m$. If we want to increase sensitivity, the only design parameter that can be affected is the number of fingers.

On the other hand, the total capacitances C_{my1} and C_{my2} of the y portion of the sensor are given as the sum of (6.9) and (6.10), and (6.11) and (6.12), respectively. This yields

$$C_{my1}(x, y) = 2\varepsilon_0 TNb \frac{1}{d - cy - y^2} \tag{6.31}$$

$$C_{my2}(x, y) = 2\varepsilon_0 TNb \frac{1}{d + cy - y^2} \tag{6.32}$$

We can see that dependence as well as sensitivity on x cancels out. The sensitivities are given as

$$\frac{\partial C_{my1}}{\partial y} = 2\varepsilon_0 TNb \frac{c + 2y}{\left(d - cy - y^2\right)^2} \tag{6.33}$$

$$\frac{\partial C_{my2}}{\partial y} = -2\varepsilon_0 TNb \frac{c - 2y}{\left(d + cy - y^2\right)^2} \tag{6.34}$$

Rewritten in the terms of design parameters

$$\frac{\partial C_{my1}}{\partial y} = 2\varepsilon_0 TN \frac{x_0\left(y_0 + y_0'\right)\left[\left(y_0' - y_0\right) + 2y\right]}{\left[y_0' y_0 - \left(y_0' - y_0\right)y - y^2\right]^2} \tag{6.35}$$

$$\frac{\partial C_{my2}}{\partial y} = -2\varepsilon_0 TN \frac{x_0\left(y_0 + y_0'\right)\left[\left(y_0' - y_0\right) - 2y\right]}{\left[y_0' y_0 + \left(y_0' - y_0\right)y - y^2\right]^2} \tag{6.36}$$

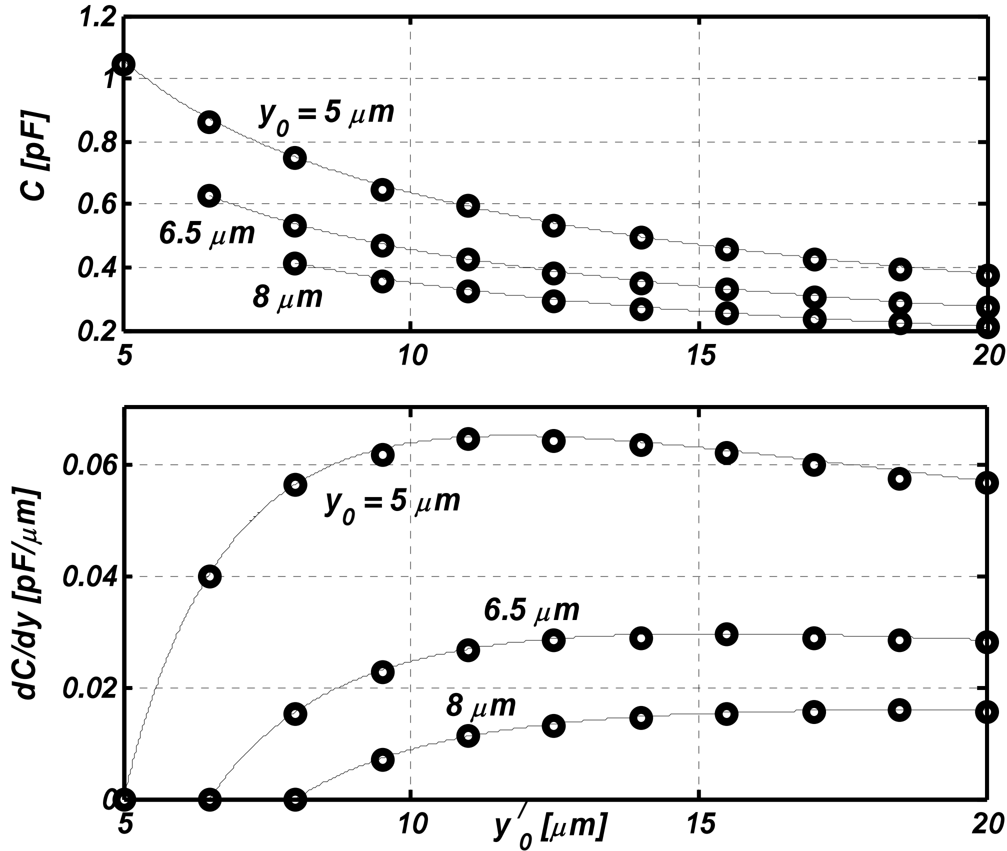

Figure 6.5 Capacitances and a capacitance sensitivity as a function of secondary gap y_0'.

In order to analyze the sensitivities described above, let us see how to determine the parameters in equations (6.35) and (6.36) should we need to fit the sensor into area of known width W_Y and length D_Y, with defined minimal geometry y_0. Parameters that are to be determined are N, y'_0 and x_0. Overlapping x_0 is easily determined as a difference between the given length and twice the maximum expected axial deflection, $x_0 \approx D_Y - 2x_{\max}$. It is desirable for x_0 to be as large as possible to get higher sensitivity.

Furthermore, the minimal functional part of the comb capacitance is defined by two finger widths $2y_0$, minimal gap width y_0, and secondary gap width y'_0. There are N fingers, and as many units and all of them have to fit inside required width W_Y. Mathematically,

$$W_Y > N(3y_0 + y'_0) \tag{6.37}$$

Therefore, increase in y'_0 will decrease the number of finger units that can be fitted into the given W_Y. For a given $W_Y = 1200\mu m$ and $x_0 = 50\mu m$, capacitances and sensitivities for the three values of the minimum geometry ($y_0 = 5\mu m$, $6.5\mu m$ and $8\mu m$) are given in figure 6.5.

As it can be seen in Figure 6b., there exists maximal sensitivity for a certain y'_0. Maximal sensitivity for $y_0 = 5\mu m$, $6.5\mu m$ and $8\mu m$ is obtained with $y'_0 = 11\mu m$, $15.5\mu m$ and $18.5\mu m$, respectively. The corresponding calculated values of fingers are $N_{5\mu m} = 46$, $N_{6.5\mu m} = 34$ and $N_{8\mu m} = 28$. It can be examine now how capacitance changes around $y = 0$ for the values given above.

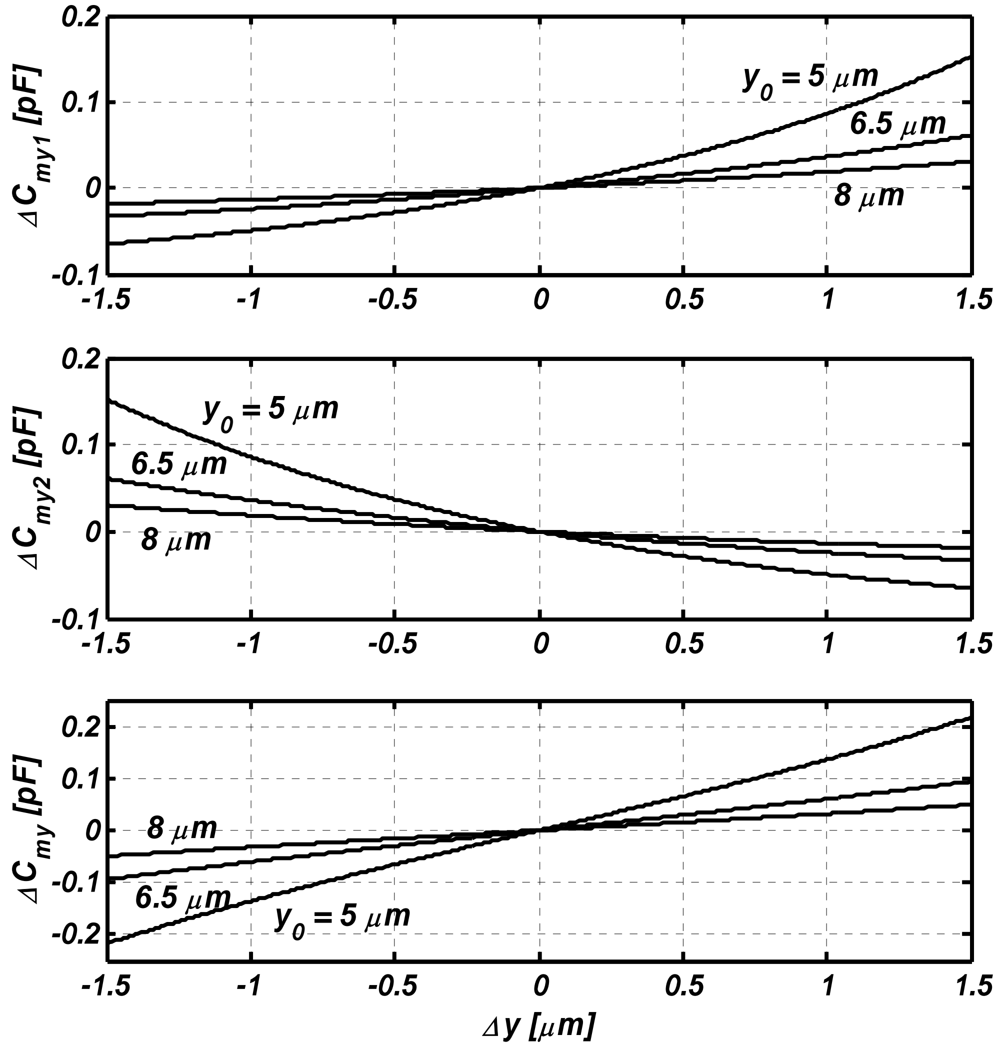

Figure 6.6 Change in capacitances ΔC_{my1}, ΔC_{my2} and ΔC_{my} as a function of y, with y_0 being parameter.

Sensor capacitances at the rest position ($y = 0$) are given as

$$C_{my10} = C_{my20} = 2\varepsilon_0 TNx_0 \frac{y_0 + y_0'}{y_0 y_0'} \tag{6.38}$$

We define $\Delta C_{my1}=C_{my1}-C_{my10}$ and $\Delta C_{my2}=C_{my2}-C_{my20}$. Capacitance changes ΔC_{my1} ΔC_{my2} $\Delta C_{my}=\Delta C_{my1}-\Delta C_{my2}$ as a function of y are shown in figure 6.6. We can immediately see that we have almost linear characteristics for ΔC_{my} for small y.

6.6 Implementation Difficulties

6.6.1 Electronic Circuitry / Influence on Measurement

Recalling the diagrams shown in figure 6.6, one can easily conclude that by choosing small values of capacitances C_f and C_m, and keeping the value of the sensitivity unchanged, there would be no problem with the readout of the differential voltage $v_{y12}-v_{y34}$. For example, if the bridge is driven with $v=10V$, and the values of the capacitances are $C_f=C_m=0.2pF$, a small change on the order of $\Delta C_m=0.01pF$ should produce a voltage difference of Δv_y of approximately $1V$. However, this is not true because when a differential amplifier in attached to the structure to measure Δv_y, it also influences the measurement with its own capacitances. The schematics of the y sensing unit from figure 6.4, with a differential amplifier attached to it, is shown in figure 6.7.

Typically, instrumentation amplifiers [45], which are suitable for the measuring the voltage levels of high impedance (capacitive) bridges, Δv_y, have the following input impedances: $R_d = 5\times 10^{12}\Omega$, $C_d=6pF$, $R_c = 5\times 10^{12}\Omega$ and $C_c=1pF$. When compared to the sensing capacitances of the comb drive, $C_f=0.3pF$ and $C_m=1pF$, these capacitances are larger by more than an order of magnitude. In order to analyze the effects of the parasitic capacitances, it can be assumed that the drive voltage of the bridge is time varying with a frequency that cancels the influence of the resistors. In other words

$R >> \left(2\pi fC\right)^{-1}$. For a critical value of the capacitance change on the order of $C=0.01pF$, the frequency is approximately $1\ kHz$. If the frequency of the bridge voltage is on order of several hundreds kHz, the network in figure 6.7 becomes purely capacitive.

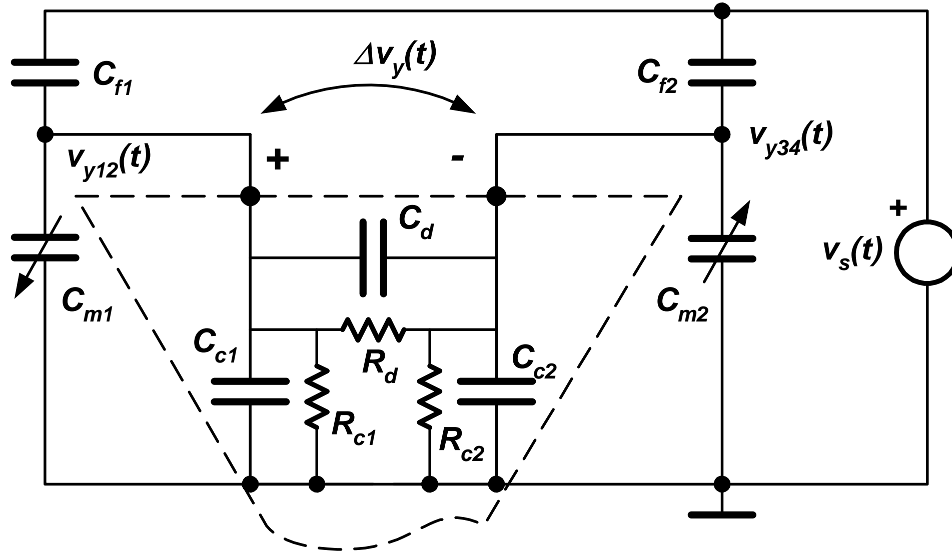

Figure 6.7 Influence of the input of the amplifier on the capacitance measurement.

First, the analysis of the influence of the common mode parasitic capacitance, C_c, will be accomplished. It is shown in figure 6.8 c). Both capacitances change for the same value; i.e., $\Delta C_{c1}=\Delta C_{c2}$. It is obvious that the parasitic capacitance of only $1pF$ decreases the output voltage from several hundreds of mV, as it would be without the amplifier attached, to barely several mV. If the parasitic capacitance is increased several times, the amplitude of the Δv_y goes even below $1mV$. At the same time, the amplitude of the voltages $v_{y12} \approx v_{y34}$ decreases from $2V$ to less than $0.2V$. However, the real problem arises when

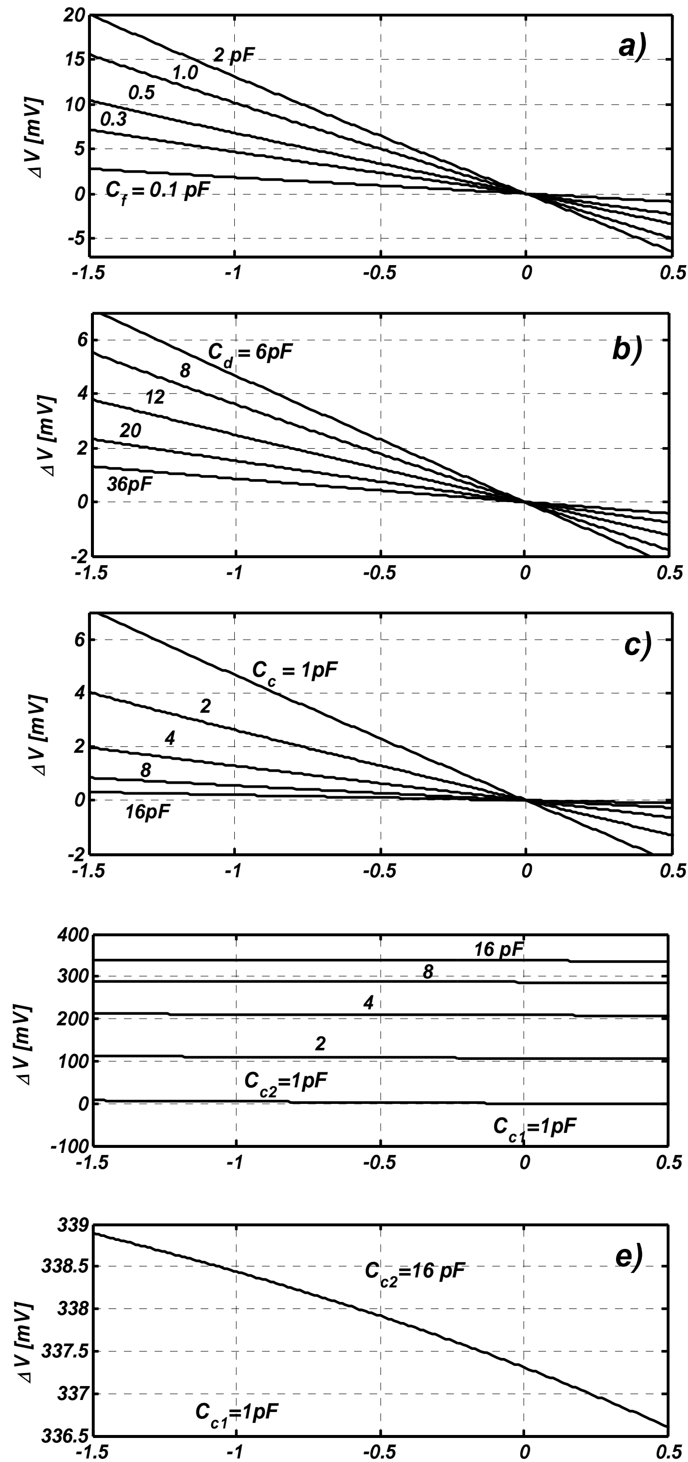

Figure 6.8 Influence of the parasitic capacitances, C_{c1}, C_{c2}, C_d, and the bias capacitance C_f on the amplitude of the differential voltage v_{y12}-v_{y34}.

common mode capacitances differ in value, $\Delta C_{c1}=0$ and $\Delta C_{c2} \neq 0$, and the bridge itself is not balanced. The situation is illustrated in figure 6.8 d), with detail in figure 6.8 e). The sensitivity becomes evidently nonlinear, and Δv_y is heavily biased. The next step is the analysis of the differential input capacitance shown in figure 6.8 b).

In general, the sensitivity can be improved by increasing the value of the capacitance C_f. The influence of the differential parasitic capacitance is shown in figure 6.8 a). It is suitable to accommodate capacitance C_f in the form of a fixed comb capacitor next to the measured capacitances, because that way, we can keep the symmetry of the bridge undisturbed. If the capacitance of a particular comb capacitor is given as $(2N\varepsilon_0 x_0 T)/y_0$, and the corresponding area it covers is given as the product of its length $\approx 1.1x_0$ and width $4Ny_0$. The capacitance per unit area is given as

$$\frac{C}{A} = \frac{2N\varepsilon_0 x_0 T}{4.4Ny_0^2 x_0} = 0.45\frac{\varepsilon_0 T}{y_0^2}\left[\frac{pF}{\mu m^2}\right] \tag{6.39}$$

With minimum features of $y_0=5$, 6.5 and $8\mu m$, and layer thickness $T=50\mu m$, we can accommodate $0.08pF$, $0.05pF$ and $0.03pF$ per $100\mu m \times 100\ \mu m$, respectively. Figure 6.8 a) depicts the increase in sensitivity due to the increase of C_f.

6.6.2 Capacitance vs. Aspect Ratio

The device described in this paper is made by using Deep Reactive Ion Etching (DRIE) micromachining. So far, we have been assuming that the sidewalls of the device are perfectly perpendicular to the substrate. However, in reality, this is not true. As illustrated in figure 6.9, the aspect ratio is not infinite, but has a finite slope. Our intention is to analyze the change in capacitance as a function of the slope angle α.

An infinitesimally small part of the capacitance is given as

$$dC = \frac{\varepsilon_0 x_0}{g(z)} dz \tag{6.40}$$

where $g(z) = g_0 - 2z\tan\alpha$ with $z \in [0, T]$. Rewritten as a function of α, equation (6.40) becomes

$$dC = \frac{\varepsilon_0 x_0}{g(z)} dz = \varepsilon_0 x_0 \frac{dz}{g_0 - 2z\tan\alpha} \tag{6.41}$$

To obtain the total capacitance, we integrate equation (6.41) over the thickness

$$C(\alpha) = \varepsilon_0 x_0 \int_{z=0}^{z=T} \frac{dz}{g_0 - 2z\tan\alpha} \tag{6.42}$$

which yields

$$C(\alpha) = \frac{\varepsilon_0 x_0}{2\tan\alpha}\left[\ln g_0 - \ln(g_0 - 2T\tan\alpha)\right] \tag{6.43}$$

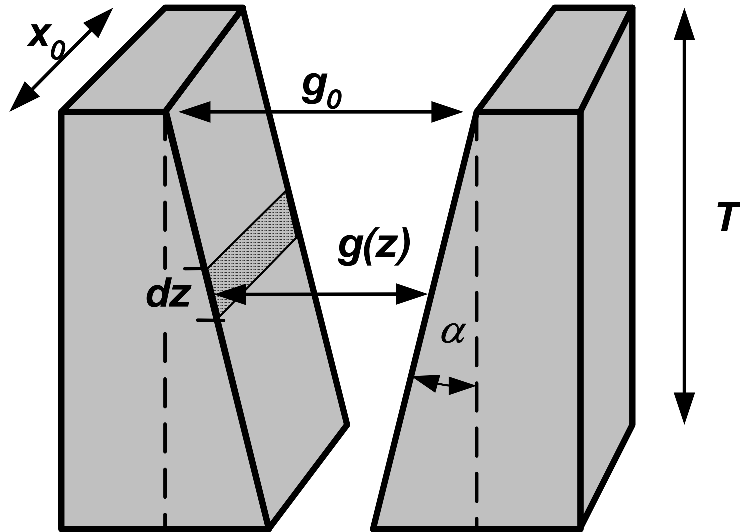

Figure 6.9 Illustration for the calculation of the influence of the final aspect ratio on the capacitances for the DRIE made structures.

or, rewritten

$$C(\alpha)=\frac{\varepsilon_0 x_0}{2\tan\alpha}\ln\frac{g_0}{g_0-2T\tan\alpha} \tag{6.44}$$

In order to check what happens to the capacitance when $\alpha \to 0$, we take the limit of the $C(\alpha)$ resulting in

$$\lim_{\alpha\to 0} C=\frac{\varepsilon_0 x_0 T}{g_0} \tag{6.45}$$

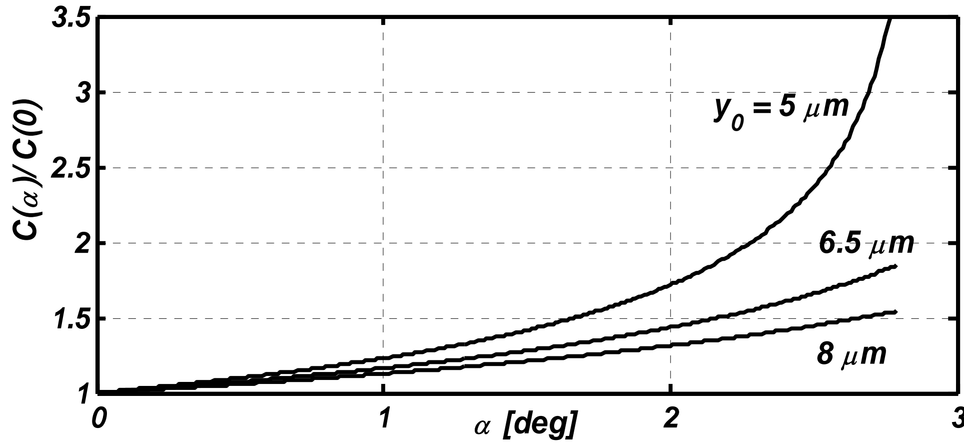

Figure 6.10 Influence of finite aspect ratio on the capacitance for the DRIE made structures.

The increase of the value of the capacitance as a function of the angle α is given as a capacitance ratio

$$\frac{C(\alpha)}{C(0)}=\frac{g_0}{2T\tan\alpha}\ln\frac{g_0}{g_0-2T\tan\alpha} \tag{6.46}$$

and its behavior is illustrated in figure 6.10 for three cases of minimum features, $y_0=5$, *6.5* and *8* μm. The conclusion is that small "minimal features" are very sensitive to fabrication parameters. Therefore, if repeatability of the driving and sensing

capacitances is required, the larger "minimal features" have to be used – in this case *6.5* or *8* μm.

6.7 Conclusions

As it was shown in the previous chapter, the solution to the problem of lateral instability of the electrostatic comb drive actuators can be accomplished by implementing an appropriate control system. One of the requirements to do that is that the lateral motion has to be measurable. Therefore, in this chapter, the modeling of the MEMS electrostatic comb capacitance bridge sensing structure in two degrees of freedom with the purpose of measuring both the lateral and axial motion was accomplished.

A new comb drive actuator device was designed that has sensors in a four-element bridge structure to detect both lateral and axial motion. A two degree-of-freedom model was developed for the new device, and the corresponding performance analysis shows that it provides a suitable structure for more accurate control of comb drive actuators. The bridge-like structure of the sensor diminishes the influence of the out-of-plane motion to the sensing. Special attention was given to the electrostatic forces and to the sensitivity of the capacitance sensor. The impact of introducing a differential amplifier to measure the voltage difference of the bridge was analyzed, as well as the influence of the finite aspect ratio of the fabricated MEMS structure on the value of the capacitances.

CHAPTER 7

CONCLUSIONS

MEMS control and modeling has been shown to be the areas of intensive research and development in both industry and academia. With this in mind, and with the focus on work that has been presented in this dissertation, several conclusions can be drawn.

In chapter 2, a simple novel method for generating a lumped nonlinear dynamical model of an electro-thermo mechanical actuator was presented. The method is based on a combined analytical and FEA approach. Several simple static FEA computations are needed to determine the parameters. The model can be evaluated outside the FEA environment by conducting numerical integration of ordinary differential equations. The structure of the model is reduced to a few states – temperature, velocity and position. The fictitious, average temperature is introduced as a state variable to preserve the energy balance inside the model. The resulting parameters are intuitive and have physical meaning that can be easily related to the geometry and material properties of the device. The model is flexible and enables a separate introduction of various phenomena and external forces. If necessary, a similar procedure can be extended to provide the higher-order degree of the model.

In chapter 3, the comparative analysis between open and close-loop driving of the comb drive is presented. In terms of the complexity for the driving and sensing electronics, an open-loop approach has advantages over closed-loop control since it uses only driving circuits. On the other hand, open-loop driving is extremely sensitive to parameter uncertainties and the shape of the input signal. The choice of actuation strategy depends on the application of the MEMS device, the availability of the sensing technique, the size, and the speed of the device. The most difficult aspect of implementation is related to the hardware implementation, rather than the control algorithms. The control algorithms should be kept as simple as possible. The feedback control definitely gives promising results, but its implementation comes with price. It is worth to continue with the analysis and implementation of the feedback strategies as they promise interesting results and significant improvements of the dynamic behavior of MEMS devices.

In chapter 4, the control scheme from chapter 3 was extended to accommodate light intensity feedback. An experimental setup and a practical system characterization of the light intensity control system for an optical waveform generator are given. The feedback control system is implemented on an actual MEMS VOA from chapter 3. The results verify that the control system proposed here do significantly improve the dynamical behavior of the existing device. It can be assumed that the implementation of the light intensity feedback may improve the accuracy of any VOA. Direct light feedback solves the problem of usually complex and uncertain relationship between position and light intensity. The price to be paid is the implementation of the feedback

itself. The MEMS VOA with its excellent light modulation properties, and wavelength independency, combined with the accuracy provided by controller, represents a flexible and useful tool in the analysis and testing of various optical networks.

In chapter 5, the novel approach for counteracting the lateral instability of the electrostatic comb drive actuators was presented. The existing comb drive from chapter 3, with a well-developed, experimentally verified mathematical model in one degree of freedom (DOF) was extended with the lateral DOF. The parameters of the lateral DOF model are determined through finite element analysis (FEA) and verified by static experimental results. This model was extended hypothetically for both the sensor and actuator for lateral movement. Additional features were used to design the controller for lateral motion. The introduction of lateral feedback extends the range of the electrostatic comb drive actuator. The amount of extension depends on how much force we can generate with the lateral actuators. The introduction of the lateral feedback has impact on the mechanical design of the device. With the lateral feedback in mind, the suspension can be made less stiff, and one can get larger deflections with lower voltages and a smaller size of the MEMS device. Lateral feedback gives more freedom in device design.

Following the results from chapter 5, in chapter 6 the modeling of the sensing structure for the purpose of measuring both the lateral and axial motion was addressed. The new comb drive actuator has sensors in a four-element bridge structure to detect both lateral and axial motion was designed. The sensor structure is not sensitive to the out-of-plane motion. Special attention is paid to the contribution model of the

electrostatic forces and to the sensitivity of the capacitance sensor. The impact of introducing a differential amplifier to measure the voltage difference of the bridge is analyzed.

APPENDIX A

ILLUSTRATIVE EXAMPLE FOR THERMAL ACTUATOR MODELING METHOD

EXAMPLE 1: Basic dynamic model

The first step of the method is establishing the proper FE model in FEA tool; i.e., Ansys, as shown in figure 2.4. The SOLID5 element was used to mesh electro-thermal model. Material properties and geometry are given in tables 2.1 and 2.2. The FEA setup is shown in figure A.1. The model contains the geometry of the thermal actuator and the portion of air between the thermal actuator and the substrate. Voltage is applied to the pads. Temperature boundary conditions are applied to the bottom area representing the substrate.

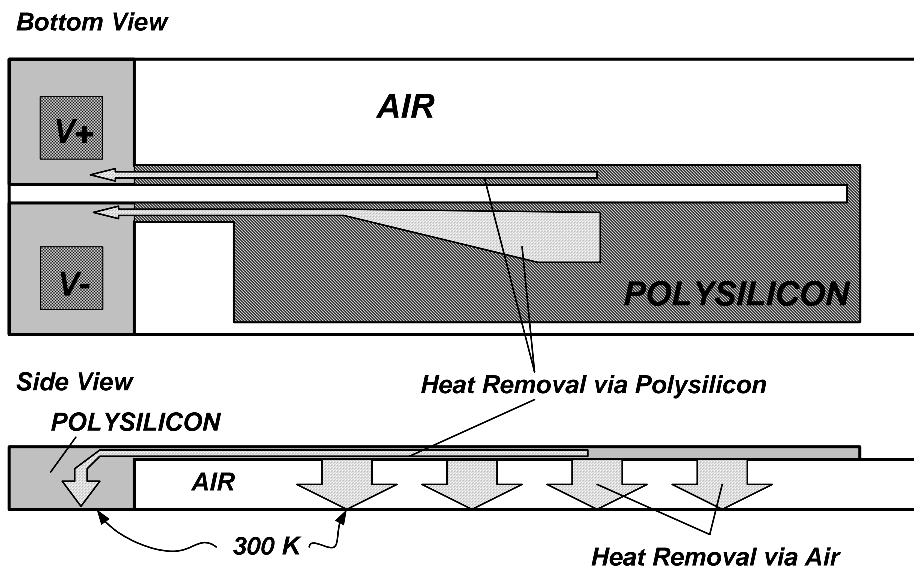

Figure A.1 FE model contains the air box with the actuator body inside. The temperature boundary conditions are applied to the bottom of the box modeling substrate (T=300K). Model is built under assumption that convection and radiation heat removal is negligible.

Since the temperature is expected to reach about *800K*, the radiation effects were not included into the model. Convection through air is also insignificant as

convection does not exist between substrate and the hot and cold arms of the thermal actuator. Instead, the heat removal through the air is modeled as a conduction heat removal mechanism. Note that model should be built as accurate as possible and all effects that may appear should be included. The resulting dynamic model may contain errors if all phenomena are not considered. It is therefore essential to have accurate static FE setup.

Before doing any FEA, the thermal capacitance was calculated assuming it is independent on temperature; i.e.

$$C_{TH} = c_p(T)\rho V \approx c_p \rho V = 2.87 \times 10^{-8}\, WsK^{-1} \tag{A.1}$$

Note that if c_p is dependent on temperature, the calculation for thermal capacitance is done for every voltage load step. The calculation is then closely related to the calculation of the average temperature for each step (2.16). In this example, however, the thermal capacitance is taken to be independent of temperature and can be therefore calculated before conducting any FEA.

Table A.1 Values read out from the FEA.

FEA step *j*	Voltage *[V]*	Total Power *q[mW]*	Max T *[K]*
1	*1*	*0.99*	*309*
2	*2*	*3.88*	*338*
3	*3*	*8.41*	*384*
4	*4*	*14.22*	*445*
5	*5*	*20.88*	*517*
6	*6*	*28.16*	*593*
7	*7*	*35.79*	*674*
8	*8*	*43.71*	*751*
9	*8.4*	*46.73*	*789*

Set of j voltages was applied. It was assumed we were interested only in basic dynamic model; i.e., only total thermal conduction is taken into account. The load voltages, total Joule heat, temperature distributions and maximal temperature were recorded for each load step and are shown in table A.1. Temperature distribution should be recorded, as well. Besides for average temperature calculation, it is used as a load in the subsequent structural FEA.

Calculated, or derived quantities, are shown in table A.2. Electrical current can be calculated from Joule heat and applied voltage. Note that in this example electric current can also be read out from the FEA results as a current density through flexures. Average temperature is calculated according to (2.18).

Table A.2 Values calculated directly from the FEA.

FEA step *j*	Current *[mA]*	T_{avg} *[K]* (2.18)
1	*0.99*	*302.3*
2	*1.94*	*308.8*
3	*2.80*	*318.9*
4	*3.55*	*331.5*
5	*4.17*	*345.5*
6	*4.69*	*359.9*
7	*5.11*	*374.1*
8	*5.46*	*387.6*
9	*5.56*	*393.0*

Electrical conductance is now related to the average temperature as $G_{el}\left(\overline{T}_j\right)=i_j/v_j$, and is given in table A.3. Note that the value of the conductivity for zero voltage should be determined separately. It can be done in two ways. First, its value can be assumed based on the rest of the conductance values from table A.3. The other way is to conduct pure electrical FEA. The value of the applied voltage and the

current density through the actuator flexures gives the temperature-independent conductance, i.e. conductance at room temperature.

Table A.3 Electrical conductance.

Voltage *[V]*	Current *[mA]*	Conductivity *[mA/V]*
0	*-*	*1.00 (est.)*
1	*0.99*	*0.99*
2	*1.94*	*0.97*
3	*2.80*	*0.93*
4	*3.55*	*0.89*
5	*4.17*	*0.83*
6	*4.69*	*0.78*
7	*5.11*	*0.73*
8	*5.46*	*0.68*
8.4	*5.56*	*0.66*

Electrical conductance data from table 3 fits into

$$G_e\left(\overline{T}\right) = 4.54\times10^{-6}\ \overline{T}^{\,2} - 3.80\times10^{-3}\,\overline{T} + 1.48 \qquad \text{(A.2)}$$

and is shown in figure A.2.

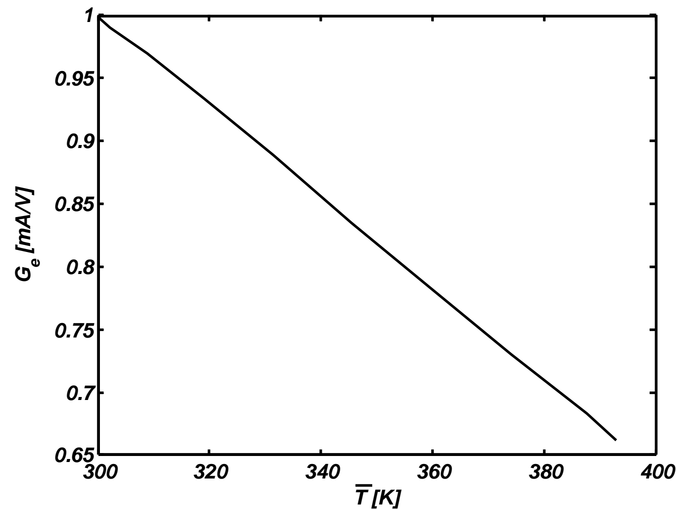

Figure A.2 Electrical conductance as a function of the average temperature. Data from table 3 were curve fitted.

Thermal conductance can be determined from $q(\overline{T})$ and $\overline{T}$. Heat flow *q(T)* corresponds to $i(\overline{T})$ in electrical domain, while $\overline{T}$ corresponds to voltage *v*. Thermal conductivity is now given as $G_{qtot}(\overline{T}) = dq(\overline{T})/d\overline{T}$, corresponding to $G_{el}(v) = di/dv$. Therefore, the first step is fitting $q(\overline{T})$ into curve. Second step is taking the derivative of $q(\overline{T})$. Total Joule heat from the table 1 can be fitted into polynomial

$$q(\overline{T}) = 4.54\times10^{-6}\ \overline{T}^{3} - 3.80\times10^{-3}\,\overline{T}^{2} + 1.48\,\overline{T} - 226.34 \qquad \text{(A.3)}$$

A derivative of (A.3) gives thermal conductance

$$G_{qtot} = \frac{dq(\overline{T})}{d\overline{T}} \qquad \text{(A.4)}$$

or, when (A.4) is calculated

$$G_{qtot}(\overline{T}) = 4.54\times10^{-6}\ \overline{T}^{2} - 3.80\times10^{-3}\,\overline{T} + 1.48 \qquad \text{(A.5)}$$

Thermal conductance is shown in figure A.3.

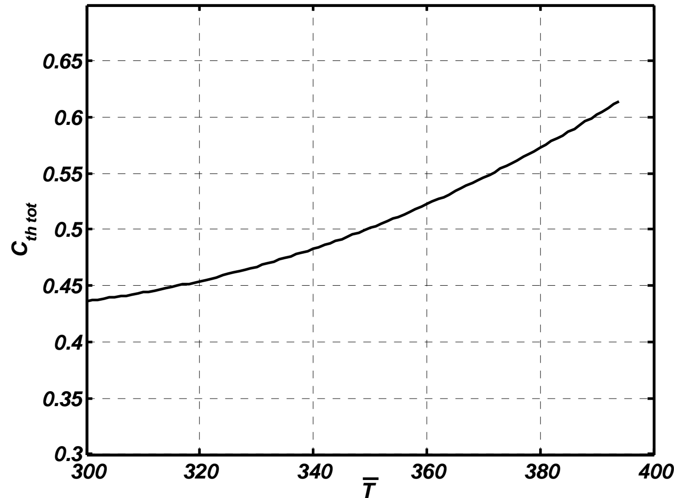

Figure A.3 Total thermal conductance as a function of the average temperature. Data from table 1 were curve fitted and the derivative with respect to the average temperature was taken.

Next step is static structural FEA. The FEA setup is shown in figure A.4. Now, the air region is not of interest anymore so it does not need to be modeled. Temperature distributions $\{T_i\}_j$ are applied as a load to the structural FEA and pads were fixed to the substrate.

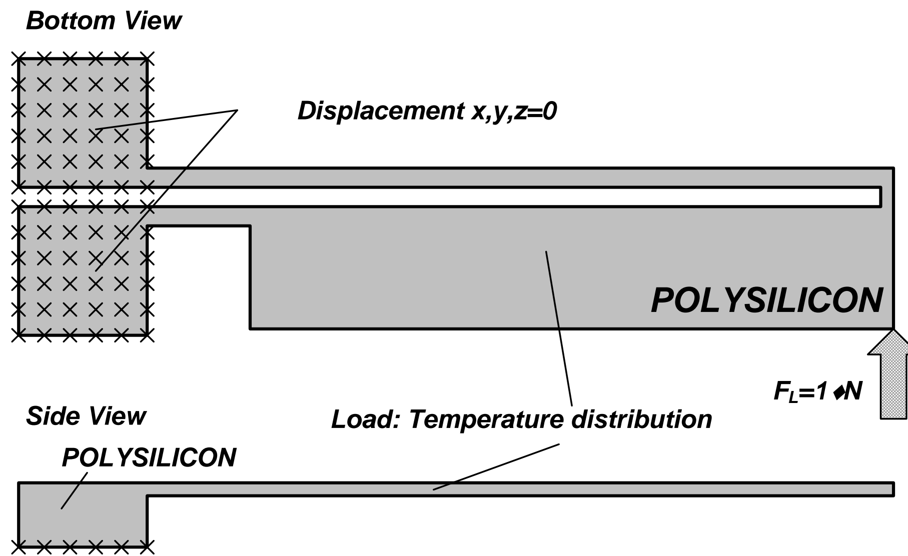

Figure A.4 FE model contains only the body of the thermal actuator. Pads are fixed with displacement boundary conditions. Temperature distributions inside the thermal actuator body, recorded during electro-thermal FEA are applied to the actuator.

For temperature load step j the deflection was recorded and the mass was calculated as shown in the first row of table A.4. Then, the load force of $1\mu N$ was applied to the actuator as it is shown in figure A.4. The FEA is repeated once again and the new deflection was recorded. The difference between original unloaded and loaded deflection was calculated according to (2.29). This is repeated j times and results are shown in table 4.

Table A.4 Mechanical parameters.

Temp. load j	Deflection $[\mu m]$ (rec.)	Mass *[kg]* (2.37) (calc.)	Δx (F_L=1N) (rec.) (2.28)	Calculated k *[N/m]* (2.29)
1	*0.19*	7.9×10^{-12}	*0.19*	*5.25*
2	*0.74*	7.9×10^{-12}	*0.19*	*5.25*
3	*1.70*	7.9×10^{-12}	*0.19*	*5.25*
4	*3.02*	7.9×10^{-12}	*0.19*	*5.25*
5	*4.61*	7.9×10^{-12}	*0.19*	*5.25*
6	*6.35*	7.9×10^{-12}	*0.19*	*5.25*
7	*8.31*	7.9×10^{-12}	*0.19*	*5.25*
8	*10.52*	7.9×10^{-12}	*0.19*	*5.25*
9	*11.27*	7.9×10^{-12}	*0.19*	*5.25*

Now, with $G_{el}(\overline{T})$, $G_{qtot}(\overline{T})$ k and m known, the dynamic model from figure 2.3 is determined. Note that damping was not calculated here but it is easy to do another set of fluid FEA to determine damping and include it into the model.

$$q = G_e(\overline{T})v^2$$
$$C_{th}(\overline{T})\dot{\overline{T}} + G_{qtot}(\overline{T})\Delta\overline{T} = q \qquad \text{(A.6)}$$
$$\overline{m}(\overline{T})\ddot{x} + d\dot{x} + k(\overline{T})x = k\alpha(\overline{T})$$

EXAMPLE 2: Including different heat removal mechanisms

The thermal conductivity from the example 1 was calculated from the total heat dissipation; i.e., Joule Heat. As such, it results in dynamic model but does not give information of how much heat is removed through the polysilicon, through the air, via convection and via radiation. If these effects are to be distinguished in terms of geometry or heat removal mechanism, more data should be recorded from the electro-

thermal simulation than it was done in the example 1. Following modifications result in the same dynamic model. The difference is that heat removal rates are now separated.

Let us assume that the total Joule heat is removed by radiation, convection, and conduction. Generally, Joule heat can be can written as (2.19)

$$q\left(\overline{T}_j\right) = q_{cond}\left(\overline{T}_j\right) + q_{rad}\left(\overline{T}_j\right) + q_{conv}\left(\overline{T}_j\right) \tag{A.7}$$

For example, we are interested in the actuator model when maximal working temperature is less than *800K*. This fact excludes radiation effects from the simulation. We also know that, in the gap between actuator and the substrate heat can not be removed via conduction. It is removed through the air via conduction. Previous equation therefore reduces to

$$q\left(\overline{T}_j\right) = q_{cond}\left(\overline{T}_j\right) \tag{A.8}$$

Conduction; however, contains two parts: conduction through the polysilicon anchors to the substrate and the conduction through the air to the substrate. These two conductions can be separated by expanding equation (A.8) as

$$q\left(\overline{T}_j\right) = q_{cond_poly}\left(\overline{T}_j\right) + q_{cond_air}\left(\overline{T}_j\right) \tag{A.9}$$

Moreover, it may be interesting to see how much heat is removed through the air from the cold arm and hot arm, since the difference influences the deflection. Equation (A.9) can be expanded as

$$q\left(\overline{T}_j\right) = q_{cond_poly}\left(\overline{T}_j\right) + q_{cond_air_cold}\left(\overline{T}_j\right) + q_{cond_air_hot}\left(\overline{T}_j\right) \tag{A.10}$$

This expanding procedure can be continued until all areas of interest are included into analysis. In this example it is assumed that only conduction through the air and polysilicon are of interest and will therefore be addressed (A.9).

The similar FEA setup that had been used in the first example was used in this example. This time, however, more data from FEA were recorded. Table A.1 and table A.2 are now expanded to accommodate recorded heat removal rates through air and polysilicon.

Table A.5 Values read out from the FEA.

FEA step *j*	Voltage *[V]*	Total Power *q[mW]*	Power removed through the air *[mW]*	Max *T [K]*
1	*1*	*0.99*	*0.76*	*309*
2	*2*	*3.88*	*2.99*	*338*
3	*3*	*8.41*	*6.52*	*384*
4	*4*	*14.22*	*11.14*	*445*
5	*5*	*20.88*	*16.56*	*517*
6	*6*	*28.16*	*22.63*	*593*
7	*7*	*35.79*	*29.10*	*674*
8	*8*	*43.71*	*35.63*	*751*
9	*8.4*	*46.73*	*38.50*	*789*

Table A.6 Values calculated from the FEA

FEA step *j*	Current *[mA]*	T_{avg} *[K]* (2.18)	Power removed through the polysilicon *[mW]*
1	*0.99*	*302.3*	*0.23*
2	*1.94*	*308.8*	*0.89*
3	*2.80*	*318.9*	*1.89*
4	*3.55*	*331.5*	*3.08*
5	*4.17*	*345.5*	*4.32*
6	*4.69*	*359.9*	*5.53*
7	*5.11*	*374.1*	*6.69*
8	*5.46*	*387.6*	*8.08*
9	*5.56*	*393.0*	*8.23*

In similar fashion as it was done in example 1, the Joule heat and flow removal rates through the polysilicon and air were curve-fitted and derived. Resulting thermal conductivities are shown in figure A.5.

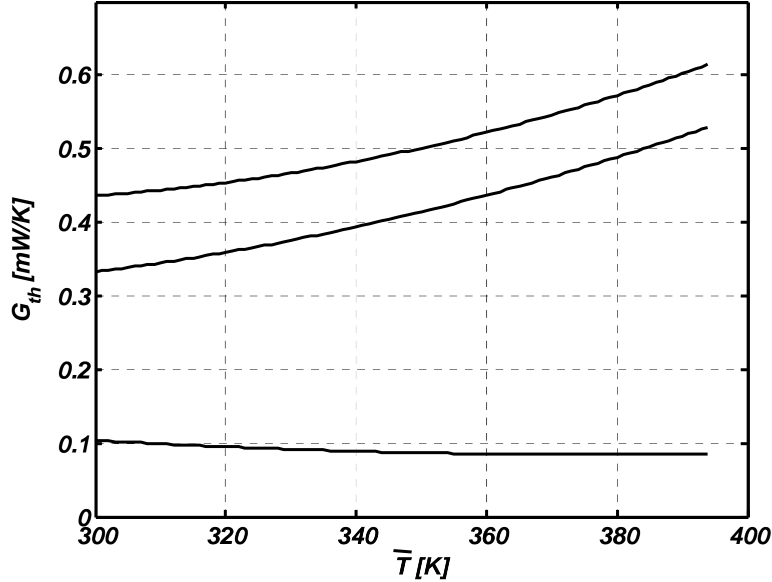

Figure A.5 Thermal conductances. Total thermal conductance, is same as in the figure A.3, is now sum of two thermal conductances – through polysilicon and air.

The rest of the procedure is similar as in example 1. The resulting model is given as

$$\begin{gathered} q = G_e\left(\overline{T}\right)v^2 \\ C_{th}\left(\overline{T}\right)\dot{\overline{T}} + G_{cond_poly}\left(\overline{T}\right)\Delta\overline{T} + G_{cond_air}\left(\overline{T}\right)\Delta\overline{T} = q \\ \overline{m}\left(\overline{T}\right)\ddot{x} + d\dot{x} + k\left(\overline{T}\right)x = k\alpha\left(\overline{T}\right) \end{gathered} \tag{A.11}$$

REFERENCES

[1] J. Bryzek, E. Abbott, A. Flannery, D. Cagle, and J. Maitan, "Control Issues for MEMS," in *Proc. of the 42nd IEEE Conference on Decision and Control*, 2003, vol. 3, pp. 3039-3047.

[2] D. O. Popa, B. H. Kang, J. T. Wen, H. E. Stephanou, G. Skidmore, A. Geisberger, "Dynamic Modeling and Input Shaping of Thermal Bimorph Actuators," in *Proc. of the 2003 IEEE International Conference on Robotics & Automation*, 2003, vol. 1, pp. 1470-1475.

[3] A. Q. Liu, X. M. Zhang, C. Lu, F. Wang, C. Lu, and Z. S. Liu, "Optical and Mechanical Models for a Variable Optical Attenuator Using a Micromirror Drawbridge," *Journal of Micromechanics and Microengineering,* vol. 13, no. 3, pp. 400-411, May 2003.

[4] J. Li, Q. X. Zhang, and A. Q. Liu, "Advanced Fiber Optical Switches Using Deep RIE (DRIE) fabrication," *Sensors and Actuators A: Physical,* vol. 102, no. 3, pp 286-295, Jan. 2003.

[5] F.L. Lewis and V. Syrmos, *Optimal Control*. New York: John Wiley & Sons, 1995.

[6] S.D. Senturia, N. Aluru, and J. White, "Simulating the Behavior of MEMS Devices: Computational Methods and Needs," *Computational Science and Engineering, IEEE,* vol. 4, no.1, pp. 30-43, Jan-March 1997.

[7] A. A. Geisberger, N. Sarkar, M. Ellis, and G. D. Skidmore, "Electrothermal Properties and Modeling of Polysilicon Microthermal Actuators," *Journal of Microelectromechanical Systems*, vol. 12, no. 4, pp. 513-523, Aug. 2003.

[8] Y. Yang and K. Shen,"Nonlinear heat–transfer macromodeling for MEMS thermal devices," *Journal of Micromechanics and Microengineering,* vol. 15, no. 2, pp. 408-418, Feb. 2005.

[9] R. Hickey, D. Sameoto, T. Hubbard, and M. Kujath,"Time and frequency response of two arm micromachined thermal actuators," *Journal of Micromechanics and Microengineering,* vol. 13, no. 1, 40-46, Jan. 2003.

[10] E. S. Kolesar, Ko, S., Howard, J., Allen, P., Wilken, J., Boydston, N., Ruff, M., and Wilks, R., "In-Plane Tip Deflection and Force Achieved with Asymmetrical Polysilicon Electrothermal Microactuators," *Metallurgical Coatings and Thin Films 2000*, vol. 2, *Elsevier Science Publishers*, 2001, pp. 719-726.

[11] D. M. Burns and V. M. Bright, "Design and performance of a double hot arm polysilicon thermal actuator," in *Proc. of SPIE,* vol. 3224, pp. 296—306, 1997.

[12] S.D. Senturia, *Microsystem Design*. Norwell: Kluwer Academic Publishers, 2000.

[13] B. D. Jensen, S. Mutlu, S. Miller, K. Kurabayashi, and J. J. Allen, "Shaped comb fingers for tailored electromechanical restoring force," *Journal of Microelectromechanical Systems*, vol. 12, no. 3, pp. 373 – 383, June 2003.

[14] C. Chen and C. Lee, "Design and modeling for comb drive actuator with enlarged static displacement," *Sensors and Actuators A: Physical,* vol. 115, no. 2-3, pp. 530-539, Sept. 2004.

[15] J. D. Grade, H. Jerman, and T. W. Kenny, "Design of Large Deflection Electrostatic Actuators," *Journal of Microelectromechanical Systems,* vol. 12, no. 3, pp. 335-343, June 2003.

[16] D. O. Popa, J. T. Wen, H. E. Stephanou, G. Skidmore,and M. Ellis, "Dynamic modeling and Input Shaping for MEMS," in *Technical Proceedings of the 2004 NSTI Nanotechnology Conference and Trade Show (NANOTECH 2004)*, 2004, vol. 2, pp. 315-318.

[17] B. Borovic, C. Hong, X. M. Zhang, A. Q. Liu, and F. L. Lewis, "Open vs. Closed-Loop Control of the MEMS Electrostatic Comb Drive," in *Proc. of the 13th Mediterranean Conference on Control and Automation (MED'05),* 2005.

[18] M.S.-C. Lu and G. K. Fedder, "Position control of parallel-plate microactuators for probe-based data storage, "*Journal of Microelectromechanical Systems*, vol. 13, no. 5, pp. 759 – 769, Oct. 2004.

[19] B. Borovic, C. Hong, A. Q. Liu, L. Xie, F. L. Lewis, "Control of a MEMS Optical Switch," in *Proc. of 42nd IEEE Int'l conference od Decision and Control*, 2004, pp. 3039-3044.

[20] Sun, Y., Nelson, B. J., Potasek, D. P., Enikov, E., A bulk microfabricated multi-axis capacitive cellular force sensor using transverse comb drives, *Journal of Micromechanics and Microengineering*, vol. 12, no. 6, pp. 832-840, Nov. 2002.

[21] Y. Sun, D. Piyabongkarn, A. Sezen, B. J. Nelson, and R. Rajamani, "A high-aspect-ratio two-axis electrostatic microactuator with extended travel range," *Sensors and Actuators A*: *Physical*, vol. 102, no. 1-2, pp. 49-60, Dec. 2002.

[22] W. C. Tang, T. H. Nguyen, and R. T. Howe, "Laterally Driven Polysilicon Resonant Microstructures," *Sensors and Actuators A: Physical,* vol. 20, no. 1-2, pp 25-32, 1989.

[23] K. Isamoto, K. Kato, A. Morosawa, C. Chong; H. Fujita, H. Toshiyoshi, "A 5-V operated MEMS variable optical attenuator by SOI bulk micromachining," *IEEE Journal of Selected Topics in Quantum Electronics*, vol. 10, no 3, pp. 570 – 578, May-June 2004.

[24] E. Klaasen, *et al.*, "Silicon fusion bonding and deep reactive ion etching; a new technology for microstructures," *Sensors and Actuators A: Physical*, vol. 52, no. 1-3, pp.132-139, March-Apr.1996.

[25] H. Fujita, "Microactuators and micromachines," *Proc. Of the IEEE*, vol. 86, no 8, pp. 1721-1732, Aug. 1998.

[26] M. Elswenpoek, R. Wiegerink, *Mechanical Microsensors*. Berlin Heidelberg: Springer-Verlag, 2001.

[27] B. Borovic, A.Q. Liu, D. Popa, Z. Xuming, and F. L. Lewis, "Lateral Motion Control of Electrostatic Comb Drive:New Methods in Modeling and Sensing," in *Proc. of 16th IASTED Int'l Conf. on Modeling and Simulation,* 2005, pp 301-307.

[28] F. L. Lewis, D. M. Dawson, J. Lin, and K. Liu, "Tank Gun-Pointing Control with Barrel Flexibility Effects," in *ASME Publication Modeling and Control of Compliant and Rigid Motion Systems,* DSC-Vol. 31, 1991, pp. 47-54.

[29] J. Bryzek, A. Flannery, and D. Skurnik, "Integrating microelectromechanical systems with integrated circuits," *Instrumentation & Measurement Magazine, IEEE,* vol. 7, no. 2, pp. 51-59, June 2004.

[30] J. I. Seeger and B. B. Boser, "Charge Control of Parallel-Plate, Electrostatic Actuators and the Tip-In Instability," *Journal of Microelectromechanical Systems*, vol. 12, no. 5, pp. 656-671, Oct. 2003.

[31] H. Fujita and H. Toshiyoshi, "Optical MEMS," *IEICE Trans. Electron.*, vol. E83-C, no. 9, pp 1427-1434, Sep. 2000.

[32] X. M. Zhang, *et. al*, "Optical Power Regulator Using Closed Controlled MEMS Variable Optical Attenuator (VOA)," in *Proc. of 12th International Conference on Solid State Sensors, Actuators and Microsystems, Transducers 03*, 2003, pp. 595-598.

[33] C.-J. Kim, A.P. Pisano, R.S. Muller, and M.G. Lim, "Polysilicon microgripper," in *Digest of Technical Papers, 4th IEEE Solid-State Sensor and Actuator Workshop*, 1990, pp. 48 – 51.

[34] T. Hirano, T. Furuhata, K. J. Gabriel, and H. Fujita, "Design, fabrication, and operation of submicron gap comb-drive microactuators," *Journal of Microelectromechanical Systems* , vol. 1, no. 1, pp. 52 – 59, March 1992.

[35] L. Paratte, G.-A. Racine, N. F. de Rooij, and E. Bornand, "A novel comb-drive electrostatic stepper motor," in *Digest of Technical Papers, Solid-State Sensors and Actuators, Int'l Conf. on TRANSDUCERS*, 1991, pp. 886 – 889.

[36] C. H. Hsu and R. S. Muller, "Micromechanical electrostatic voltmeter," in *Digest of Technical Papers, Solid-State Sensors and Actuators, Int'l Conf. on TRANSDUCERS*, 1991, pp. 659 – 662.

[37] X. Huikai, L. Erdmann, X. Zhu; K. J. Gabriel, and G. K. Fedder, "Post-CMOS processing for high-aspect-ratio integrated silicon microstructures," *Journal of Microelectromechanical Systems*, vol. 11, no. 2, pp. 93 – 101, Apr. 2002.

[38] L. Li and D. Uttamchandani,"Modified asymmetric micro-electrothermal actuator: analysis and experimentation," *Journal of Micromechanics and Microengineering*, vol. 14, no. 12, pp. 1734-1741, Dec. 2004.

[39] C. R. Giles *et al.*, "A silicon MEMS optical switch attenuator and its use in lightwave subsystems," *IEEE Journal of Selected Topics in Quantum Electronics*, vol. 5, no. 1, pp. 18 – 25, Jan.-Feb. 1999.

[40] R. Legtenberg, A. W. Groeneveld, and M. Elwenspoek,"Comb-drive actuators for large displacements," *Journal of Micromechanics and Microengineering,* vol. 6**,** no. 3, pp. 320–329, Sept.1996.

[41] D. Elata, O. Bochobza-Degani, and Y. Nemirovsky, "Analytical approach and numerical alpha-lines method for pull-in hyper-surface extraction of electrostatic actuators with multiple uncoupled voltage sources," *Journal of Microelectromechanical Systems,* vol. 12, no. 5, pp. 681–691, Oct. 2003.

[42] Grade J D 1999 Large deflection, high speed, electrostatic actuators for optical switching applications, *Mechanical Engineering,* Stanford University, p 232

[43] B. Borovic, A. Q. Liu, D. Popa, H. Cai, and F. L. Lewis, "Open-loop vs. closed-loop control of MEMS devices: choices and issues," *Journal of Micromechanics and Microengineering*, vol. 15, no. 10, pp. 1917-1924, Oct. 2005.

[44] K. J. Astrom and B. Wittenmark, *Computer-Controlled Systems: Theory and Design,* 2nd ed. Upper Saddle River: Prentice-Hall, 1997.

[45] S. Franco, *Design with operational amplifiers and analog integrated circuits*, 3rd ed. Singapore: McGraw-Hill, 2002.

[46] W. J. Wang and R. M. Lin, "Simulation and Realization of Free Space Optical Switch Architecture Based on MEMS Vertical Mirrors," in *Tech. Proceedings of International. Conference on Modeling and Simulation of Microsystems*, 2002, vol. 1, pp 226-229.

[47] H. Toshiyoshi and H. Fujita, "Electrostatic Micro Torsion Mirrors for an Optical Switch Matrix," *Journal of Microelectromechanical Systems,* vol. 5, no. 4, pp. 231-237, Dec. 1996.

[48] T.P. Kurzweg and A.S. Morris III, "Macro-Modeling of Systems Including Free-Space Optical MEMS," in *Tech. Proc. of International. Conference on Modeling and Simulation of Microsystems*, 2000, pp 146-149.

[49] Y. Chen, Y. Shroff, and W. G. Oldham, "Phase-Lead Compensator to Improve the Transient Performance of Comb Actuators," in *Tech. Proc. of International. Conference on Modeling and Simulation of Microsystems*, 2000, pp 178-180.

[50] F.L. Lewis, *Applied Optimal Control and Estimation*. New Jersey: Prentice-Hall, 1996.

[51] Haim Baruh, *Analytical Dynamics*. Singapore: McGraw-Hill, 1999.

[52] Z. Izham and M. C. L. Ward, "Dynamic Simulation of a Resonant MEMS magnetometer in Simulink," *Sensors and Actuators A: Physical,* vol. 115, no. 2-3, pp. 392-400, Sept. 2004.

[53] J. Pons-Nin, A. Rodriguez, L. M. Castaner, "Voltage and Pull-In Time in Current Drive of Electrostatic Actuators," *Journal of Microelectromechanical Systems,* vol. 11**,** no. 3, pp. 196–205, June 2002.

[54] http://www.dspace.de/ww/en/pub/start.cfm

[55] D. Yan, A. Khajepour, and R. Mansour, "Modeling of Two-Hot-Arm Horizontal Thermal Actuator," *Journal of Micromechanics and Microengineering*, vol. 13, no. 2, pp. 312–322, March 2003.

[56] Q.-A. Huang and N. K. S. Lee, "Analysis and Design of Polysilicon Thermal Flexure Actuator," *Journal of Micromechanics and Microengineering*, vol. 9, no. 1, pp. 64–70, March 1999.

[57] R. Hickey, D. Sameoto, T. Hubbard, and M. Kujath, "Time and Frequency Response of Two-Arm Micromachined Thermal Actuators," *Journal of Micromechanics and Microengineering*, vol. 13, no. 1, pp. 40–46, Jan. 2003.

[58] M. J. Sinclair and K. Wang, "Thermal Actuator Improvements: Tapering and Folding," in *Proc. of SPIE, Smart Sensors, Actuators and MEMS,* 2003, vol. 5116, pp 237-251.

[59] D. Sameoto, T. Hubbard, and M. Kujath, "Operation of Electrothermal and Electrostatic MUMPs Microactuators Underwater," *Journal of Micromechanics and Microengineering*, vol. 14, no. 10, pp. 1359–1366, Oct. 2004.

[60] M. Sulfridge, T. Saif, N. Miller, and M. Meinhart, "Nonlinear Dynamic Study of a Bistable MEMS: Model and Experiment," *Journal of Microelectromechanical Systems*, vol. 13, no. 5, pp. 725-731, Oct. 2004.

[61] L. Lin and M. Chiao, "Electrothermal Responses of Lineshape Microstructures," *Sensors and Actuators A: Physical*, vol. 55, no. 1, pp. 35-41, July 1996.

[62] T. Akiyama, D. Collard, and H. Fujita, "Scratch Drive Actuator with Mechanical Links for Self-Assembly of Three-Dimensional MEMS," *Journal of Microelectromechanical Systems,* vol. 6, no. 1, pp. 10-17, March 1997.

[63] P. M. Osterberg, S. D. Senturia, "M-TEST: A Test Chip for MEMS Material Property Measurement Using Electrostatically Actuated Test Structures," *Journal of Microelectromechanical Systems,* vol. 6, no. 2, pp. 107-118, June 1997.

[64] Elmer S. Hung and Stephen D. Senturia, "Extending the Travel Range of Analog-Tuned Electrostatic Actuators," *Journal of Microelectromechanical Systems,* vol. 8, no. 4, pp. 497-505, Dec. 1999.

[65] R. Legtenberg, J. Gilbert, S. D. Senturia, and M. Elwenspoek, "Electrostatic Curved Electrode Actuators," *Journal of Microelectromechanical Systems,* vol. 6, No. 3, pp. 257-265, Sept. 1997.

[66] I.-H. Hwang, Y.-S. Shim, J.-H. Lee, “Modeling and Experimental Characterization of the Chevron-Type Bi-Stable Microactuator,” *Journal of Micromechanics and Microengineering*, vol. 13, no. 6, pp. 948–954, Nov. 2003.

[67] R. DeAnna, S. Roy, C. A. Zorman, and M. Mehregany, “Modeling MEMS Resonant Devices Over a Broad temperature Range,” *Ansys Solutions,* vol. 1, no. 2, pp. 22-24, 1999.

[68] Kurt E. Petersen, “Silicon as a Mechanical Material,” *Proceedings of the IEEE,* vol. 70, no. 5, pp. 420-457, May 1982.

[69] W. H. Lee, B. H. Kang, Y. S. Oh, and H. Stephanou, “Micropeg Manipulation with a Compliant Microgripper,” in *Proc. ICRA 03, IEEE International Conference on Robotics & Automation 2003,* 2003, vol. 3, pp. 3213-3218.

[70] R. Saini, A. Geisberger, K. Tsui, C. Nistorica, M. Ellis, G. Skidmore, “Assembled MEMS VOA,” in *International Conference on Optical MEMS, 2003 IEEE/LEOS,* 2003, pp. 139-140.

[71] M.-A. Gretillat, *et. al,* “Nonlinear Electromechanical Behaviour of an Electrostatic Microrelay,” in *International Conference on Solid State Sensors and Actuators, Transducers ’97,* 1997, vol. 2, pp. 1141-1144.

[72] V. L. Rabinovich, R. K. Gupta, and S. D. Senturia, “The effect of release-etch holes on the electromechanical behaviour of MEMS structures,” in *International Conference on Solid State Sensors and Actuators, Transducers ’97,* 1997, vol. 2, pp. 1125-1128.

[73] R. K. Gupta and S. D. Senturia, “Pull-in time dynamics as a measure of absolute pressure, Micro Electro Mechanical Systems,” in *Proceedings of Tenth IEEE Annual International Workshop on MEMS*, 1997, pp. 290-294.

[74] B. E. A. Saleh, M. C. Teich, *Fundamentals of Photonics*. New York: John Wiley & Sons, 1991.

[75] S. O. Kasap, *Optoelectronics and Photonics*. Upper Saddle River: Prentice-Hall, 2001.

[76] M. Madou, *Fundamentals of Microfabrication*. Boca Raton: CRC Press, 1997.

[77] G. T. A. Kovacs, *Micromachined Transducers Sourcebook*. New York: McGraw-Hill, 1998.

[78] W. C. Young and R. G. Budynas, *Roark's Formulas for Stress and Strain*, 7th ed. Singapore: McGraw-Hill, 2002.

[79] S. P. Timoshenko and J. N. Goodier, *Theory of Elasticity*, 3rd ed. Singapore: McGraw-Hill, 1970.

[80] S. S. Rao, *Mechanical Vibrations*, SI ed. Singapore: Prentice Hall, 2005.

[81] B. Friedland, *Control System Design: An Introduction to State Space Methods*. Singapore: McGraw-Hill, 1986.

[82] I. P. F. Harouche and C. Shafai, "Simulation of shaped comb drive as a stepped actuator for microtweezers application," *Sensors and Actuators A: Physical,* vol. 123-124, pp. 540-546 Sept 2005.

[83] J. Singh, T. Gan, A. A. Mohanraj, and S Liw, "3D free space thermally actuated micromirror device," *Sensors and Actuators A: Physical,* vol. 123-124, pp. 468-475, Sept 2005.

[84] J. D. Grade, K. Y. Yasumura, and H. Jerman, "Micromachined actuators with braking mechanisms" *Sensors and Actuators A: Physical,* vol. 122, no. 1, pp. 1-8, July 2005.

[85] L. Dong, L. Che, L. Sun, and Y. Wang, "Effects of non-parallel combs on reliable operation conditions of capacitive inertial sensor for step and shock signals," *Sensors and Actuators A: Physical,* vol. 121, no. 2, pp. 395-404, June 2005.

[86] Jian Ping Zhao, Hua Ling Chen, Jian Ming Huang and Ai Qun Liu, "A study of dynamic characteristics and simulation of MEMS torsional micromirrors," *Sensors and Actuators A: Physical,* vol. 120, no. 1, pp. 199-210, Apr. 2005.

[87] R. R. A. Syms, H. Zou, J. Stagg, and H Veladi, "Sliding-blade MEMS iris and variable optical attenuator," *Journal of Micromechanics and Microengineering*, vol. 14**,** no. 12**,** pp. 1700-1710, Dec. 2004.

BIOGRAPHICAL INFORMATION

Bruno Borovic was born in Zagreb, Croatia in 1971. He obtained Bachelor's degree in Electrical Engineering in 1996 and the Master's of Electrical Engineering degree in 1998 at Faculty of Electrical Engineering and Computing, University of Zagreb, Zagreb, Croatia. He spent four and a half years with the Brodarski institute, Zagreb, where he was involved in design and implementation of marine vessels and hydropower plant control and guidance systems. He was a Ph.D student at Automation & Robotics Research Institute of University of Texas at Arlington since 2001 till 2005. He published 3 journal papers, 20 conference papers and a book chapter. His current interests include control systems development and implementation, MEMS design, modeling and fabrication as well as control applications in MEMS area.